Turbulence Model Development Using Approximate Bayesian Computation

by

Olga A. Doronina

M.S., Moscow Institute of Physics and Technology, 2014

B.S., Moscow Institute of Physics and Technology, 2012

A thesis submitted to the

Faculty of the Graduate School of the

University of Colorado in partial fulfillment

of the requirements for the degree of

Doctor of Philosophy

Department of Mechanical Engineering

2020

Committee Members:

Peter E. Hamlington

Daven K. Henze

Debanjan Mukherjee

Ian Grooms

William Kleiber

Doronina, Olga A. (Ph.D., Mechanical Engineering)

Turbulence Model Development Using Approximate Bayesian Computation

Thesis directed by Prof. Peter E. Hamlington

Turbulent flows are present in a wide variety of real-world engineering problems, often by design due to their favorable mixing characteristics. At the same time, however, these flows are challenging to simulate due to the computational cost of resolving the wide ranges of spatial and temporal scales associated with practical engineering applications. There are two main approaches — large-eddy simulations (LES) and Reynolds averaged Navier Stokes (RANS) simulations — to reduce the computational cost of such simulations, and both approaches use models to represent unresolved small-scale processes and close the governing equations. To date, however, there is still no universally accurate closure model for either LES or RANS, and the most widely used models continue to employ empirical coefficients that have been calibrated for different flows and geometries.

To achieve more flexible turbulence model calibration using a range of reference data sources, in this dissertation we develop and demonstrate a method based on approximate Bayesian Computation (ABC). This approach provides probability distributions of calibrated parameters, and thus naturally provides uncertainties in parameter estimates. Moreover, compared to full Bayesian analyses, the ABC approach does not require the direct computation of a likelihood function, thereby enabling substantially faster estimation of unknown parameters and the calibration of more complicated models.

In this dissertation, we describe the ABC approach in detail, including the use of a Markov chain Monte Carlo (MCMC) technique, calibration step, adaptive proposal, and a linear regression correction. We demonstrate the baseline ABC method without MCMC by estimating unknown boundary conditions in simulations of turbulent buoyant jets, where lower-dimensional experimental measurements from laser absorption spectroscopy are used as reference data. Then, to demonstrate

how the ABC approach can be applied to turbulence model calibration, we estimate parameters for three different turbulence models.

First, ABC and MCMC methods are used to estimate values of model coefficients, as well as their joint probability distributions, in a subgrid-scale nonlinear model for LES of turbulent flows. The results from both *a priori* and *a posteriori* tests are provided for homogeneous isotropic turbulence. We also demonstrate how parameters can be calibrated without external reference data using ABC in an autonomic closure procedure.

Second, we use ABC and MCMC to estimate parameters in a nonequilibrium anisotropy closure for RANS simulations of unsteadily strained homogeneous flows. Unknown model parameters are estimated based on turbulence kinetic energy reference data for four impulsively-sheared homogeneous turbulence test cases, as well as for periodically-sheared homogeneous turbulence with five different shearing frequencies. The ABC and MCMC methods are shown to yield parameter values for the nonequilibrium anisotropy closure that provide good agreement between model results and reference data.

Finally, we demonstrate the ABC and MCMC approaches applied to a more complicated inhomogeneous flow, in particular the axisymmetric transonic bump case, and calibrate parameters in the RANS Menter Shear-Stress Transport model, using experiments as reference data.

In this dissertation, we thus demonstrate how the ABC approach can be applied to successfully calibrate a range of turbulence models, even those containing many parameters and partial differential equations.

Contents

Chapter

Tables

Table

Figures

Figure

Chapter 1

Introduction

Many engineering problems spanning a wide range of application areas involve turbulent fluid flow. Numerical simulations of such problems can significantly reduce the cost of engineering design and can help to better understand the physics of the problem. However, turbulent flows are challenging to simulate because of the high computational cost of resolving the full range of relevant spatial and temporal scales present in high Reynolds number real-world flows.

There are two common approaches to reduce the cost of such simulations: (*i*) large-eddy simulations (LES), which directly resolve turbulence on large scales and use subgrid-scale (SGS) models to represent small-scale physics, and (*ii*) Reynolds averaged Navier-Stokes (RANS) approaches, which resolve only averaged quantities and model turbulent fluctuations. In both of these approaches, however, there is no universally accurate turbulence model. All models rely on empirical coefficients that must be calibrated for different flows and geometries. In this dissertation, we find these coefficients using data-driven approaches based on experiments or high-fidelity computational data.

Traditionally, turbulence model parameters have been determined through either direct inversion of model equations, given some reference data, or using optimization techniques. Recently, a direct inversion technique for RANS has been developed by Parish and Duraisamy [84] using a machine learning approach. However, this approach becomes complicated for models with many different parameters or when the model itself consists of partial differential equations. Oberkampf, Trucano, and co-authors [80, 81, 82, 79] have advocated against optimization approaches in partic-

ular, noting that model parameter estimates must necessarily include quantification of uncertainty, especially given the uncertain nature of essentially all reference data (even if only due to statistical non-convergence), as well as the approximate nature of SGS models (even for the most sophisticated models).

Statistical methods, such as Bayesian approaches, provide an alternative path to model parameter calibration, giving a posterior probability distribution of unknown parameters. Cheung et al. [17] was the first to apply Bayesian inference method to calibrate Spallart-Allmaras turbulence model using velocity and skin friction experimental data. Oliver and Moser [83] extended this work by adding more models and stochastic extensions. Ray and co-authors [90, 60, 91, 93, 92] used a similar approach to calibrate RANS model parameters in more complex turbulent flow, namely jet-in-crossflow. Zhang and Fu [128] combined the high-dimensional model representation technique and the Gaussian process machine learning method to construct the surrogate model to make Bayesian inference more affordable. Safta et al. [98] used a Bayesian approach to estimate a joint distribution for LES sub-grid scale model parameters.

A benefit of the statistical Bayesian approach is that the posterior probability density also naturally provides uncertainties associated with each estimated parameter, in contrast to other inversion techniques that provide only a single point estimate for unknown parameters. However, solving the full Bayesian problem requires knowledge of the likelihood function, which can be difficult and/or costly to compute. In many cases, this likelihood function is approximated by a Gaussian or surrogate model used to substitute the expensive CFD simulations.

In this dissertation, we outline the use of approximate Bayesian computation (ABC) and Markov chain Monte Carlo (MCMC) methods to determine unknown model parameters and their uncertainties. The ABC method approximates the posterior distribution of parameters without using a likelihood function.

The ABC method was introduced and first widely applied in population genetics [6, 71, 122] and molecular genetics [70]. Then it was implemented in other scientific areas such as astrophysics [121, 14], chemistry [87], epidemiology [64, 130] and ecology [4]. More detailed recent

reviews of the ABC approach are provided by Csilléry et al. [26], Marin et al. [68], Lintusaari et al. [63], Sisson et al. [106] and, most recently, Beaumont [5]. The ABC method also has previously been used in engineering contexts for the estimation of boundary conditions in complex thermal-fluid flows [22, 21, 23], but here we will be the first to take advantage of both ABC and MCMC for discovering model parameter values and uncertainties in multi-parameter turbulence closures.

1.1 Overview of Dissertation

Details of the ABC approach, including the use of an MCMC technique, a calibration step, an adaptive proposal, and a linear regression correction are described in Chapter 2. In Chapter 3, a brief demonstration is provided of the baseline ABC rejection algorithm without MCMC for boundary condition estimation in simulations of turbulent buoyant jets using experimental reference data. This work was submitted to Experiments in Fluids titled "Flow Parameter Estimation Using Laser Absorption Spectroscopy and Approximate Bayesian Computation" by Jason D. Christopher, **Olga A. Doronina**, Daniel Petrykowski, Torrey R. S. Hayden, Caelan Lapointe, Nicholas T. Wimer, Ian Grooms, Gregory B. Rieker, and Peter E. Hamlington.

An example of LES nonlinear model calibration using the ABC-MCMC method is provided in Chapter 4. The parameters estimation for LES nonlinear model using higher fidelity direct numerical simulation (DNS) data is summarized in a paper submitted to *Physical Review Fluids* titled "Parameter Estimation for Subgrid-Scale Models Using Markov Chain Monte Carlo Approximate Bayesian Computation" by **Olga A. Doronina**, Colin A. Z. Towery, and Peter E. Hamlington. The results of using ABC in autonomic closure setup for LES nonlinear model were published in the AIAA Scitech conference paper titled "Autonomic closure for turbulent flows using Approximate Bayesian Computation" by **Olga A. Doronina**, Jason D. Christopher, Colin A. Z. Towery, Peter E. Hamlington, and Werner J. A. Dahm.

The parameter estimation study for nonequilibrium RANS model using homogeneous turbulent flow reference data is presented in Chapter 5. The preliminary results of this study was published in AIAA Scitech conference paper titled "Turbulence model development using Markov

chain Monte Carlo Approximate Bayesian Computation" by **Olga A. Doronina**, Colin A. Z. Towery, Jason D. Christopher, Ian Grooms, and Peter E.Hamlington.

The demonstration of ABC-MCMC applied to Menter Shear Stress Transport (SST) RANS model calibration for an axisymmetric transonic bump is presented in Chapter 6.

Finally, conclusions and possible future research directions are summarized in Chapter 7.

1.2 Primary Contributions of the Dissertation

This dissertation contains the following primary contributions:

(1) *Development of a flexible ABC-MCMC tool for turbulence model calibration.* This tool includes functionality for an initial calibration step, an adaptive proposal, and corrections using linear regression. An open-source package is provided on Github and the tool can be configured for either *a priori* or *a posteriori* model calibration; both approaches are demonstrated in this dissertation.

(2) *Demonstration of ABC without MCMC for boundary condition estimation.* Using the baseline ABC rejection algorithm, we estimate inflow boundary conditions for a high-temperature turbulent buoyant jet based on experimental measurements from laser absorption spectroscopy. This configuration, which has been studied previously by Christopher *et al.* [20], is used as an example to demonstrate the use of kernel density estimation with mirroring in the selection of parameters from joint posterior distributions, as well as perform an observing system experiment.

(3) *Demonstration of nonlinear SGS model calibration for LES using the ABC method.* We use ABC-MCMC method to estimate joint posterior distributions of two nonlinear SGS closure parameters using reference data from direct numerical simulations of homogeneous isotropic turbulence. We show that the resulting parameter values give excellent agreement with reference probability density functions of the SGS stress and kinetic energy production rate in *a priori* tests, while also providing stable solutions in forward LES (i.e., *a posteriori*

tests) for homogeneous isotropic turbulence. The ABC-MCMC method is thus shown to be an effective and efficient approach for estimating unknown parameters, including their uncertainties, in SGS closure models for LES of turbulent flows.

(4) *Demonstration of ABC-MCMC in autonomic closure.* We formulate and provide initial results for an autonomic closure approach using approximate Bayesian computation. Using test-scale filtering, the closure method is able to determine, on the fly, a non-parametric relation for the subgrid-scale stresses at the test scale. It then uses this relation at the LES grid-scale to achieve closure. Compared to prior implementations of autonomic closure, this approach has low memory requirements and instead relies on substantial processing power. Initial *a priori* and *a posteriori* tests on homogeneous isotropic turbulence indicate that the new approach can be used to accurately and stably close the LES equations.

(5) *Calibration of a nonequilibrium model in homogeneous turbulent flow using ABC-MCMC.* As reference data, we use turbulence kinetic energy data for four different impulsively strained cases and periodically sheared turbulence with five different shearing frequencies. The estimated parameters were found to be similar to, but not exactly the same as previously reported values, and gave good agreement between model results and the reference data.

(6) *Demonstration of ABC-MCMC on the RANS Menter SST model calibration.* The Menter SST model parameters are estimated using experimental data for the Bachalo-Johnson axisymmetric transonic bump. We provide simulation results for estimated parameters as well as a detailed description of the calibration step for ABC-MCMC and the choice of summary statistics.

1.3 Research Products in the Dissertation

A number of research products are associated with this dissertation, as outlined in the following.

Journal publications:

(1) Olga A. Doronina, Colin A. Z. Towery, and Peter E. Hamlington. Parameter Estimation for Subgrid-Scale Models Using Markov Chain Monte Carlo Approximate Bayesian Computation. Physical Review Fluids (submitted). 2020.

(2) Jason D. Christopher, Olga A. Doronina, Daniel Petrykowski, Torrey R. S. Hayden, Caelan Lapointe, Nicholas T. Wimer, Ian Grooms, Gregory B. Rieker, and Peter E. Hamlington. Flow Parameter Estimation Using Laser Absorption Spectroscopy and Approximate Bayesian Computation. Experiments in Fluids (submitted). 2020.

(3) Olga A. Doronina, Colin A. Z. Towery, Ian Grooms and Peter E. Hamlington. Approximate Bayesian Computation for Parameter Estimation in RANS Turbulence Models (in preparation, current draft is Chapter 5 of this dissertation).

(4) Olga A. Doronina, Scott M. Murman, and Peter E. Hamlington. Parameter Estimation for Menter SST RANS Model Using Approximate Bayesian Computation (in preparation, current draft is Chapter 6 of this dissertation).

Conference papers:

(1) Olga A. Doronina, Colin A. Z. Towery, Jason D. Christopher, Ian Grooms, and Peter E. Hamlington. Turbulence model development using Markov chain Monte Carlo Approximate Bayesian Computation. In **AIAA Scitech 2019 Forum**, page 1883, 2019

(2) Olga A. Doronina, Jason D. Christopher, Colin A. Z. Towery, Peter E. Hamlington, and Werner J. A. Dahm. Autonomic closure for turbulent flows using Approximate Bayesian Computation. In **2018 AIAA Aerospace Sciences Meeting**, page 0594, 2018

Conference presentations:

(1) Olga Doronina, Scott Murman, and Peter Hamlington. Parameter Estimation for Menter SST RANS Model Using Approximate Bayesian Computation. RMFM, 2020

(2) Olga Doronina, Scott Murman, and Peter Hamlington. Approximate Bayesian Computation for parameter estimation in RANS turbulence models. APS, 2019

(3) Olga Doronina and Peter Hamlington. Turbulence model development using Approximate-Bayesian Computation. RMFM, 2019

(4) Olga A. Doronina, Colin A. Z. Towery, Jason D. Christopher, Ian Grooms, and Peter E.Hamlington. Turbulence model development using Markov chain Monte Carlo Approximate Bayesian Computation. AIAA Scitech, 2019

(5) Olga Doronina, Colin Towery, and Peter Hamlington. Subgrid-scale model development using Approximate Bayesian Computation. APS, 2018

(6) Olga Doronina, Colin Towery, and Peter Hamlington. On Markov chain Monte Carlo Approximate Bayesian Computation approach for subgrid-scale model development. RMFM, 2018

(7) Olga A. Doronina, Jason D. Christopher, Colin A. Z. Towery, Peter E. Hamlington, and Werner J. A. Dahm. Autonomic closure for turbulent flows using Approximate Bayesian Computation. AIAA Scitech, 2018

(8) Olga Doronina, Jason Christopher, Colin Towery, Peter Hamlington, and Werner Dahm. Autonomic closure for turbulent flows using Approximate Bayesian Computation. APS, 2017

(9) Olga Doronina and Peter Hamlington. Parameter estimation for eddy-viscocity model using Approximate Bayesian Computation. RMFM, 2017

Chapter 2

Approximate Bayesian Computation Metholodogy

2.1 Introduction

While the numerical simulation of turbulent flows (e.g., for the prediction of turbulent velocity fields) is a forward problem, the estimation of turbulence model parameters given observed flow data (i.e., "truth" or "reference" data) is an inverse problem. Thus, in order to calibrate the parameters in a turbulence model, we need to solve an inverse problem.

One way to estimate unknown parameters is to use a statistical approach, such as a Bayesian method. Bayesian methods define the "solution" of the inverse problem as the probability distribution of unknown parameters given the truth data. This probability distribution is usually referred to as the posterior distribution, and the truth data is also referred to as observed data, which can come from experiments or higher fidelity models.

Bayes' theorem provides us with a posterior distribution by using a presumed prior distribution and likelihood function. The prior distribution is formed using our knowledge of unknown parameters. The likelihood function is the conditional density of the data given the parameters. Thus, the practical application of Bayes' theorem requires knowledge of the likelihood function, which can be difficult and/or costly to compute. In many cases, this likelihood function is approximated by a Gaussian distribution, which does not always reflect the actual likelihood function.

To avoid the costly calculation of the likelihood function, we can use likelihood-free methods such as approximate Bayesian computation (ABC). ABC provides us with an approximation of a posterior distribution but does not require the likelihood function to be known or estimated.

In the present chapter, we outline the ABC method in detail and explain the underlying assumptions. We also describe the ABC method with the Markov chain Monte Carlo (MCMC) technique and a calibration step, named ABC-MCMC, which significantly reduces the number of computations in the ABC algorithm. An adaptive proposal is introduced into the chain sampling in the ABC-MCMC procedure to account for model parameter correlations and to further accelerate the algorithm. Finally, we explain the local-linear regression technique, which acts as a post-processing correction that reduces the bias in the posterior distribution of parameters.

All of these algorithms and techniques are used in the remaining chapters of this dissertation, where we demonstrate the application of ABC-MCMC to turbulence model calibration.

2.2 Explanation of the ABC Approach

Statistical inference is a powerful instrument for solving inverse problems. Bayes' theorem, in particular, allows one to write posterior probability densities of model parameters $\mathbf{c} \in \mathbf{C}$ given data $\mathcal{D}$ as

$$P(\mathbf{c}|\mathcal{D}) = \frac{L(\mathcal{D} \,|\, \mathbf{c})\pi(\mathbf{c})}{\int_{\mathbf{C}} L(\mathcal{D} \,|\, \mathbf{c})\pi(\mathbf{c}) d\mathbf{c}}\,, \tag{2.1}$$

where $L(\mathcal{D} \,|\, \mathbf{c})$ is the likelihood function and $\pi(\mathbf{c})$ is the prior distribution of model parameters. A benefit of the statistical Bayesian approach is that the posterior probability density also naturally provides uncertainties associated with each estimated parameter in contrast to other inversion techniques that provide only a single point estimate for unknown parameters.

However, explicit analytical expressions for the likelihood function $L(\mathcal{D} \,|\, \mathbf{c})$ are rarely available. When the model parameter space $\mathbf{C}$ is finite and of low dimension, one can get the posterior density without an explicit likelihood function and without approximation using rejection sampling algorithm (Algorithm 1), which was introduced by Rubin [97]. This algorithm samples model parameters from prior distributions and compares model outcomes (or data) $\mathcal{D}'$ with observed reference data $\mathcal{D}$, which may come from experiments or a higher fidelity model. The algorithm accepts parameters only if the modeled and reference data are exactly the same.

Algorithm 1 Rejection sampling algorithm [97]

1: **for** $i = 1$ to N **do**
2: **repeat**
3: Sample $\mathbf{c}_i$ from prior distribution $\pi(\mathbf{c})$
4: Calculate $\mathcal{D}' = \mathcal{F}(\mathbf{c}_i)$
5: **until** $\mathcal{D}' = \mathcal{D}$
6: accept $\mathbf{c}_i$
7: Using all accepted $\mathbf{c}_i$ calculate joint pdf

In our case, however, the parameter space $\mathbf{C}$ is continuous and the model is imperfect, making Algorithm 1 impossible to use in the form outlined above. As an alternative, the acceptance criterion in Algorithm 1 can be relaxed to

$$d(\mathcal{D}', \mathcal{D}) \leq \varepsilon \,, \tag{2.2}$$

where $d(\cdot)$ is a distance function measuring the discrepancy between modeled data $\mathcal{D}'$ and given data $\mathcal{D}$. Sampled parameter values are accepted if the distance d is within some specified tolerance ε. The distance function may be a Kullback-Leibler divergence, Hellinger distance, or simply a mean-square error. The main idea of ABC is that if the distance between modeled and given statistics, $d(\mathcal{D}', \mathcal{D})$, is small enough, then the parameter $\mathbf{c}'$ is sampled from the posterior.

In order to reduce the dimensionality of the data and, hence, the computational expense, instead of the full observed data $\mathcal{D}$, one can use summary statistics $\mathcal{S}(\mathcal{D})$, such as the mean, standard deviation, or probability density function (pdf) of the data $\mathcal{D}$. The choice of summary statistics depends heavily on the problem and requires domain knowledge. Because of it, there is also a bit of an art to designing a summary statistic. The main assumption of ABC is that the summary statistic is sufficient enough, such that $P(\mathbf{c}|\mathcal{S}) = P(\mathbf{c}|\mathcal{D})$.

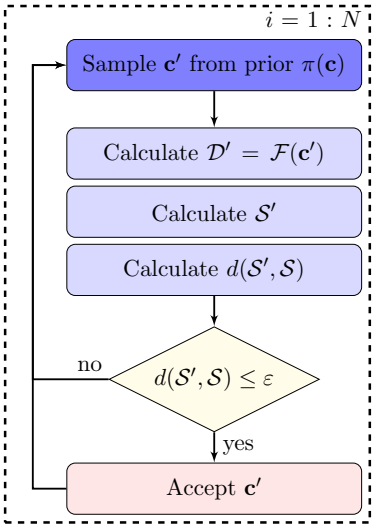

Figure 2.1: ABC rejection algorithm.

A model summary statistic can then be compared with the reference summary statistic using a statistical

distance function. By applying the statistical distance function, $d(\mathcal{S}', \mathcal{S})$, introducing the acceptance threshold ε, and using a summary statistic instead of the full data, we obtain the ABC rejection sampling algorithm (Algorithm 2 and Figure 2.1 for schematic).

Algorithm 2 ABC rejection sampling algorithm

1: Calculate true summary statistic $\mathcal{S}$
2: Sample N parameters $\mathbf{c}_i$ from prior distribution $\pi(\mathbf{c})$
3: **for** each $\mathbf{c}_i$ **do**
4: Calculate $\mathcal{D}' = \mathcal{F}(\mathbf{c}_i)$
5: Compute summary statistic $\mathcal{S}'$
6: Calculate statistical distance $d(\mathcal{S}', \mathcal{S})$
7: **if** $d(\mathcal{S}', \mathcal{S}) \leq \varepsilon$ **then**
8: accept $\mathbf{c}_i$
9: Using all accepted $\mathbf{c}_i$ calculate joint pdf

It should be noted that while ABC is based on Bayes' theorem, instead of determining the true posterior, it provides an approximation to the posterior distribution using a distance function and summary statistics [114], namely

$$P_\varepsilon(\mathbf{c} \,|\, \mathcal{S}) = P\left(\mathbf{c} \,|\, d(\mathcal{S}', \mathcal{S}) \leq \varepsilon\right) . \tag{2.3}$$

Under the assumption of sufficient summary statistics and if $\varepsilon \to 0$, then $P_\varepsilon(\mathbf{c} \,|\, \mathcal{S}) \to P(\mathbf{c} \,|\, \mathcal{D})$. However, in real life, too small of an ε is computationally impractical because it leads to too many rejections. Relaxing the acceptance criterion and not using sufficient summary statistics results in some bias in the final posterior distribution. Correction techniques such as local linear [6] and nonlinear [8] regressions aim to correct the bias caused by a nonzero ε.

The primary advantages of the ABC approach are the low cost relative to full Bayesian methods and the flexibility in parameter estimation for complex models. ABC does not require a likelihood and allows one to work with simulator-based models which can contain unobservable random quantities. A single set of parameters can be selected as a maximum *a posteriori* probability (MAP) estimate, a mean value, or another characteristic statistic of the posterior distribution.

2.3 Markov Chain Monte Carlo without Likelihood

Although Algorithm 2 is straightforward to implement, it can be computationally expensive and inefficient. The number of accepted parameters, which, in fact, form the posterior distribution, are only a small fraction of the total number of sampled parameters, and the region (in parameter space) of accepted parameters rapidly shrinks as the number of parameters in the model increases. Thus, most of the sampled parameters and evaluations of summary statistics do not contribute to the posterior. However, this problem can be solved, and the sampling technique can be significantly improved, by using Markov chain Monte Carlo (MCMC) methods.

The MCMC without likelihood method (or ABC-MCMC) introduced by Marjoram et al. [71], is based on the Metropolis–Hastings algorithm, however, no likelihoods are used or estimated. For an accepted parameter $\mathbf{c}_i$, the Metropolis–Hastings algorithm samples the next candidate parameter using the proposal $q(\mathbf{c}_i \to \mathbf{c}')$. If $d(\mathcal{S}', \mathcal{S}) \leq \varepsilon$, then the proposed parameters are accepted with probability

$$h = \min\left[1, \frac{\pi(\mathbf{c}')q(\mathbf{c}_i \to \mathbf{c}')}{\pi(\mathbf{c_i})q(\mathbf{c}' \to \mathbf{c}_i)}\right]. \tag{2.4}$$

Using the detailed balance condition, Marjoram et al. [71] demonstrated that the chain has a stationary distribution $P_\varepsilon(\mathbf{c} \,|\, \mathcal{S})$. An outline of the ABC-MCMC method is provided in Algorithm 3 (Figure 2.2).

Algorithm 3 ABC-MCMC

Starting from accepted parameters $\mathbf{c}_0$.
$i := 0$
while $i < N$ **do**
    Sample $\mathbf{c}'$ from proposal $q(\mathbf{c}_i \to \mathbf{c}')$
    Calculate $\mathcal{D}' = \mathcal{F}(\mathbf{c}_i)$
    Compute statistic $\mathcal{S}'$
    Calculate statistical distance $d(\mathcal{S}', \mathcal{S})$
    if $d(\mathcal{S}', \mathcal{S}) \leq \epsilon$ **then**
        Accept $\mathbf{c}'$ with probability $h = \min\left[1, \frac{\pi(\mathbf{c}')q(\mathbf{c}_i \to \mathbf{c}')}{\pi(\mathbf{c_i})q(\mathbf{c}' \to \mathbf{c}_i)}\right]$
    if accepted **then**
        Set $\mathbf{c}_i = \mathbf{c}'$ and increment i
Using all accepted $\mathbf{c}_i$ calculate the joint pdf.

We choose the proposal distribution to be the Gaussian with the current parameter $\mathbf{c}_i$ as the mean value and covariance matrix C, i.e. $q(\mathbf{c}_i \to \mathbf{c}') = q(\mathbf{c}'|\mathbf{c}_i, C)$. For a Gaussian proposal, $q(\mathbf{c}_i \to \mathbf{c}') = q(\mathbf{c}' \to \mathbf{c}_i)$ and h depends only on the prior. If the prior is uniform, then $\pi(\mathbf{c}) = \pi(\mathbf{c}')$, and the Gaussian proposal leads to $h = 1$ for any $\mathbf{c}'$. As a result, the algorithm reduces to a rejection method with correlated outputs [71].

2.3.1 Adaptive Proposal

The choice of proposal distribution is crucial for the rate of convergence of the Metropolis algorithm. A variable proposal with adapting size and spatial orientation could provide faster convergence.

We follow the adaptive proposal procedure outlined by Haario et al. [43], where the covariance C_i in the Gaussian proposal $q(\mathbf{c}'|\mathbf{c}_i, C_i)$ is updated during the process using all previous steps of the chain as

$$C_i = \begin{cases} C_0, & \text{if } i < k \\ s_d \mathrm{cov}(\mathbf{c}_0, \ldots, \mathbf{c}_i), & \text{if } i \geq k \end{cases}, \tag{2.5}$$

where $k > 0$ is the length of initial period without adaptation and s_d is a constant depending on the parameter space dimensionality as $s_d = (2.4)^2/\delta$, where δ is the dimensionality and initial covariance C_0. This algorithm does not require substantial additional computational cost, since the covariance $\mathrm{cov}(\mathbf{c}_0, \ldots, \mathbf{c}_i) = \mathrm{cov}_i$ can be calculated using the recursive formula

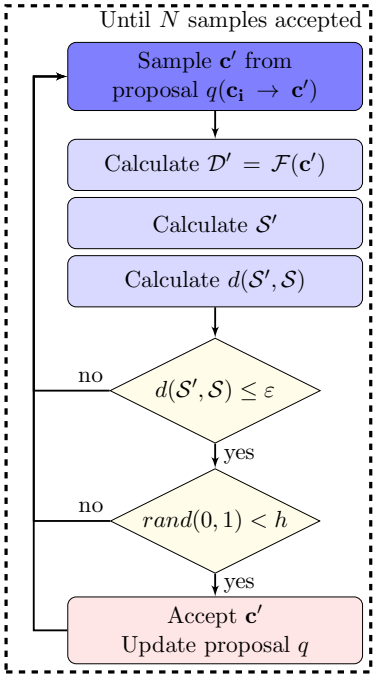

Figure 2.2: ABC-MCMC algorithm.

$$\mathrm{cov}_i = \frac{i-1}{i}\mathrm{cov}_{i-1} + \frac{1}{i+1}\left(\boldsymbol{\mu}_{i-1} - \mathbf{c}_i\right)\left(\boldsymbol{\mu}_{i-1} - \mathbf{c}_i\right)^T, \tag{2.6}$$

where $\boldsymbol{\mu}_i = [1/(i+1)] \sum_{k=0}^{i} \mathbf{c}_k$ is the average of all previous accepted parameter values, which also

satisfies the recursive formula

$$\boldsymbol{\mu}_i = \boldsymbol{\mu}_{i-1} - \frac{i}{i+1}\left(\boldsymbol{\mu}_{i-1} - \mathbf{c}_i\right) . \tag{2.7}$$

Since the adaptive Metropolis (AM) algorithm is adaptive, it is no longer Markovian, but Haario et al. [43] have shown that it has the correct ergodic properties and the accuracy of the AM algorithm is close to the accuracy of the standard Metropolis algorithm given a properly chosen proposal.

2.3.2 Calibration Step

The main advantage of the ABC-MCMC method is the high rate of acceptance, since we start from an accepted parameter and stay in the acceptance region. However, for high dimensional parameter spaces when the acceptance region is small, sampling the initial accepted parameters $\mathbf{c}_0$ can require many iterations.

The other problem of the ABC-MCMC algorithm is the same as for ABC rejection; namely, the fixed acceptance threshold value ε must be defined before the simulation, and indeed before the entire Markov chain is run. The choice of ε is important, since too large a tolerance interval results in a chain that is dominated by the prior. On the other hand, too small a value leads to a very small acceptance rate and also increase the initialization cost.

The proposal parameters such as the initial variance of the Gaussian must also be defined *a priori*. The percent of accepted parameters in ABC-MCMC depends on the variance in the proposal, such that a smaller variance leads to a larger number of accepted parameters, but more iterations are required to explore the posterior and to converge.

To solve these problems, Wegmann et al. [122] suggested to use a calibration step before the MCMC algorithm. In this step, a series of n_1 simulations are performed, where the parameters are sampled from their prior to obtain $P_{n_1}(d(\mathcal{S}', \mathcal{S}) \,|\, \mathbf{c}, \mathcal{S}')$, an approximation of the distance distribution $\pi(d(\mathcal{S}', \mathcal{S}) \,|\, \mathbf{c}, \mathcal{S}')$. This calibration step is used to adjust the range of the prior based on the range of $n_1 x_1$ parameters with smallest distances, where $0 < x_1 < 1$.

Then we perform another calibration sampling n_2 parameters from the prior within the new range and obtain a distance distribution $P_{n_2}(d(\mathcal{S}', \mathcal{S}) \,|\, \mathbf{c}, \mathcal{S}')$. Using the second calibration step, we can define a threshold distance, ε, such that $P(d(\mathcal{S}', \mathcal{S}) \leq \varepsilon) = x_2$, where x_2 is the desired ratio of the accepted simulations. We then randomly choose a sampled parameter for which $d(\mathcal{S}', \mathcal{S}) \leq \varepsilon$ as a starting point $\mathbf{c}_0$ for the Markov chain. These simulations are also used to adjust the proposal $q(\mathbf{c}_i \rightarrow \mathbf{c}')$ by setting initial covariance matrix C_0 to be diagonal matrix with $s_d$var on diagonal, where var is variance of sampled parameter for which $d(\mathcal{S}', \mathcal{S}) \leq \varepsilon$. In our case, the initial q is set to be a Gaussian distribution with standard deviation equal to the standard deviation of the retained parameters from the second calibration step. The resulting algorithm is based on ABC-MCMC with the calibration step from [122] and has an additional calibration step and an adaptive proposal. This algorithm is shown in Figure 2.3 as Algorithm 4.

2.4 Regression

As mentioned before, a nonzero acceptance threshold, ε, and insufficient summary statistics introduce some bias to the final posterior distribution. The bias related to ε is caused by the fact that all parameters with $d(\mathcal{S}, \mathcal{S}') \leq \varepsilon$ are accepted and treated equally, regardless of the actual value of $d(\mathcal{S}, \mathcal{S}')$. Beaumont et al. [6] suggested improvements to the ABC algorithm to eliminate this bias. The suggested correction techniques included smooth weighting based on $d(\mathcal{S}, \mathcal{S}')$ and local-linear regression adjustment. Both of these techniques can be applied in post-processing after running the actual ABC algorithm. However, it is possible that the linear regression models are not flexible enough to account for nonlinearity effects in the model parameters. A wider class of nonlinear regression models was introduced by Blum and François [8], where a feed-forward neural network was applied for the parameter estimations.

Regression adjustment became a state of the art technique for ABC and a description of its implementation can be found in [6, 7, 32, 68, 8]. In the following we outline the linear regression and local-linear regression techniques from [6]. Linear regression is provided just to introduce the idea of local-linear regression. An example of an application of local-linear regression to the turbulence

Algorithm 4 ABC-MCMC with calibration step

procedure CALIBRATION STEP(n, x)
  Sample n parameters $\mathbf{c}_i$ from prior distribution $\pi(\mathbf{c})$
  Calculate statistical distance $d(\mathcal{S}', \mathcal{S})$ for each of $\mathbf{c}_i$
  Define tolerance ε such that $P(d(\mathcal{S}', \mathcal{S}) \leq \varepsilon) = x$
  Randomly choose $\mathbf{c}_0$ from accepted points
  Define Gaussian proposal kernel variance as variance of parameters with $d(\mathcal{S}', \mathcal{S}) \leq \varepsilon$
procedure MCMC WITHOUT LIKELIHOOD($\mathbf{c_0}$, ε, var)
  while $i < k$ **do**
    Sample $\mathbf{c}'$ from proposal $q(\mathbf{c}_i, C_i)$
    Calculate $\mathcal{D}' = \mathcal{F}(\mathbf{c}', \theta)$
    Compute statistic $\mathcal{S}'$
    Calculate statistical distance $d(\mathcal{S}', \mathcal{S})$
    if $d(\mathcal{S}', \mathcal{S}) \leq \varepsilon$ **then**
      Accept $\mathbf{c}'$ with probability $h = \min\left[1, \frac{\pi(\mathbf{c}')q(\mathbf{c}_i \to \mathbf{c}')}{\pi(\mathbf{c}_i)q(\mathbf{c}' \to \mathbf{c}_i)}\right]$
    if accepted **then**
      Set $\mathbf{c}_i = \mathbf{c}'$, set $i = i + 1$
Using all accepted $\mathbf{c}_i$ calculate the joint pdf

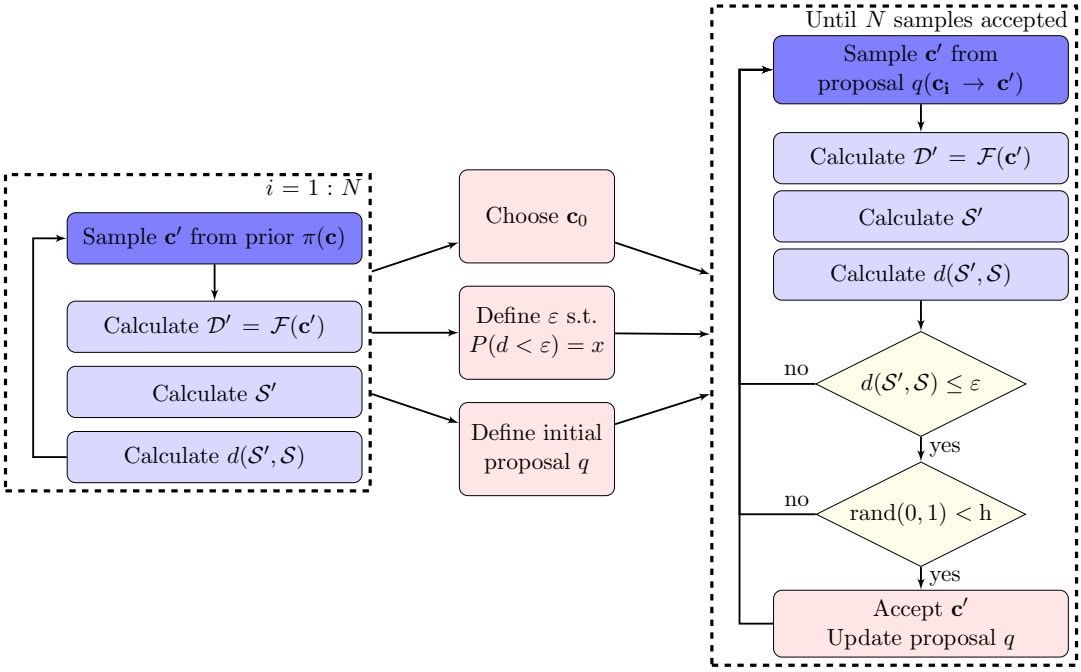

Figure 2.3: ABC-MCMC with calibration step.

model calibration can be found in Section 5.5.

2.4.1 Local-Linear Regression

The posterior distribution of model parameters is a conditional distribution $P(\mathbf{c}|\mathbb{S})$. Since the conditional distribution can be written in terms of a joint distribution and a marginal distribution, i.e $P(\mathbf{c}|\mathbb{S}) = P(\mathbb{S}, \mathbf{c})/P(\mathbb{S})$, we can find a posterior distribution by estimating the joint density, $P(\mathbb{S}, \mathbf{c})$, and dividing it by estimate of the marginal density, $P(\mathbb{S})$, evaluated at $\mathbb{S} = \mathcal{S}$, where $\mathcal{S} \equiv (s_1, \ldots, s_q)$ is the truth summary statistics vector.

As a result of the ABC algorithm (Algorithm 2) we obtain m pairs $(\mathbf{c}_i, \mathcal{S}'_i)$ of sampled parameter-vectors, $\mathbf{c}_i$, and the corresponding modeled summary statistics vectors, $\mathcal{S}'_i$.

Linear regression is a well known technique used to fit a linear model to provided data, i.e. find linear model coefficients, which minimize the error between the linear model and the data. We can assume that the conditional density of the model parameters, can be described by a linear model

$$\mathbf{c}_i = \alpha + (\mathcal{S}'_i - \mathcal{S})^T \beta + \zeta_i, \quad i = 1, \ldots, m, \tag{2.8}$$

where ζ_i is the error between the linear model and the data, which is assumed to have a normal distribution with zero mean and common variation (assumption of homoscedasticity), where α is an intercept and β a vector of regression coefficients. The parameters α and β can be found using least-square minimization, i.e. as parameters minimizing the sum

$$\sum_{i=1}^{m} \left[\mathbf{c}_i - \alpha + (\mathcal{S}'_i - \mathcal{S})^T \beta\right]^2 . \tag{2.9}$$

The solution for this minimization problem is

$$(\hat{\alpha}, \hat{\beta}) = (X^T X)^{-1} X^T \theta, \tag{2.10}$$

where

$$X = \begin{pmatrix} 1 & s'_{11} - s_1 & \cdots & s'_{1q} - s_q \\ \vdots & \vdots & \ddots & \vdots \\ 1 & s'_{m1} - s_1 & \cdots & s'_{mq} - s_q \end{pmatrix}, \quad \theta = \begin{pmatrix} \mathbf{c}_1 \\ \vdots \\ \mathbf{c}_m \end{pmatrix} . \tag{2.11}$$

Thus, we can shrink the parameters $\mathbf{c}_i$ in a linear manner as

$$\mathbf{c}_i^* = \mathbf{c}_i - (\mathcal{S}_i' - \mathcal{S})^T \hat{\beta}\,, \tag{2.12}$$

which are now from the corrected posterior distribution $P(\mathbf{c}|\mathcal{S})$.

Local-linear regression relaxes the linearity assumption, i.e. we assume linearity only locally around $\mathcal{S}$. To achieve this we estimate the parameters (α, β) by minimizing the weighted least-squares criterion instead of (2.9), i.e.

$$\sum_{i=1}^{m} \left\{\mathbf{c}_i - \alpha + (\mathcal{S}_i' - \mathcal{S})^T \beta\right\}^2 K_\delta(d(\mathcal{S}_i', \mathcal{S}))\,, \tag{2.13}$$

where K_δ is the kernel with bandwidth δ. Beaumont et al. [6] suggested to use the Epanechnikov kernel as K_δ, namely

$$K_\delta(t) = \begin{cases} c\delta^{-1}(1 - (t/\delta)^2), & t \leq \delta \\ 0, & t > \delta \end{cases}, \tag{2.14}$$

where c is a normalization constant and $\delta \leq \varepsilon$. Other kernel functions can be used instead, e.g. Gaussian kernel, if one wants smooth decrease to zero in parameter weights.

The solution for this minimization problem in Eq. (2.13) is

$$(\hat{\alpha}, \hat{\beta}) = (X^T W X)^{-1} X^T W \theta, \tag{2.15}$$

where W is the diagonal matrix with $K_\delta(d(\mathcal{S}_i', \mathcal{S}))$ on diagonal. Weighted by $K_\delta(d(\mathcal{S}_i', \mathcal{S}))$, the $\mathbf{c}_i^*$ from Eq. (2.12) provide an approximate sample from the posterior distribution.

Wegmann et al. [122] demonstrated that stationary distribution of the ABC-MCMC chain is identical to the ABC algorithm posterior distribution and suggested to apply local-linear regression, outlined above, to the posterior distribution obtained with ABC-MCMC algorithm. Wegmann et al. [122] applied local-linear regression on a subsample of size t consisting of the samples associated with the smallest distances $d(\mathcal{S}', \mathcal{S})$ generated by the Markov chain, thus, adding a postprocessing correction to the ABC-MCMC algorithm.

An example of the local-linear regression correction applied to turbulence parameter calibration is provided in Section 5.5.

Chapter 3

Flow Parameter Estimation Using Approximate Bayesian Computation

3.1 Introduction

Despite ongoing advances in the quality and breadth of experimental measurements, the complete characterization of many real-world engineering systems remains a considerable challenge. For example, experimental diagnostics can now provide spatially and temporally resolved measurements of temperature, velocity, chemical composition, and other properties, but few (if any) experiments can provide fully resolved three-dimensional (3D) spatial and temporal fields over the entire system domain simultaneously for all quantities of interest. Although numerical simulations can, in principle, be used to complement experimental measurements and develop a more comprehensive understanding of a system, physically accurate boundary conditions and fluid properties are required to ensure that the simulations are modeling a truly equivalent configuration. Once again, however, such information is often difficult to obtain experimentally.

Traditionally, the challenge of estimating unknown parameters in real-world engineering systems has been addressed by proposing *a priori* distributions of parameter values, generating model (e.g., simulation) data using parameters sampled from these distributions, and then calculating likely distributions of true parameters using statistical inversions based on available reference or experimental data [79, 80, 81, 82]. Various optimization methods have been used to perform these inversions (e.g., Refs. [66, 99, 119, 85, 54]), but such techniques typically provide single values of unknown parameters, with limited measures of uncertainty when using imperfect experimental data and computational models.

Bayesian methods naturally overcome this limitation by providing a probability distribution of unknown parameters. For example, several studies have successfully performed parameter estimation for engineering problems using full Bayesian methods [31, 78, 24, 116, 108]. However, such methods require knowledge of the likelihood function which often requires extensive observations or simplifying assumptions.

In this study, we demonstrate the use of approximate Bayesian computation (ABC) for estimating unknown parameters in the real-world turbulent thermal-fluid system, namely, the high-temperature turbulent flow produced by an industrial catalytic burner. The catalytic burner examined here has been studied previously [51, 50] and is a scaled-down version of catalytic burners commonly used for industrial heating of food products and polymer films. The catalytic burner combusts a mixture of methane and desiccated air and an iron-chromium alloy catalyst mesh is welded to an open-box metal frame. The catalyst is used to achieve more complete combustion at lower temperatures, thereby reducing the presence of reactive products of incomplete combustion and pollutants [25] in the burner exit gases. Experimental measurements were made using wavelength modulation spectroscopy (WMS) which is a specialized form of laser absorption spectroscopy (LAS) and provides line-of-sight, absorption-weighted average temperature and chemical species concentrations. More details about experiment setup and measuring techniques can be found in Appendix A.

Although the LAS technique [51, 50, 52] can provide accurate, time-resolved temperature measurements above the burner surface, limited information is available regarding the speed of gases exiting the burner. The available LAS measurements suggest that there is incomplete combustion within the catalytic burner, but specific details of the exit gas chemical composition are not available because the approach does not probe all of the exit gas species. At the same time, the knowledge of the speed of gases exiting the burner and the prevalence of reactive products of incomplete combustion in the exit gases are essential parameters to set up the numerical simulations in a configuration that is equivalent to the experiment.

Thus, in this chapter, we consider large eddy simulation to be a model in ABC algorithm

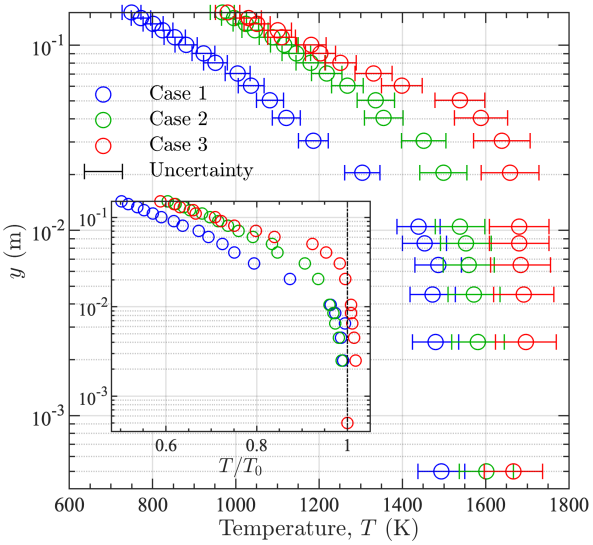

Figure 3.1: Vertical profiles of absorption-weighted time-averaged temperature above the catalytic burner. Results are shown for the three experimental cases in Table 3.1. Experimental uncertainties are based on instrument validation. The inset shows temperature profiles normalized by T_0 from Table 3.1.

and estimate the flow speed and the prevalence of additional heat release above the burner due to continued combustion. We demonstrate how the classical form of ABC algorithm, the acceptance-rejection ABC algorithm (Algorithm 2, Figure 2.1), can be used to estimate these parameters. As a reference data in ABC algorithm, we use available line-of-sight, absorption-weighted average temperatures from LAS. In following, we discuss details of ABC set up and demonstrate the resulting posterior distribution and estimated parameters. We also include an observing system experiment to confirm the validity of the estimated parameters.

3.2 Reference Data

The reference data we are using in this study is line-of-sight, absorption-weighted average temperatures measured using wavelength modulation spectroscopy (WMS). The WMS measurements were made along the longest dimension of the burner at the midpoint of the burner width. Vertical profiles of line-of-sight, absorption-weighted average temperature, used further as reference data, were measured for three different burner operating powers and can be seen in Figure 3.1.

Table 3.1: Catalytic burner operating conditions studied here, showing the burner power flux, equivalence ratio ϕ, line-of-sight absorption-weighted time-averaged surface temperature T_0, and estimated bulk flow speed V_0 of burner exit gases.

Case	Power (W/cm^2)	ϕ	T_0 (K)	V_0 (m/s)
1	16	0.80	1494	0.37
2	27	0.85	1602	0.65
3	27	1.00	1667	0.62

3.2.1 Burner Operating Conditions

In this experiment, mass flow controllers were used to separately regulate the flow rates of air and methane, allowing independent control of the burner power flux and equivalence ratio, ϕ. The catalytic burner was operated at two power fluxes, and three values of ϕ, as summarized in Table 3.1.

For the first case (denoted 'Case 1' herein), the power flux was 16 W/cm^2 with $\phi = 0.80$. These conditions were thought to result in complete combustion within the catalyst, such that all reactions were finished before hot products exited the burner. The temperature consistently decreased away from the burner surface for this case, indicating no significant heat addition. The line-of-sight, absorption-weighted time-averaged temperature of the burner surface was $T_0 = 1494$ K, measured 0.5 mm above the surface assuming a laser beam width of 1 mm. Based on bulk mass-flow measurements, the measured atmospheric pressure, and the assumed density and composition (i.e., complete combustion was assumed) of gases exiting the burner, the inlet speed was estimated as $V_0 = 0.37$ m/s for this case. Although V_0 is not measured directly in the experiments and will not be used as reference data in the ABC algorithm, this estimate allows us to determine whether the correct trends in V_0 are captured by ABC and whether the predicted values have reasonable magnitudes.

For 'Case 2', the inlet power was substantially increased as compared to Case 1, but with a similar equivalence ratio; this case had a power flux of 27 W/cm^2 and $\phi = 0.85$. The resulting

burner surface temperature was $T_0 = 1602$ K and the inlet speed was estimated as $V_0 = 0.65$ m/s. Given the higher power and ϕ of this case, it was thought possible that continued combustion could occur above the burner, although it will be seen in the following that the ABC parameter estimation method predicts that this is unlikely based on the LAS temperature measurements.

Finally, the burner was operated for conditions that suggested the presence of continued reactions above the burner. This case, referred to as 'Case 3', had an inlet power flux of 27 W/cm^2 and $\phi = 1.00$. This power flux was the same as for Case 2, but ϕ was significantly higher than either Cases 1 or 2. Compared to Case 2, this results in a higher surface temperature, $T_0 = 1667$ K, and a lower estimated inlet speed, $V_0 = 0.62$ m/s. The additional fuel entering the combustor in Case 3 causes additional chemiluminescence above the burner surface, indicative of continued combustion, as well as detectable concentrations of OH; it will be seen in Section 5.4 that the ABC method predicts additional heat release above the burner for this case.

3.2.2 Vertical Temperature Profiles

Vertical profiles of line of sight, absorption weighted time-averaged temperature for the three experimental burner operating conditions are shown in Fig. 3.1. The time averaging spans the entire 10 min time series obtained using LAS at each measurement height.

The temperature profiles in the main panel of Fig. 3.1 indicate that, from Case 1 to 3, the temperature near the burner surface increases from roughly 1500 K to nearly 1700 K. Moreover, the temperature remains high a greater distance above the burner for Case 3, and subsequently decreases rapidly to match the temperatures seen for Case 2 farther from the burner. It should be noted that we decreased the air flow rate in order to achieve a larger ϕ in Case 3, and thus the estimated inlet speed of Case 2 was actually slightly higher than for Case 3, as indicated in Table 3.1.

Differences in the profile shapes are more clearly indicated by the profiles of normalized temperature T/T_0 in the inset of Fig. 3.1, where the burner surface temperatures, T_0, are given in Table 3.1. In addition to further emphasizing the rapid decrease in temperature far from the burner

in Case 3, the inset also indicates that there is an increase in temperature immediately above the burner for this case. This is indicative of additional heat release due to continued combustion, which is assumed to arise from reactive products of incomplete combustion exiting the burner at these conditions.

The temperature profiles in Fig. 3.1 thus provide valuable information concerning the characteristics of the flow field above the burner for different operating conditions, but these results also lead to new questions about the magnitude and extent of additional heat release above the burner for Case 3. Moreover, it is not possible based on the results in Fig. 3.1 to rule out additional, although more moderate, heat release above the burner even for Cases 1 and 2.

In the following, we use ABC and LES to determine inflow speeds and whether additional heat release is indeed implied by the profiles in Fig. 3.1. We will show, in particular, that only Case 3 is likely to have additional heat release above the burner. Using LES, we then show that the resulting parameter estimates enable accurate predictions of the vertical temperature profile for each case, including the rapid decrease in temperature far from the burner for Case 3.

3.3 Present Configuration of ABC

Here we describe details of ABC setup such as choice of summary statistics, distance function and acceptance criteria.

Based on the LAS measurements, we seek estimates for three parameters of the catalytic burner system: the speed of gases exiting the burner, the intensity of heat addition above the burner due to continued combustion of reactive chemical species in the exit gases, and the spatial region over which heat addition occurs. The first of these properties is known only approximately based on the measured mass flow rates and the assumed density of gases exiting the burner, while the other two quantities are implied by the results shown in Fig. 3.1, particularly for Case 3. Each of these properties are required to obtain a more complete understanding of the catalytic burner, as well as to accurately model the burner using numerical simulations.

The LAS measurements described in Section 3.2 provide line-of-sight absorption-weighted

temperature time series data $\mathcal{D}$, which give the time-averaged vertical profiles of temperature shown in Fig. 3.1; these profiles are the reference summary statistic $\mathcal{S}$ in the present demonstration of ABC.

This choice of summary statistic is based on prior knowledge of the connection between burner inlet speeds and vertical profiles of temperature in turbulent buoyant jets. In particular, Christopher et al. [20] used reference data from numerical simulations to show that single-location temperature measurements at heights within approximately 0.5 to 1.5 burner widths can be used to infer inlet speeds. Here, we further improve our ability to predict the speed by using average temperatures at multiple locations simultaneously.

The model data, $\mathcal{D}'$, are obtained from 3D LES of the experimental configurations, allowing the calculation of equivalent vertical profiles of time-averaged absorption-weighted temperature, denoted $\mathcal{S}'$, at the same locations as in the experiments. Details of the numerical model are provided in Appendix A.2.1 and the procedure by which LAS-equivalent statistics are calculated from the model data is described in Section A.2.2.

The LES data were also adjusted to account for uncertainties inherent in the measurements. For each sampled parameter $\mathbf{c}$, a uniform random number between $\pm 3\%$ was selected independently 1,000 times, and this amount of uncertainty was added to the entire profile of temperature (assuming that any bias observed in the experiment was correlated at all heights). The resulting modeled summary statistics $\mathcal{S}'$, each with added uncertainty, were then compared with the reference values $\mathcal{S}$ for each of the 1,000 randomly selected uncertainties, for each value of $\mathbf{c}$. It should be noted, however, that the variation in $\mathcal{S}'$ was generally larger due to variations in $\mathbf{c}$, as opposed to variations in the applied uncertainty.

For the distance function, $d(\mathcal{S}, \mathcal{S}')$, we use the RMSE over all measurement locations. Other metrics are also possible, such as the L1 and L2 norms, or the integrated difference in temperature at all locations. However, we found that the posterior distributions were similar for each of these metrics, and so here we only show results using RMSE, which is a robust and common metric for computing statistical distances. Chai and Draxler [15] have also shown that RMSE is particularly

appropriate for comparing model and reference data when the model error is assumed to be Gaussian, as is likely the case here. Each measurement in the RMSE is given equal weighting despite the fact that the measurements near the burner surface are very close together; the resulting additional weight given to the near-surface region was intentional, since matching the lower portion of the profile is key to determining whether continued combustion is present above the burner.

The choice of rejection threshold ε can have a substantial impact on the approximate posterior distribution. Values of ε that are too large will result in the acceptance of too many sampled parameters, giving a biased posterior that is similar to the prior distribution; that is, no additional information is gained from the ABC method [20]. Conversely, an ε that is too small will result in the rejection of all but a single case, giving a posterior with very low statistical confidence. Although Marin *et al.* [67] and Lintusaari *et al.* [63] argue that a smaller ε is generally preferable, the specific value is often largely determined by the available computational resources. Based on the high computational cost of 3D LES, a relatively limited number [i.e., $\mathcal{O}(10^3)$] of simulations could be performed in the present study. Thus, using the same approach as in previous studies (e.g., Refs. [113, 69, 67, 63, 95]), here we calculate approximate posteriors corresponding to various values of ε to show convergence of the posterior as ε decreases. The value of ε is characterized here by the percentage of sampled parameters retained in the posterior, where smaller values of ε give lower acceptance rates.

Uniform distributions were used for the prior, $\pi(\mathbf{c})$, where $\mathbf{c}$ is the vector of unknown parameters corresponding to the burner inlet speed, the intensity (or 'strength') of heat addition, and the extent (or 'height') of heat addition above the burner. The prior must be sufficiently wide to encompass realistic values of $\mathbf{c}$, but narrow enough to keep the ABC procedure computationally affordable. Based on the experimental estimates of V_0 in Table 3.1, the range of inlet speeds in the prior was 0.13 m/s to 0.8 m/s for Case 1 and 0.13 m/s to 1.13 m/s for Cases 2 and 3.

Heat addition due to ongoing reactions was modeled in the LES using a half-Gaussian source term that peaks at the burner surface; this source term was parameterized by the total amount of heat added in Watts (W), and by the standard deviation (or height) of the half-Gaussian distri-

bution. The lower limit for heat addition was 0 W, indicating no additional combustion, and the upper limit was determined from an energy balance based on how much power is going into the system from the reactants and how much energy it would take to heat the gases to the measured inlet temperature, giving a maximum value of 2500 W across all cases. The height of heat addition is equivalent to three standard deviations of the half-Gaussian distribution, and corresponds to the height at which the majority of the heat has been added. A lower limit of 0.01 m was chosen to confine the heat addition very close to the burner and, based on previous experimental measurements showing increasing temperature above the catalytic burner, the upper limit was chosen as 0.07 m.

We used a fixed burner surface temperature close to T_0 from Table 3.1 for all simulations of a given case. This decision was made to reduce the computational cost, since each unknown parameter adds approximately an order of magnitude more simulations to the ABC method; the number of simulations, N, needed to identify n parameters goes as $N \sim 10^n$. More importantly, the temperature measurements at the lowest height are likely to accurately represent the exit temperature of the burner since the laser skims the burner surface at the lowest measurement height (i.e., at 0.5 mm).

During the ABC procedure, parameter values $\mathbf{c}$ were deterministically chosen to uniformly sample the entire prior $\pi(\mathbf{c})$, thereby reducing bias and effectively covering the entire parameter space. This approach was chosen over other viable options (e.g., random draws, Latin hypercube sampling, etc.) due to the cost of the 3D LES for each choice of $\mathbf{c}$. In total, $N \sim 10^2$ – 10^3 parameter values $\mathbf{c}$ were modeled using LES for each of the three experimental configurations.

3.4 Parameter Estimation Results

Here we calculate posterior distributions of inlet speed, heat source strength, and heat source height using ABC for each of the three burner cases. The posteriors are calculated for four different values of ε, corresponding to sampled parameter acceptance rates between 5% and 20%. A total of $N = 495$ sampled parameters were modeled using LES for Case 1, while $N = 693$ parameters were

modeled for each of Cases 2 and 3.

Using parameter estimates from the posterior distributions, we are able to recover trends in the experimentally estimated inflow speed V_0, as well as predict additional heat release above the burner for Case 3, indicating incomplete combustion within the catalyst at these conditions. We then show that LES of the catalytic burner using the estimated parameter values provides modeled vertical profiles of average temperature that agree closely with the LAS measurements for each case. Finally, we present results from an observing system experiment, further demonstrating the predictive power and effectiveness of the ABC method.

3.4.1 Posterior Distributions and Estimated Parameters

The primary outcome from ABC is the multi-dimensional posterior, $P[\mathbf{c}|d(\mathcal{S},\mathcal{S}') \leq \varepsilon]$, from which we can estimate unknown parameter values and determine the degree of confidence in these values. Here, $\mathbf{c}$ and the posterior represent three unknown parameters (i.e., inlet speed, heat source strength, and heat source height). As a result, we show one- and two-dimensional (1D and 2D, respectively) marginalized posteriors, computed using Gaussian kernel density estimation (KDE) [103]. We also employ mirroring when the posteriors peak at the bounds of the prior $P(\boldsymbol{\theta})$. The maximum *a posterior* probability (MAP) values from the full 3D posterior with KDE and mirroring provide estimates of the unknown parameters, as summarized in Table 3.2.

Table 3.2: Maximum *a posterior* probability estimates from ABC of the burner inlet speed, heat source strength, and heat source height for each of the cases. Parameter estimates are obtained from the 5% acceptance rate full 3D posteriors, and values in parentheses show the nearest simulation values.

		Heat source properties	
Case	Inlet speed (m/s)	Strength (W)	Height (m)
1	0.30 (0.30)	0 (0)	0.040 (0.040)
2	0.61 (0.63)	50 (0)	0.042 (0.040)
3	0.48 (0.47)	726 (750)	0.047 (0.048)

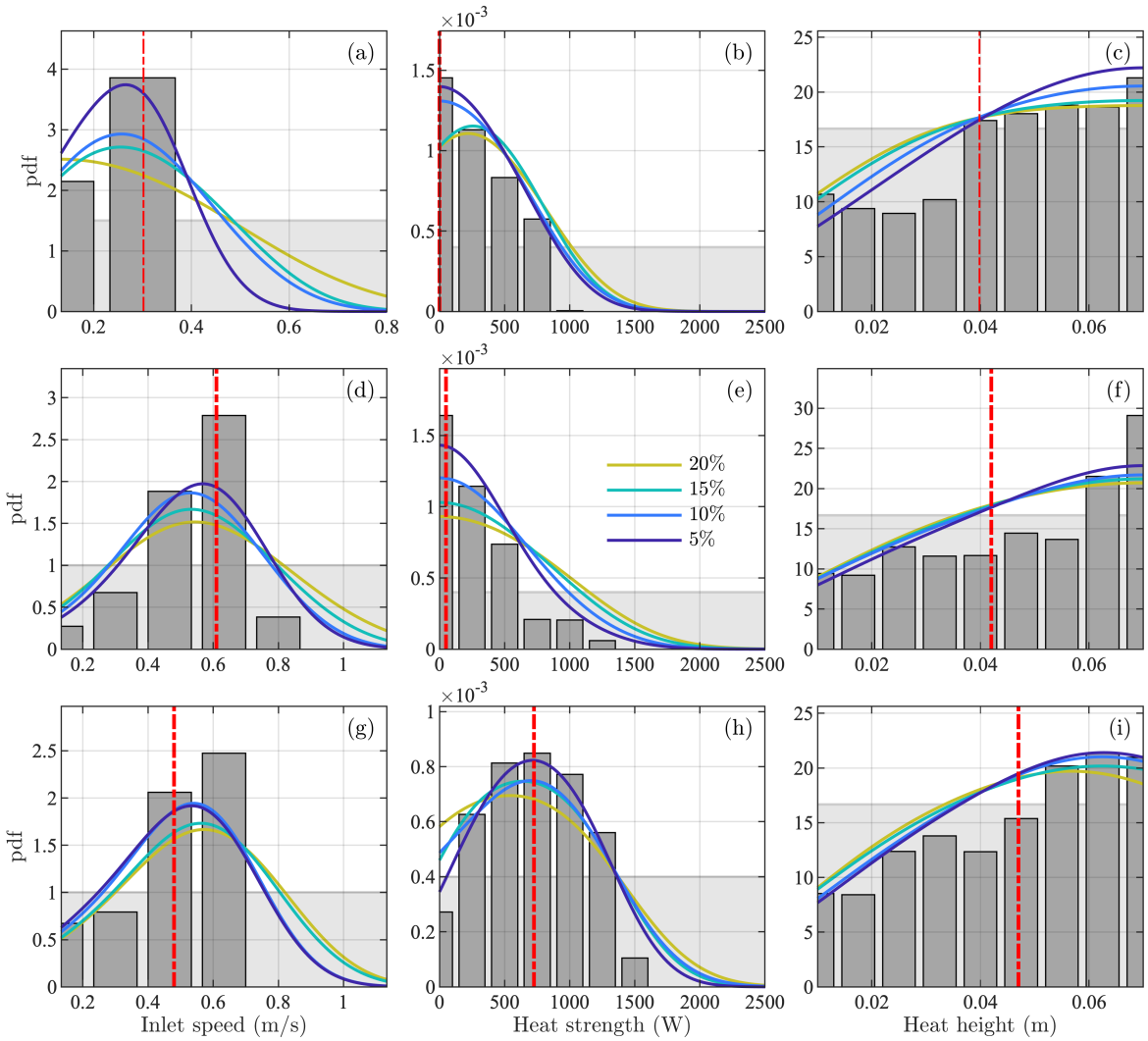

Figure 3.2: One-dimensional marginalized posteriors for Cases 1, 2 and 3 (top, middle, and bottom rows, respectively) for inlet speed, heat source strength, and heat source height (left, middle and right columns, respectively). Line colors correspond to the percentage of accepted simulations, as determined by the rejection threshold ε. Raw posteriors (i.e., before Gaussian kernel estimation) are shown by dark gray bars, and prior distributions are shown by the lighter gray regions. Vertical red dash-dot lines show the most probable parameter values from the full 3D posterior for a 5% acceptance rate, summarized in Table 3.2.

Figure 3.2 shows the 1D posteriors of the three unknown parameters for each of the three burner cases. For Case 1, the posterior of the inlet speed approaches the bulk flow experimental estimate of $V_0 = 0.37$ m/s as ε decreases, as shown in Fig. 3.2(a). Although the mode of the posterior for the smallest value of ε occurs at 0.3 m/s, which is lower than the experimental estimate, the

rough correspondence nevertheless provides confidence in the accuracy of the ABC method. The inverse relationship between the inlet speed and the heat source strength can be seen in the 2D marginalized posteriors in Fig. 3.3 for ε corresponding to a 5% acceptance rate. The dominant mode in the 2D posterior of heat source strength and inlet speed in Fig. 3.3(a) corresponds to 0 W and 0.3 m/s, respectively. However, there is also a non-zero probability of larger heat source strengths as the inlet speed decreases, indicating that additional heat release can compensate for lower inlet speeds. Nevertheless, the peak in the joint posterior at 0.3 m/s, with 0 W heat addition, is the most probable condition corresponding to the experimental measurements for Case 1 (see also Table 3.2). This is also confirmed by the 1D marginalized posterior of the heat source strength shown in Fig. 3.2(b), which peaks at 0 W.

For the heat source height in Fig. 3.2(c), the posteriors generally provide less information gain compared to the prior, and the resulting MAP value of the heat source height is 0.04 m, which is in the exact middle of the prior. As ε decreases, however, a modal value of the heat source height does begin to appear in Fig. 3.2(c) at the maximum possible value of the height allowed by the prior. This modal value ensures that even if a simulation has some small amount of heat addition, the additional heat is moved as far from the burner surface as possible. This is also shown in Fig. 3.3(c), where smaller heat source heights correspond to very small values of the heat source strength, and it is only for larger values of the height that larger values of the strength have significant probabilities. Taken together, these results strongly suggest that there is no additional heat release above the burner for Case 1, since the MAP values of the heat source strength and height are 0 W and 0.04 m, respectively, and non-zero values of the strength are only estimated using ABC when they occur far from the burner surface, where there is little impact on the resulting temperature profiles.

Figures 3.2 and 3.3 show that the posterior distributions for Case 2 are qualitatively similar to those for Case 1. However, the inlet speed estimation for Case 2, corresponding to 0.61 m/s in Fig. 3.2(d), is larger than in Case 1 and is in good agreement with the experimental estimate of $V_0 = 0.65$ m/s for this case. The posteriors for Case 2 in Fig. 3.2(e) and Figs. 3.3(d) and (e)

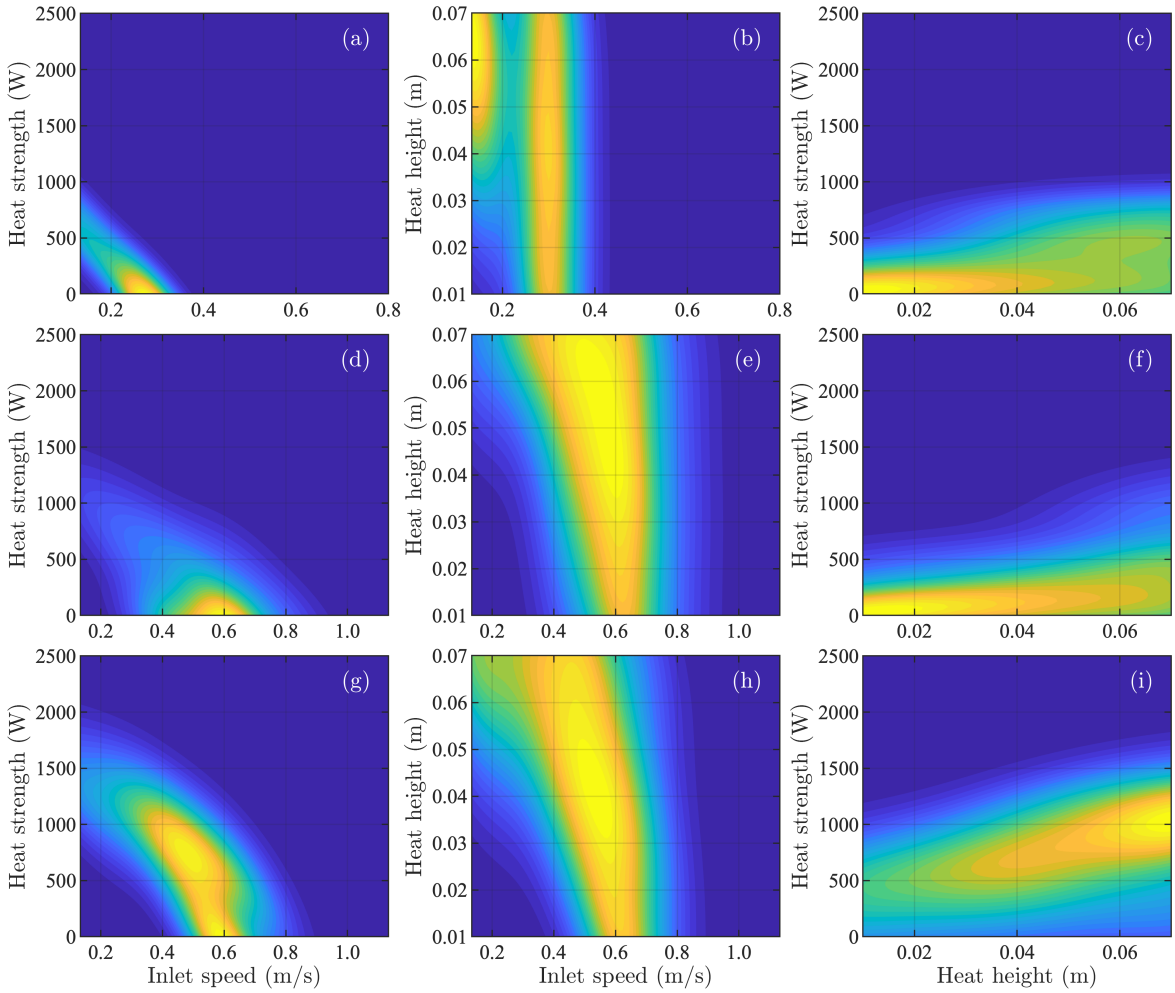

Figure 3.3: Two-dimensional marginalized joint posteriors for Cases 1, 2 and 3 (top, middle, and bottom rows, respectively) when ε is set to accept 5% of simulations. Columns show joint posteriors for heat source strength and inlet speed (left), heat source height and inlet speed (middle), and heat source strength and heat source height (right). Colors represent the density of the posterior, with yellow and blue corresponding to high and low densities, respectively.

indicate that the most probable heat source strength is very small, with a MAP value of 50 W. Once again, there is also relatively little information gained about the most likely heat source height for larger values, with a MAP value of 0.042 m, close to the center of the prior. For smaller values of ε in Fig. 3.2(f) where non-zero values of the heat source strength are permissible for sufficiently small inlet speeds [see Fig. 3.3(d)], the preferred heat source height is pushed far from the burner surface, as shown in Figs. 3.3(e) and (f). These results suggest that there is a possibility of heat

release above the burner for Case 2, but the heat source strength is so small (only 50 W) that it has a nearly negligible effect on the overall temperature profile for this case.

The lack of substantial additional heat release predicted by ABC for Cases 1 and 2 is consistent with previous experimental results [51, 50] that showed no signs of additional combustion in the flow above the burner (i.e., low quantities of OH and no appreciable increase in temperature above the surface). Posteriors for Case 3 are, however, substantially different. In particular, ABC again provides a most probable inlet speed that is consistent with the trends in the experimental estimates [see Fig. 3.2(g)], but the heat source strength now has a modal value between 500 and 1000 W, even for very small values of ε, as shown in Fig. 3.2(h). The marginalized posteriors [e.g., Fig. 3.2(i)] for the heat source height are qualitatively similar to those for Cases 1 and 2, but the MAP value has shifted to a larger value of 0.047 m, away from the center of the prior. The MAP value of the height is now much more significant since it corresponds to a non-zero value of the heat source strength, as shown in Fig. 3.3(i). The non-zero value of the heat source strength indicated by the Case 3 posteriors in Figs. 3.2 and 3.3 thus suggests that there is substantial additional heat release due to continued combustion above the surface at these burner conditions.

It should be noted that the MAP inlet speeds predicted by ABC for Cases 1 and 2 are similar to the estimated bulk flow speeds from the experiments. For Case 3, however, the predicted value is lower than the experimental estimate. It is unclear whether this difference occurs due to the modeling used in the LES, to the approximations used to experimentally estimate inlet speeds (specifically, the assumption that combustion was complete when determining the exit gas composition), or to the fact that there is likely additional heat release above the burner for this case. However, it will be seen in the next section that the lower inlet speed for Case 3, when combined with additional heat release, yields excellent agreement between the LES and experimental results, providing confidence in the accuracy of the parameter estimates in Table 3.2.

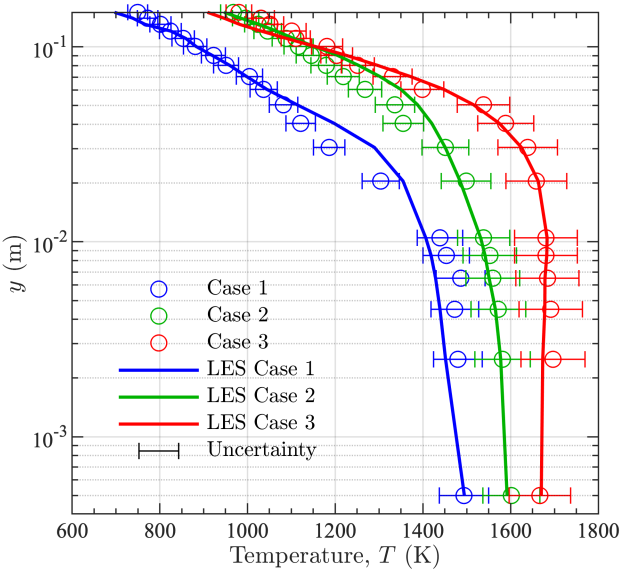

Figure 3.4: Vertical profiles of temporally-averaged, line-of-sight, absorption-weighted temperature from LES using parameters in Table 3.2 (solid lines) and from the LAS (empty circles) for each burner case. Error bars denote experimental uncertainty.

3.4.2 Temperature Profile and Field Comparisons

Using the parameter values in Table 3.2, LES was performed for each of the three experimental burner configurations. The resulting vertical profiles of temperature are shown in Fig. 3.4, along with the corresponding experimental measurements from Fig. 3.1. The LES results generally agree closely with the experimental measurements, including the initial increase, and then rapid decrease, in temperature above the burner for Case 3. It is emphasized that the agreement shown in Fig. 3.4 for Case 3 requires substantial heat addition to account for continued combustion. For Cases 1 and 2, by contrast, reasonable agreement is obtained with the experimental measurements without including additional heat release above the burner, further indicating that continued combustion is unlikely for these cases.

Given the agreement between the simulation and experimental results shown in Fig. 3.4, we can be confident that we are performing LES for equivalent configurations to the experiments. The resulting LES fields of velocity, temperature, and chemical species can then be used to develop a more complete understanding of the real-world catalytic burner system.

3.4.3 Observing System Experiment

As a final test of the predictive power of ABC, an Observing System Experiment (OSE) [126, 11] was conducted. In this test, one of the experimental measurement heights was excluded from the reference summary statistics $\mathcal{S}$ prior to performing ABC. During the ABC procedure, parameter values giving the smallest distances $d(\mathcal{S}, \mathcal{S}')$ were identified, where $\mathcal{S}'$ was again obtained from LES and the RMSE was used for the distance function. The vertical profiles of temperature corresponding to these parameter values were then used to estimate the missing experimental data (which in this case was not used to generate the list of 'best' simulations). This approach thus provides insight into how well ABC can predict missing experimental data.

Here we perform an OSE for each of the three experimental configurations. Because there is an substantial change in the temperature gradient at approximately 1.05 cm above the burner surface, as shown in Fig. 3.4, this measurement height was deemed difficult to predict and was consequently removed from the reference summary statistics prior to performing ABC; similar tests can also be performed excluding other measurement locations, or excluding multiple locations. Once again, ε was set to accept 5% of the sampled parameters.

Figure 3.5 shows the resulting distributions of predicted temperature 1.05 cm above the surface using all simulations, and using only the best 5% of simulations. For Cases 1 and 2 shown in Figs. 3.5(a) and (b), respectively, the modes of the full data distributions fall outside the experimental data ranges of 1439 ± 43 K for Case 1 and 1538 ± 46 K for Case 2. For Case 3 in Fig. 3.5(c), the mode of the full distribution is at the upper end of the experimental range of 1681 ± 50 K.

By contrast, for the best 5% of simulations determined by ABC, the distribution modes are each within the experimental ranges and fall close to the nominal experimental values in each case. The temperatures predicted by ABC are 1433 K, 1550 K, and 1662 K for Cases 1–3, respectively, corresponding to errors of 1% or less compared to the experimental results. It should also be noted that the distributions in Fig. 3.5 are relatively narrow for the best 5% of simulations, with standard

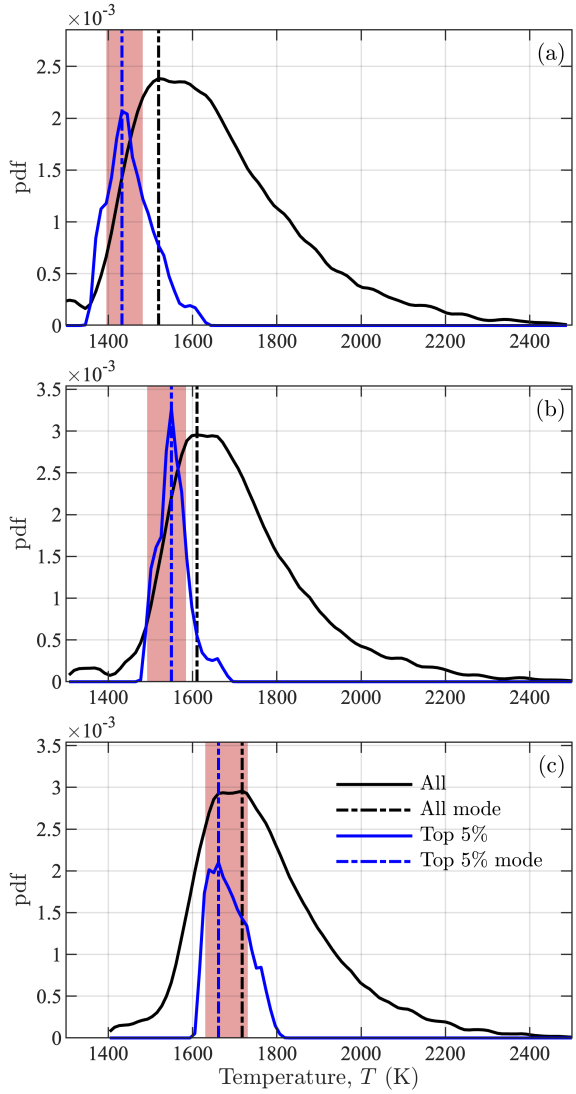

Figure 3.5: Probability density functions (pdfs) of temperature 1.05 cm above the burner from LES for Cases 1–3 (a–c), showing results from all tested parameters (black lines) and from the closest 5% of parameters, as determined using ABC (blue lines). The pdf magnitudes for the top 5% results are decreased by a factor of 4 for display purposes. Modes of the pdfs are shown by the vertical dash-dot lines, and the experimental measurements at this height, with uncertainties of ±3%, are indicated by the red shaded regions.

deviations of 55 K, 38 K, and 45 K for Cases 1–3, respectively, indicating high confidence in the values of temperature predicted by ABC.

This OSE indicates that ABC is extremely effective at providing predictive information within the domain where the simulation and reference data match, even when there is no corresponding

reference data to inform the inference. In future efforts, this approach could be used to design experiments with the fewest possible measurements such that the accuracy of the parameter estimation is unaffected.

3.5 Conclusions

In this chapter, we demonstrated the use of ABC for estimating unknown characteristics of real-world engineering systems, given spatially sparse measurements from experiments. Vertical profiles of temporally averaged absorption-weighted temperature from LAS were combined with ABC and LES to estimate the speed and heat addition characteristics of the high temperature flow created by an industrially relevant catalytic burner. The ABC method was performed for the burner operating at three different conditions, corresponding to different power fluxes and equivalence ratios.

We show that ABC, when given LAS measurements and driven by LES, successfully predicts trends in the inflow speed and also predicts continued combustion above the burner for the case with the highest equivalence ratio. We selected most likely parameter values from the posterior distributions provided by the ABC method and used these values to perform LES of the burner for each of the three burner operating conditions. In each case, the LES results were in close agreement with the experimentally measured vertical profiles of temperature. Additionally, using an OSE, we showed that we were able to successfully predict a missing temperature from the experimental data. We thus demonstrated the utility of the ABC approach for improving knowledge of real-world systems, as well as for improving the physical fidelity of numerical simulations.

This study suggests several directions for future research. In particular, the ABC method should now be tested on more complicated geometries, as well as extended to directly address the chemical composition and subsequent finite rate combustion of the gases leaving the burner. Furthermore, the present ABC approach can be used to simultaneously adjust boundary conditions, fluid properties, and turbulence model parameters in a simulation to achieve a comprehensive improvement in simulation accuracy. Lastly, the OSE performed here suggests that ABC could be

used to design more efficient experimental campaigns with reduced measurement locations.

Chapter 4

Subgrid-Scale Model Calibration Using ABC-MCMC

4.1 Introduction

Large-Eddy Simulations (LES) have the potential to provide a nearly ideal blend of computational accuracy and low cost for the simulation of turbulent flows, but the predictive power of such simulations depends on the accuracy of the closure models used to represent the subgrid scale (SGS) fluxes. Attempts to develop such models from physics principles alone have thus far failed to yield a universally accurate SGS model.

Consequently, the overwhelming majority of LES continues to be performed using classical [107] or dynamic [36] Smagorinsky models, or with artificial dissipation from low-order numerical schemes in what are termed implicit LES approaches. Attempts have been made to find the optimal Smagorinsky constant using an optimization technique [76], Kriging-based response surface [56], and a neural network [100].

However, such simple or non-physical models perform poorly in flows with complex physics (e.g., combustion) and in situations where the fundamental principles underlying LES break down (e.g., in near-wall regions where there is no longer a separation between energy input and dissipation scales). At the same time, attempts to develop more sophisticated models are typically plagued by the presence of many unknown model coefficients, which can be difficult to simultaneously calibrate across different flows. Recently, Safta et al. [98] used a Bayesian approach to estimate a joint distribution for the LES sub-grid scale Yoshizawa model parameters. Here, we apply the ABC-MCMC method to discover model parameters and their uncertainties in nonlinear multi-parameter

SGS closures using higher fidelity direct numerical simulation (DNS) data.

An autonomic closure approach was recently proposed by King et al. [57] as another way to improve upon Smagorinsky-based models. In autonomic closure, test scale filtering is used to provide training data that can be used to determine unknown coefficients in a high-dimensional non-parametric relation for the unclosed stresses. In this sense, autonomic closure can be considered a "data-driven" turbulence closure, except that the training data are provided internally to the simulation, rather than externally from experimental or higher fidelity DNS data. In King et al. [57], a Volterra series [12] was used to represent the closure relation and the unknown coefficients in the series were obtained using an optimization procedure at the test scale. The resulting relation was then applied at the LES grid scale to achieve closure. *A priori* tests [57] using DNS data for homogeneous isotropic turbulence (HIT) have shown that autonomic closure is more accurate at reproducing the exact SGS stress and production fields than a dynamic Smagorinsky model.

The primary challenge in autonomic closure is the need to solve an optimization problem at the test scale, which requires the inversion of large matrices. There are a number of computational algorithms that can perform this procedure with little difficulty, but at the expense of high memory usage. In order to take advantage of the processing surplus available on many modern supercomputers, we propose to substantially reduce the memory requirements of autonomic closure by using approximate Bayesian computation in place of the optimization step.

In the following, we solve the SGS closure inverse problem with the ABC-MCMC approach using DNS as the reference data and provide results for *a priori* and *a posteriori* testing. We also formulate an autonomic closure using the ABC method (ABC-AC) and test it in *a priori* and *a posteriori* tests.

4.2 Subgrid-Scale Closure for Large-Eddy Simulations

Coarse-graining of the Navier Stokes equations using a low pass filter, denoted $\widetilde{(\cdot)}$, at scale Δ gives the LES equations for an incompressible flow, which are written as [74]

$$\frac{\partial \widetilde{u}_i}{\partial x_i} = 0, \qquad \frac{\partial \widetilde{u}_i}{\partial t} + \widetilde{u}_j \frac{\partial \widetilde{u}_i}{\partial x_j} = -\frac{\partial \widetilde{p}}{\partial x_i} + \nu \frac{\partial^2 \widetilde{u}_i}{\partial x_j \partial x_j} - \frac{\partial \tau_{ij}}{\partial x_j}\,, \tag{4.1}$$

where $\widetilde{u}_i$ is the resolved scale velocity, $\widetilde{p}$ is the resolved scale pressure normalized by density, ν is the kinematic viscosity, and τ_{ij} is the unclosed SGS stress tensor given by

$$\tau_{ij} = \widetilde{u_i u_j} - \widetilde{u}_i \widetilde{u}_j\,. \tag{4.2}$$

The grid scale $\widetilde{\Delta}$ is often termed the LES scale since this is the finest scale represented when using the grid discretization as an implicit LES filter. The SGS stress τ_{ij} prevents closure and, in order to solve Eq. (4.1), an appropriate relation for τ_{ij} must be found in terms of resolved scale quantities only.

4.2.1 Inverse Problem with DNS as Reference Data

Closure of Eq. (4.1) can be achieved by modeling the deviatoric part of the stress tensor $\sigma_{ij} = \tau_{ij} - \frac{1}{3}\tau_{kk}\delta_{ij}$, which can be written in terms of an unknown, high-dimensional, non-parametric functional $\mathcal{F}_{ij}$ that takes as its arguments only quantities that can be expressed in terms of the resolved-scale strain rate, $\widetilde{S}_{ij}$, and rotation rate, $\widetilde{R}_{ij}$, tensors; namely [88, 28]

$$\sigma_{ij}(\mathbf{x}, t) \approx \mathcal{F}_{ij}\left[\widetilde{S}_{ij}(\mathbf{x}+\mathbf{x}', t-t'), \widetilde{R}_{ij}(\mathbf{x}+\mathbf{x}', t-t')\right] \quad \text{for all } \mathbf{x}' \text{ and } t' \geq 0, \tag{4.3}$$

where the resolved-scale strain and rotation rate tensors are given by

$$\widetilde{S}_{ij} = \frac{1}{2}\left(\frac{\partial \widetilde{u}_i}{\partial x_j} + \frac{\partial \widetilde{u}_j}{\partial x_i}\right), \quad \widetilde{R}_{ij} = \frac{1}{2}\left(\frac{\partial \widetilde{u}_i}{\partial x_j} - \frac{\partial \widetilde{u}_j}{\partial x_i}\right). \tag{4.4}$$

It should be noted that the closure relation in Eq. (4.3) allows SGS stresses at location and time $(\mathbf{x}, t)$ to depend on the resolved-scale strain and rotation rates, as well as their products, at any point in the flow and at any prior time.

As outlined by King et al. [57], the nonparametric functional $\mathcal{F}_{ij}$ in Eq. (4.3) can be written as a Volterra series [12] or any other appropriate high-dimensional nonparametric functional. Although the Volterra series has been used previously to demonstrate the accuracy of autonomic closure [57], the exact nonparametric representation of $\mathcal{F}_{ij}$ can vary and is not fundamental.

As a demonstration of the ABC approach for determining SGS model coefficients, here we will use the single point, single time nonlinear model introduced by Pope [88], which is given for generic strain and rotation rate tensors, S_{ij} and R_{ij} [following similar definitions to those in Eq. (4.4)], as

$$\mathcal{F}_{ij}(S_{ij}, R_{ij}) = \sum_{\lambda=1}^{4} c_\lambda G_{ij}^{(\lambda)} \,, \tag{4.5}$$

where c_λ are coefficients that can depend on invariants of S_{ij}, R_{ij}, and their products up to second order. It should be noted that the original formulation by Pope [88] extends to fifth order, but here the model is truncated to second order for simplicity. The tensor bases $G_{ij}^{(\lambda)}$ are formed from products of S_{ij} and R_{ij} up to second order; namely [88]

$$G_{ij}^{(1)} = S_{ij} \,, \qquad G_{ij}^{(3)} = S_{ik}S_{kj} - \frac{1}{3}\delta_{ij}S_{kl}S_{kl} \,,$$
$$G_{ij}^{(2)} = S_{ik}R_{kj} - R_{ik}S_{kj} \,, \qquad G_{ij}^{(4)} = R_{ik}R_{kj} - \frac{1}{3}\delta_{ij}R_{kl}R_{kl} \,.$$

In order to obtain $\widetilde{G}_{ij}^{(\lambda)}$ at the LES grid scale, S_{ij} and R_{ij} are replaced by the appropriate resolved scale values of the strain and rotation rate tensors [as given in Eqs. (4.4)].

Using data from experiments or direct numerical simulations (DNS), $\sigma_{ij}(\mathbf{x}, t)$ can be calculated and denoted as reference data $\mathcal{D}$. Thus, we obtain the inverse problem

$$\mathcal{F}_{ij}(\mathbf{c}) = \mathcal{D} \,, \tag{4.6}$$

where the model parameters of $\mathcal{F}_{ij}$ must be determined through an appropriate inversion technique.

4.2.2 Autonomic Closure as an Inverse Problem

The same functional from Eq. (4.3) can also be used to write down the closure relation at a test scale $\widehat{\Delta}$, where $\widehat{\Delta} > \widetilde{\Delta}$, as

$$\widehat{\sigma}_{ij}(\mathbf{x}, t) \approx \mathcal{F}_{ij}\left[\widehat{\widetilde{S}}_{ij}(\mathbf{x}+\mathbf{x}', t-t'), \widehat{\widetilde{R}}_{ij}(\mathbf{x}+\mathbf{x}', t-t') \forall\, \mathbf{x}' \text{ and } t' \geq 0\right] . \tag{4.7}$$

The deviatoric test scale stress tensor is then given by $\widehat{\sigma}_{ij} = T_{ij} - \frac{1}{3}T_{kk}\delta_{ij}$ where $T_{ij} = \widehat{\widetilde{u}_i\widetilde{u}_j} - \widehat{\widetilde{u}}_i\widehat{\widetilde{u}}_j$ represents the test scale stress tensor. The test scale strain and rotation rate tensors are written as

$$\widehat{\widetilde{S}}_{ij} = \frac{1}{2}\left(\frac{\partial\widehat{\widetilde{u}}_i}{\partial x_j} + \frac{\partial\widehat{\widetilde{u}}_j}{\partial x_i}\right), \quad \widehat{\widetilde{R}}_{ij} = \frac{1}{2}\left(\frac{\partial\widehat{\widetilde{u}}_i}{\partial x_j} - \frac{\partial\widehat{\widetilde{u}}_j}{\partial x_i}\right). \tag{4.8}$$

Here, and in the following, $\widehat{(\cdot)}$ denotes a low-pass filter at test scale $\widehat{\Delta}$. In order to obtain $\widehat{G}_{ij}^{(\lambda)}$ at the test scales, respectively, S_{ij} and R_{ij} are replaced by the appropriate test scale values of the strain and rotation rate tensors [as given in Eq. (4.8)].

The advantage of using LES and test scales is that now we can calculate $\widehat{\sigma}_{ij}$ using only LES data and we do not need to have DNS or experimental data. Thus, denoting reference data $\widehat{\sigma}_{ij}$ as $\mathcal{D}_{\text{LES}}$ we obtain the inverse problem

$$\mathcal{F}_{ij}(\mathbf{c}) = \mathcal{D}_{\text{LES}}\,, \tag{4.9}$$

and the model parameters of $\mathcal{F}_{ij}$ can be determined through an appropriate inversion technique.

Once $\mathcal{F}_{ij}$ is known at the test scale $\widehat{\Delta}$, it is then projected to the grid scale $\widetilde{\Delta}$. The resulting closure approach is similar to dynamic versions of classical closures such as the Smagorinsky model [35, 62] and to scale-similarity models such as that by Bardina et al. [2], except that the relation $\mathcal{F}_{ij}$ is high-dimensional and nonparametric. That is, any of the terms or components in $\mathcal{F}_{ij}$ could be deemed unimportant during the inversion procedure, resulting in a fundamentally different functional form.

In King et al. [57], optimization and a least squares technique were used to solve for the unknown coefficients in the Volterra series formulation of $\mathcal{F}_{ij}$. However, the inversion process was memory intensive and no uncertainty measures for the values of the unknown coefficients in $\mathcal{F}_{ij}$ were obtained. Here we instead use ABC combined with MCMC methods to determine $\mathcal{F}_{ij}$.

4.2.3 Approximate Bayesian Computation Autonomic Closure (ABC-AC)

Using concepts from autonomic closure and ABC, we propose the following combined closure approach, denoted ABC-AC, at a particular time t. Here we neglect the use of prior time steps for simplicity; the ABC-AC approach is easily extended to include information at earlier times.

Note that in the following, we assume that an appropriate relation containing a set of N unknown coefficients has already been selected for $\mathcal{F}_{ij}$. Moreover, we also assume that an N-dimensional prior joint pdf has been formulated as an estimate of the distribution of the unknown coefficients; typically, these priors are formulated as uniform or Gaussian distributions. The steps involved in application of the ABC-AC approach to closure of the LES equations are as follows:

(1) Filter resolved scale quantities $\widetilde{u}_i$ and $\widetilde{p}$ in order to obtain test scale quantities $\widehat{\widetilde{u}}_i$ and $\widehat{\widetilde{p}}$.

(2) Compute test scale deviatoric stresses $\widehat{\sigma}_{ij}$ using resolved scale quantities $\widetilde{u}_i$.

(3) Using $\widehat{\sigma}_{ij}$ as truth data $\mathcal{D}_{\text{LES}}$, run the ABC algorithm (Algorithm 2) to obtain a joint posterior distribution of model parameters.

(4) From the estimated posterior, choose the modal value of the parameters; these parameters then give a statistically-accurate estimate for $\mathcal{F}_{ij}$.

(5) Apply $\mathcal{F}_{ij}$ at the LES scale to achieve closure.

4.3 Reference Data

In this section, we apply the ABC-MCMC approach outlined in Chapter 2 to the inverse problem stated in Section 4.2. The reference data in the following examples are taken as a 256^3 subsample of 1024^3 pseudospectral HIT DNS data at $Re_\lambda = 433$ from the John Hopkins Turbulence Database [61]. The filtering required in *a priori* tests is accomplished using spectrally sharp filtering at $k_{\widetilde{\Delta}} = 30$ for LES filtering and at $k_{\widehat{\Delta}} = 15$ for test filtering. Example velocity fields and SGS stresses σ_{ij} at the LES scale for pseudospectral are shown on Figure 4.1.

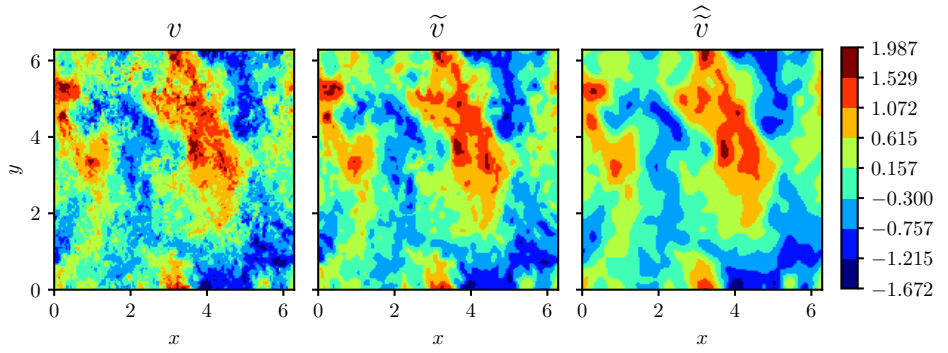

(a) Velocity fields at the full DNS resolution, and at LES and test scales (left to right).

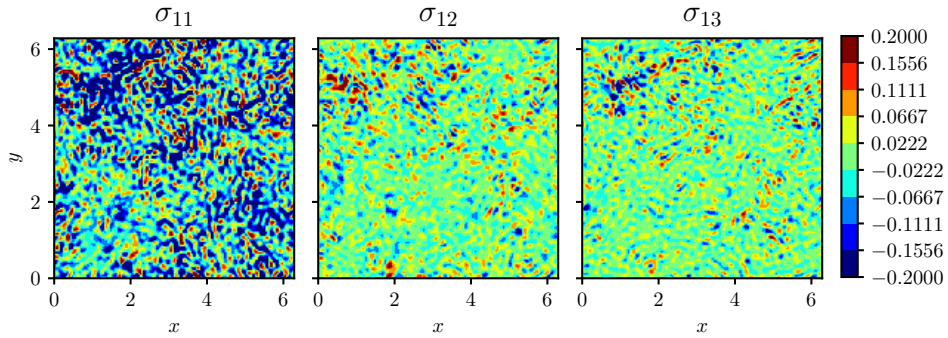

(b) SGS deviatoric stress (σ_{ij}) fields at the LES scale.

Figure 4.1: Example velocity fields and SGS stresses σ_{ij} at the LES scale for pseudospectral HIT data [61] used in *a priori* testing.

4.4 Summary Statistics and Statistical Distance

The summary statistics $\mathcal{S}$ used in the ABC-MCMC analysis are pdfs of the deviatoric stresses σ_{ij} and a pdf of the production $P = \sigma_{ij}S_{ij}$. Since the model still does not exactly represent the flow physics, we can consider the result of the model to have some uncertainty due to the modeling. To introduce this uncertainty, we randomly pick 10^5 data points out of 256^3 for each iteration in the ABC-MCMC algorithm to calculate modeled summary statistics. This makes our model stochastic and reduces the amount of computations.

Summary statistics of the deviatoric stresses, denoted as $\mathcal{S}_\sigma$, consist of six pdfs $\mathcal{S}_{ij}$, one pdf for each i, j component of the stress tensor. We calculate these pdfs on [-0.3, 0.3]. The statistical distance $d(\mathcal{S}'_\sigma, \mathcal{S}_\sigma)$ can be calculated many different ways. Here we show results using the Mean

Square Error (MSE) of the logarithms of the pdfs. The MSE distance is given by

$$d(\mathcal{S}'_\sigma, \mathcal{S}_\sigma) = \sum_{i,j|j\geq i} d\left(\mathcal{S}'_{ij}, \mathcal{S}_{ij}\right) = \sum_{i,j|j\geq i} \left(\ln \mathcal{S}'_{ij} - \ln \mathcal{S}_{ij}\right)^2, \tag{4.10}$$

where the summation is over all i and j such that $j \geq i$, which gives six independent terms in the summation; this summation approach is necessary since the stress tensors are symmetric and the terms with $i \neq j$ should not be double counted in the combined distance metric.

Another common statistical distance is the Kullback-Leibler (KL) divergence. Autonomic closure results provide the comparison of KL and MSE distances. The KL distance is given by

$$d^{\mathrm{KL}}(\mathcal{S}'_\sigma, \mathcal{S}_\sigma) = \sum_{i,j|j\geq i} d\left(\mathcal{S}'_{ij}, \mathcal{S}_{ij}\right) = \sum_{i,j|j\geq i} \left(\mathcal{S}_{ij} \left|\ln \mathcal{S}_{ij} - \ln \mathcal{S}^{\mathcal{F}}_{ij}\right|\right) . \tag{4.11}$$

It is emphasized that, in the present tests, $\mathcal{S}_{ij}$ represents the pdf of the reference deviatoric stresses and $\mathcal{S}'_{ij}$ represents the pdf of the modeled deviatoric stresses.

Summary statistics of the production field, $P = \sigma_{ij} S_{ij}$, are denoted as $\mathcal{S}_P$, which is a pdf of the production field. The production pdfs are calculated on [-5, 5]. Thus, the distance function is simply the MSE distance between the logarithms of the reference pdf $\mathcal{S}_P$ and the logarithms of modeled pdf $\mathcal{S}'_P$,

$$d(\mathcal{S}'_P, \mathcal{S}_P) = \left(\ln \mathcal{S}'_P - \ln \mathcal{S}_P\right)^2 . \tag{4.12}$$

4.5 Results with DNS as Reference Data

4.5.1 *A Priori* Testing

The *a posteriori* distribution of the SGS closure coefficients in Eq. (4.5) is calculated using the ABC-MCMC algorithm described in Section 2.3 and the DNS data described in Section 4.3 as reference data. It should be noted that we use only 10^5 data points to evaluate the modeled pdfs in the ABC-MCMC algorithm. Then the maximum *a posteriori* distribution (MAP) estimate is used as the proposed parameter vector for the SGS closure model.

In *a priori* testing, we evaluate the model using the sampled parameters and all 256^3 data

points and directly compare the modeled deviatoric stresses and production pdfs with the corresponding pdfs of the reference data.

We start with a demonstration of the *a posteriori* distribution and *a priori* testing results for the training procedure using only deviatoric stresses summary statistics. However, despite the fact that Eq. (4.5) models the deviatoric stresses, it is important that the model can correctly reproduce not only the deviatoric stresses pdfs but also the dissipation process. One of the advantages of the proposed algorithm is that the statistics it is trained on can be easily changed. Taking this into account, we also demonstrate how the proposed coefficients change if a posterior distribution is obtained using only production summary statistics, or a combination of deviatoric stresses and production summary statistics.

4.5.1.1 Training on deviatoric stresses

First, we ensure that for a first-order simplification of the closure relation in Eq. (4.5), the approach can recover the coefficient C_S used in the Smagorinsky model [107]. We then obtain coefficients for the three- and four-parameter second-order truncations of Eq. (4.5) (the fourth basis function, $G_{ij}^{(4)}$ is sometimes omitted in second-order stress models) and show their posterior pdfs.

For the first-order version of the full model in Eq. (4.5), it can be shown based on the classical Smagorinsky model that $c_1 = -2(C_S\Delta)^2|\widetilde{S}|$ where C_S is the Smagorinsky coefficient and $|\widetilde{S}| \equiv \sqrt{2\widetilde{S}_{ij}\widetilde{S}_{ij}}$. The first order model can thus be written as

$$\sigma'_{ij} = C_1\Delta^2|\widetilde{S}|\widetilde{S}_{ij}\,, \tag{4.13}$$

where C_1 is the unknown that will be estimated using the MCMC-ABC approach.

It should be noted that an expected value of C_S can be obtained from the DNS data using kinetic energy arguments, giving

$$C_S^2 = \left[\frac{\varepsilon}{\Delta\langle|\widetilde{S}|^3\rangle}\right], \tag{4.14}$$

where $\varepsilon = 2\nu S_{ij}S_{ij}$ is the true kinetic energy dissipation rate and $\langle\cdot\rangle$ is an average. Using this relation, the data give $C_S = 0.22$. In order for the ABC-MCMC approach to be deemed successful, it should recover a value close to this C_S.

For the first-order model, we sampled 10^3 samples of C_1 from a uniform prior. The parameter value resulting in the minimum distance is $C_1 = -0.0639$, which gives $C_S = \sqrt{-C_1/2} = 0.18$. This value for C_S is reasonably close to the dissipation-based value $C_S = 0.22$ from Eq. (4.14).

A similar analysis can be performed for the second-order model from Eq. (4.5). The calibration step used 10^3 and 10^4 samples for the three- and four-parameter models, respectively, and a uniform prior was initially bounded as $C_1 \in [-0.3, 0.0]$, $C_2 \in [-0.5, 0.5]$, $C_3 \in [-0.2, 0.2]$ and $C_4 \in [-0.2, 0.2]$.

Figure 4.2 shows the resulting posterior pdfs for a three-parameter second-order model, and Figure 4.3 shows the posterior pdfs corresponding to a four-parameter model. In order to facilitate visualization of these posteriors, we show marginal pdfs for each parameter on diagonal subplots. 2D marginalized joint pdfs are shown on overdiagonal subplots and conditional pdfs are shown on subplots below the diagonal.

For both three- and four-parameter cases, the three- or four-dimensional posterior pdfs, respectively, are calculated using kernel density estimation (KDE) with a Gaussian kernel and bandwidth defined by Scott's Rule [104, 105].

For the three-parameter model, the ABC-MCMC approach provides a value of C_1 close to -0.069, resulting in a value of $C_S = 0.186$ and for the four-parameter case $C_1 = -0.0432$, which corresponds to $C_S = 0.147$. The marginal pdfs for C_2 are bimodal with peaks at $C_2 = \pm 0.1$; this indicates that the sign of C_2 is of no importance compared to the magnitude. The marginal pdf of C_3 in the three-parameter case peaks near zero, indicating that this term is of negligible importance compared to the other two terms in the three-term second-order closure relation. Finally, in the four-parameter model, the marginal pdf of C_3 and C_4 in Figure 4.3 are symmetric and strongly correlated. This strong correlation is a good example of when the proposal kernel with adaptive covariance (see Section 2.3.1) can improve the acceptance rate of the ABC-MCMC algorithm.

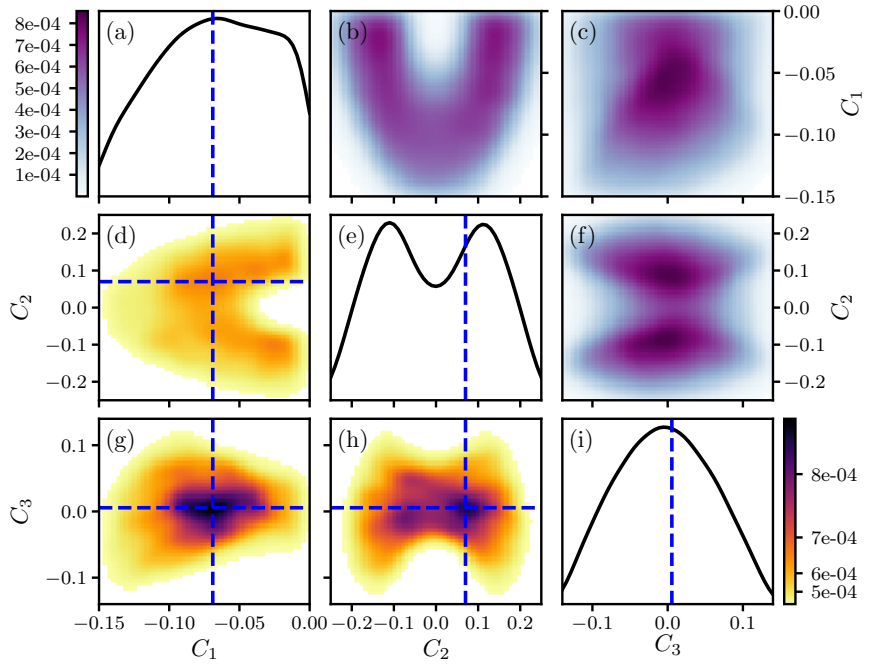

Figure 4.2: Marginal and joint probability density functions of accepted values of C_1, C_2, and C_3 for the three-term second order model from Eq. (4.5) trained using pdf of σ_{ij} as summary statistics.

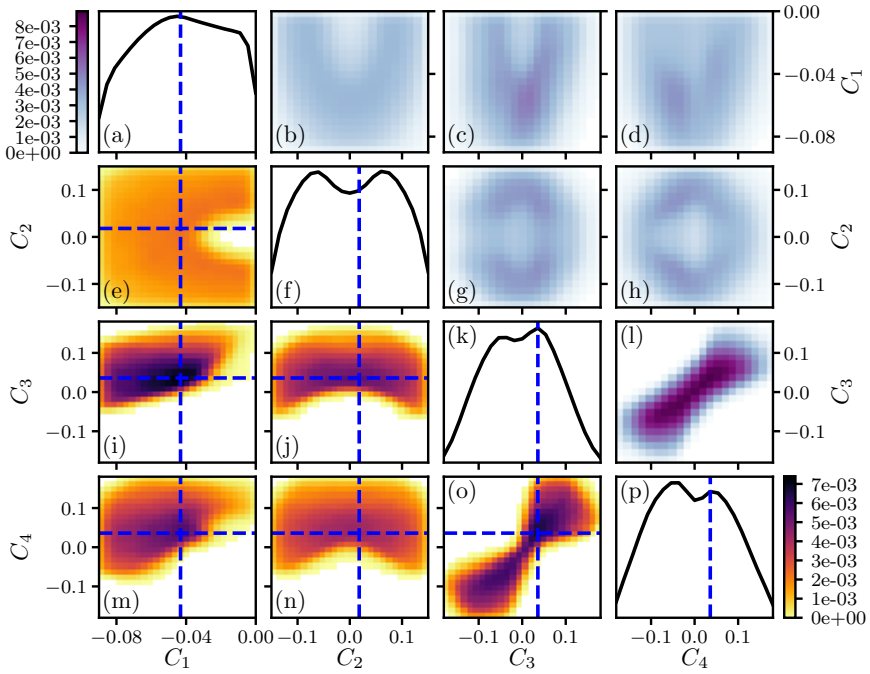

Figure 4.3: Marginal and joint probability density functions of accepted values of C_1, C_2, C_3, and C_4 for the four-term second order model from Eq. (4.5) trained using pdf of σ_{ij} as summary statistics.

		C_1	C_2	C_3	C_4
Trained on sigma	3 parameters	-0.069	0.07	0.00556	–
	4 parameters	-0.0432	0.018	0.036	0.036
Trained on production	3 parameters	-0.0474	-0.036	-0.2886	–
	4 parameters	-0.0366	-0.09	-0.1262	0.2158
Trained on sigma and production	3 parameters	-0.0402	0.27	-0.1598	–
	4 parameters	-0.0318	–0.0144	-0.198	-0.198

Table 4.1: MAP values from joint probability density functions.

The maximums of the three- or four-dimensional posterior pdfs are taken as the estimated parameters for the model. These MAP parameters are shown in Figures 4.2 and 4.3, and the values are listed in Table 4.1. A comparison between truth and MAP modeled summary statistics are shown in Figure 4.8(a). The performance of the four-parameter model is improved in comparison to the three-parameter model. This demonstrates that the fourth basis function, $G_{ij}^{(4)}$ is important in the second-order model. We can see that despite good agreement in the deviatoric stresses pdfs, the model cannot correctly reproduce back-scattering (positive production). This limitation is caused by training only on deviatoric stresses pdfs without taking into account the correct modeling of the dissipation process.

4.5.1.2 Training on Production

In this section, we focus only on the correct modeling of the dissipation process and use only the production pdf as a summary statistic for the ABC-MCMC algorithm. We provide results for the three- and four-parameter models from Eq. (4.5).

Similar to training on the deviatoric stresses summary statistics, the calibration step uses 10^3 and 10^4 samples for the three- and four-parameter models, but a uniform prior was initially bounded as $C_1 \in [-0.3, 0.0]$, $C_2 \in [-0.5, 0.5]$, $C_3 \in [-0.5, 0.2]$ and $C_4 \in [-0.2, 0.5]$.

Figures 4.4 and 4.5 show the resulting posterior pdfs for the three- and four-parameter second-order models. The marginal pdf of C_2 is no longer bimodal in the four-parameter model, and it peaks near zero, indicating that this term is of negligible importance compared to the other three

terms in the four-term second-order closure relation.

Summary statistics produced by the three- and four-parameter models with the MAP parameters (Figure 4.8 (b)) match production pdf reasonably well, but the deviatoric stresses pdfs have worse agreement, especially for the diagonal elements of the tensor. This shows that training only on the production pdf is not sufficient to correctly reproduce the deviatoric stresses.

4.5.1.3 Training on a Combination of Deviatoric Stresses and Production

The ABC-MCMC algorithm flexibility also allows us to combine summary statistics. Thus, we can train the algorithm on both the deviatoric stresses and production summary statistics simultaneously. Thus, our acceptance criterion is:

$$\left[\alpha\, d(\mathcal{S}'_\sigma, \mathcal{S}_\sigma) + \beta\, d(\mathcal{S}'_P, \mathcal{S}_P)\right] \leq \varepsilon\,, \tag{4.15}$$

where α and β are weights. One can change these weights according to the importance of different summary statistic components. For the three-parameter model, we used $\alpha = 1$ and $\beta = 3$.

Similar to the previous case, the calibration step used 10^3 and 10^4 samples for the three- and four-parameter models, respectively, and a uniform prior was initially bounded as $C_1 \in [-0.3, 0.0]$, $C_2 \in [-0.5, 0.5]$, $C_3 \in [-0.5, 0.2]$ and $C_4 \in [-0.5, 0.5]$. Figures 4.6 and 4.7 show the resulting posterior pdfs for the three- and four-parameter second-order models. The marginal pdf of C_2 in the four-parameter case is no longer bimodal and peaks near zero, indicating that this term is of negligible importance compared to the other three terms in the four-term second-order closure relation.

Finally, the comparison of truth and MAP modeled summary statistics (Figure 4.8 (c)) demonstrates that the second order model from Eq. (4.5) cannot satisfy matching both deviatoric stresses and production pdfs simultaneously.

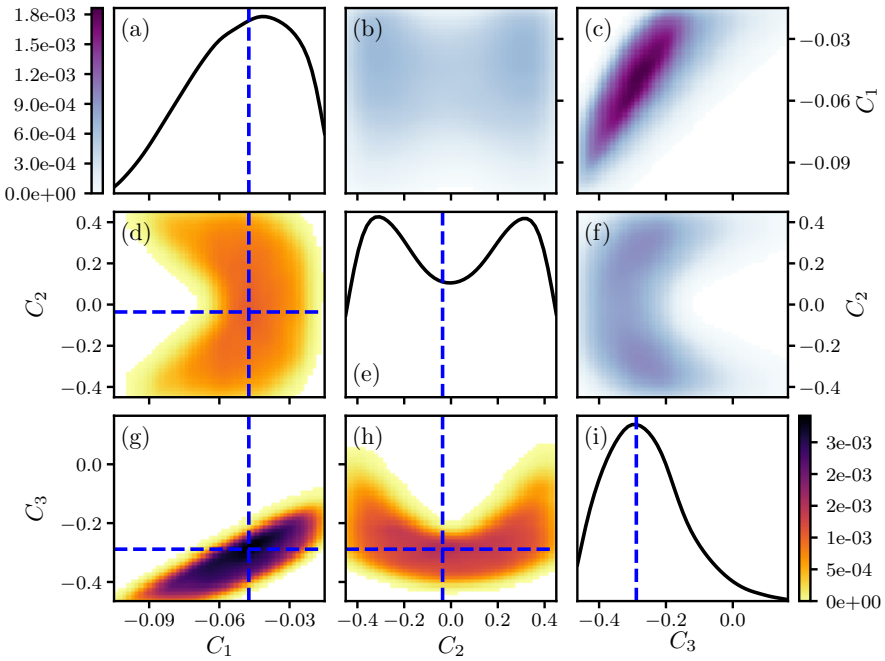

Figure 4.4: Marginal and joint probability density functions of accepted values of C_1, C_2, and C_3 for the three-term second-order model from Eq. (4.5) trained using pdf of production $\sigma_{ij}S_{ij}$ as summary statistics.

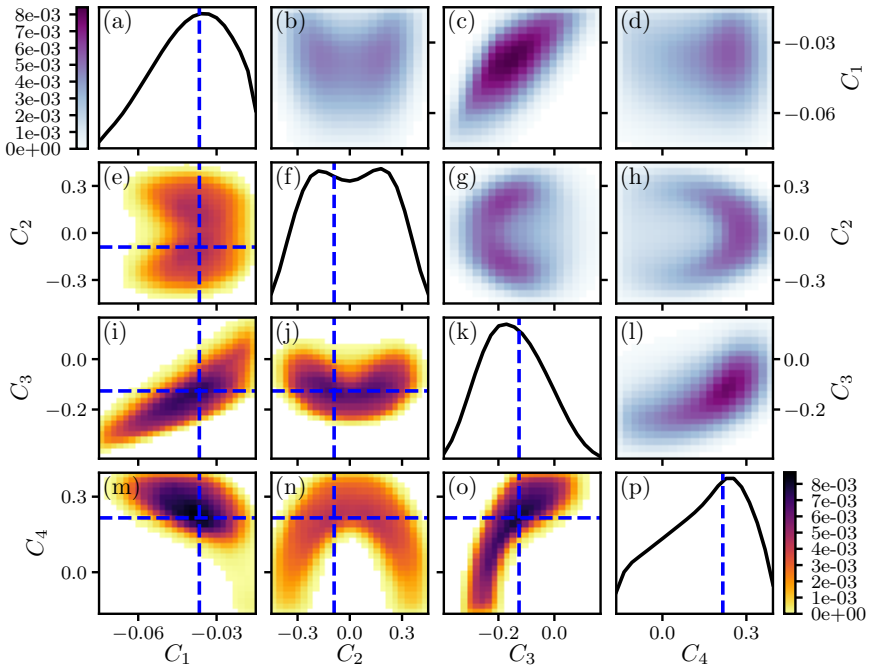

Figure 4.5: Marginal and joint probability density functions of accepted values of C_1, C_2, C_3, and C_4 for the four-term second-order model from Eq. (4.5) trained using pdf of production $\sigma_{ij}S_{ij}$ as summary statistics.

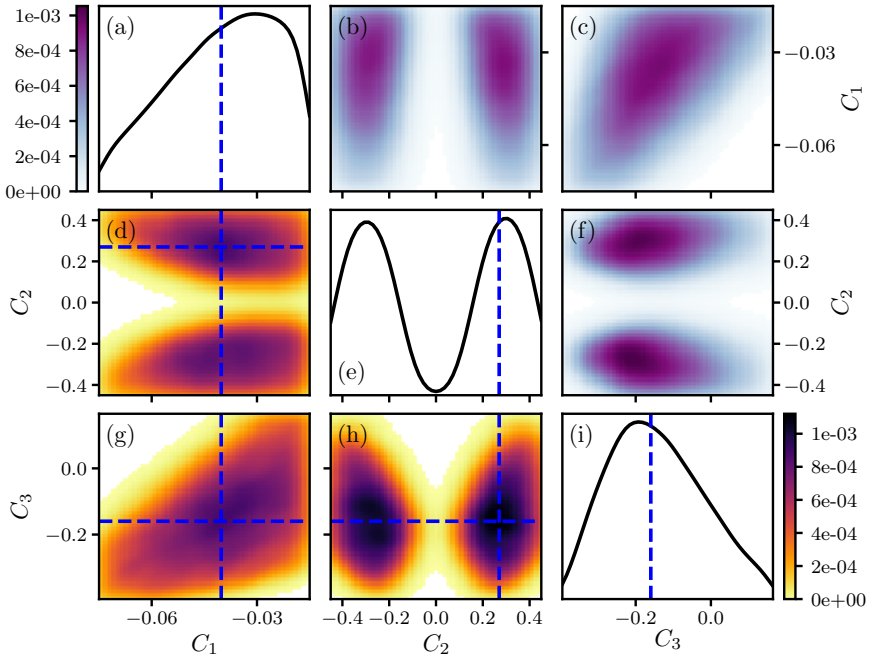

Figure 4.6: Marginal and joint probability density functions of accepted values of C_1, C_2, and C_3 for the three-term second order model from Eq. (4.5) trained using a combination of production pdf $\sigma_{ij}S_{ij}$ and pdf of σ_{ij} as summary statistics.

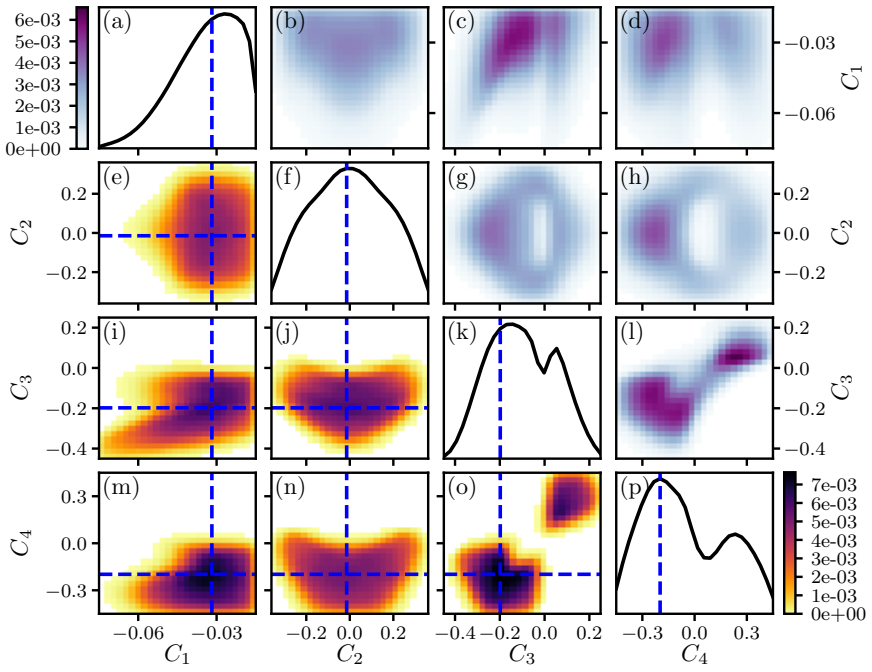

Figure 4.7: Marginal and joint probability density functions of accepted values of C_1, C_2, C_3, and C_4 for the four-term second order model from Eq. (4.5) trained using a combination of production pdf $\sigma_{ij}S_{ij}$ and pdf of σ_{ij} as summary statistics.

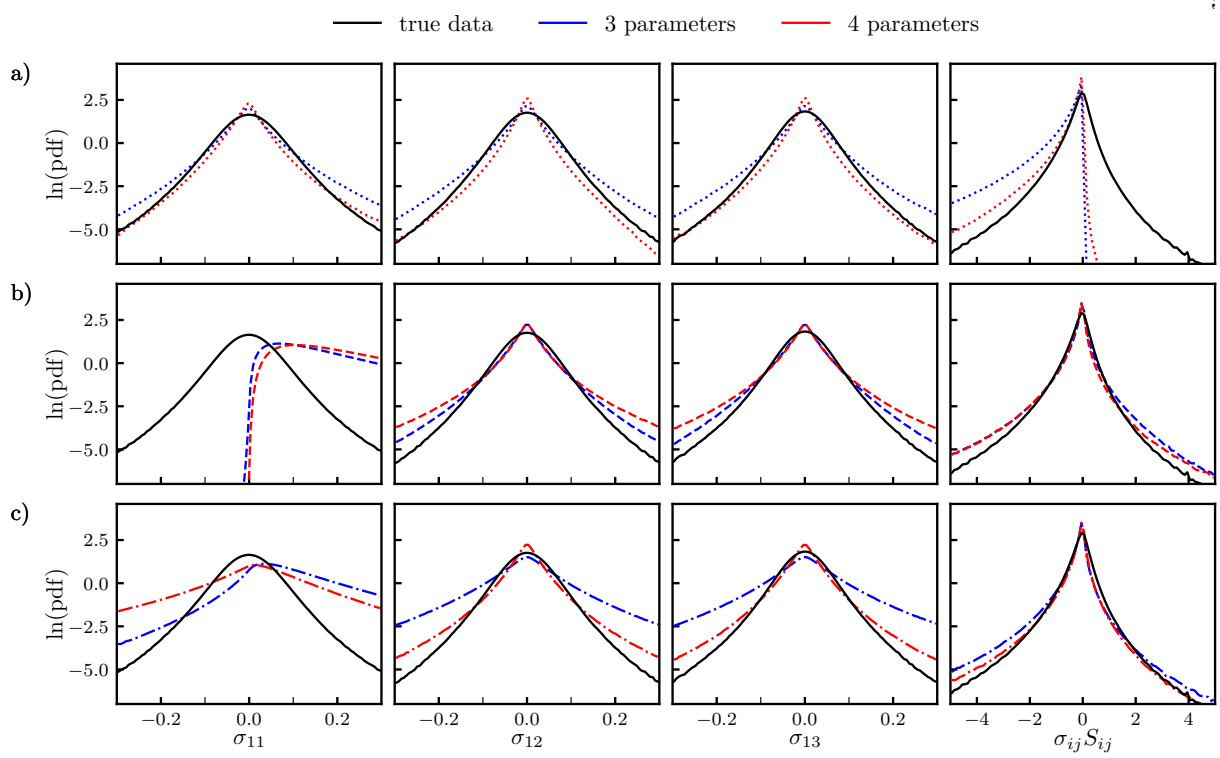

Figure 4.8: The comparison of truth summary statistics $\mathcal{S}_\sigma$ and $\mathcal{S}_P$ with modeled summary statistics $\mathcal{S}'_\sigma$ and $\mathcal{S}'_P$ produced by three- and four-parameter model with the MAP parameters.

4.5.2 *A Posteriori* Testing

A posteriori testing was performed using `spectralLES`[1] , a pseudospectral LES solver for model testing and development written in pure Python that is based on an open-source, pure Python code, `spectralDNS`, [2] written by Mortensen and Langtangen [77]. Initial *a posteriori* tests have focused on whether models learned from the ABC approach can be stably integrated into forward LES runs. Second, we compared the deviatoric stresses and production pdfs from these LES runs with the corresponding pdfs from the reference DNS data.

Simulations were initialized using a random initial velocity field with a prescribed isotropic energy spectrum, and turbulence is subsequently sustained using spectrally-truncated linear forcing of wavenumber shells $k = 2$ and $k = 3$. Simulations were performed using the same domain, energy

[1] https://github.com/phamlington/teslapy/tree/master/spectralLES
[2] https://github.com/spectralDNS/spectralDNS/blob/master/spectralDNS3D_short.py

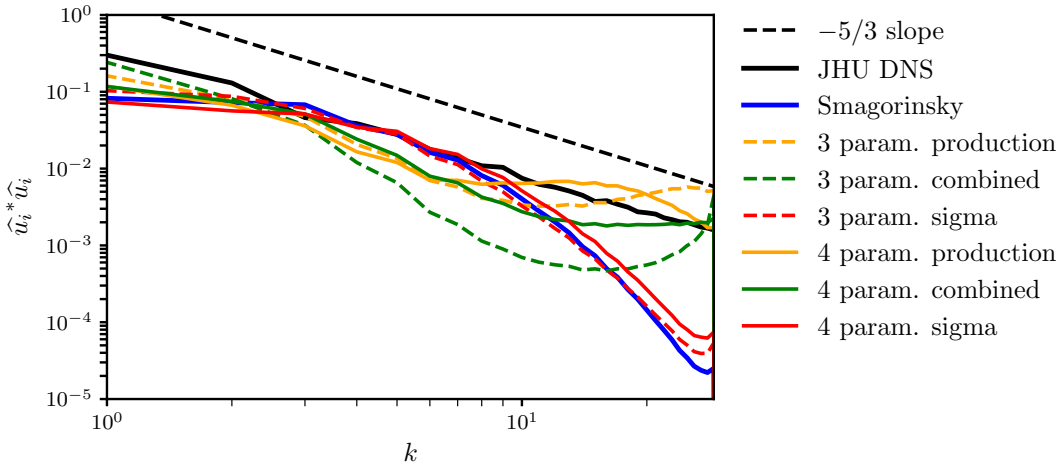

Figure 4.9: Spectra of HIT LES forward runs with MAP model parameters from Table 4.1.

injection rate, viscosity, and LES filter scale as the DNS data described in Section 4.3 used for model learning and using a 64^3 uniform grid. For comparison, we also ran a simulation using the static Smagorinsky model with the standard Smagorinsky constant value $C_S =?$.

The resulting kinetic energy spectra of the HIT LES simulations with model coefficients defined as MAP values from Table 4.1 are shown in Fig. 4.9. Parameters trained on the deviatoric stresses summary statistics result in spectra similar to the Smagorinsky model spectra, while the spectra of simulations with parameters trained on production tend to have higher values for higher wavenumbers. This is caused by the fact that training on the production pdf causes the algorithm to match production and dissipation at the LES scale only.

To study the propagation of uncertainty in the model parameters in forward runs, we sampled 100 parameter sets from each of the six posterior pdfs reported in Section 4.5.1 using a Monte Carlo acceptance-rejection method and ran the described above HIT LES simulations for each of these parameter sets. Figure 4.10 shows the resulting kinetic energy spectra distributions for stable forward runs. Figure 4.12 shows the resulting distribution of deviatoric and production pdfs for the four-parameter case.

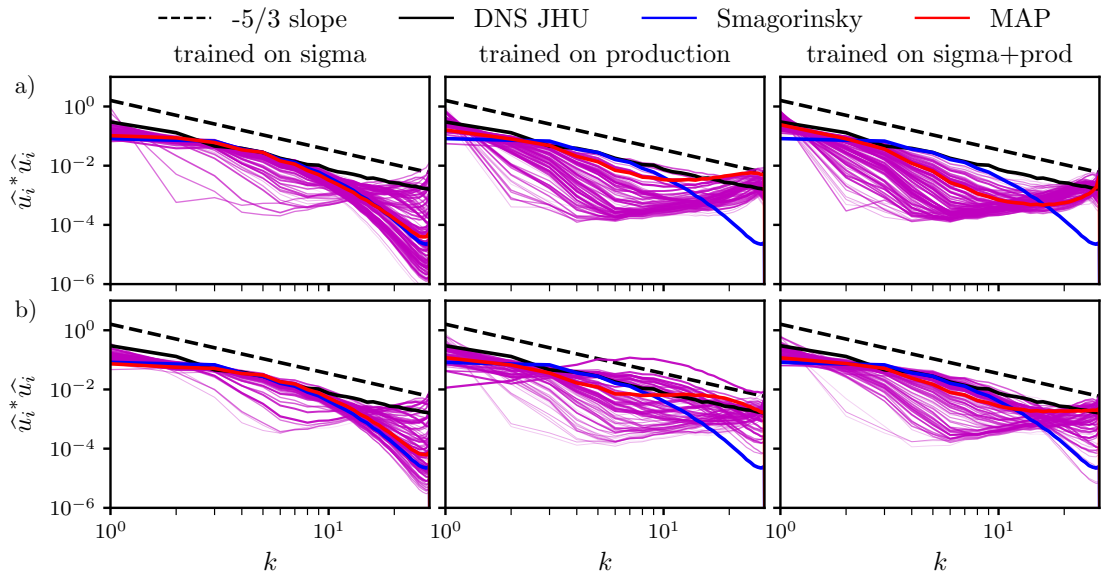

Figure 4.10: Spectra distributions of stable forward runs: a) three parameters models, b) four parameters models. The intensity of magenta lines indicates the probability of each set to be sampled from posterior distribution.

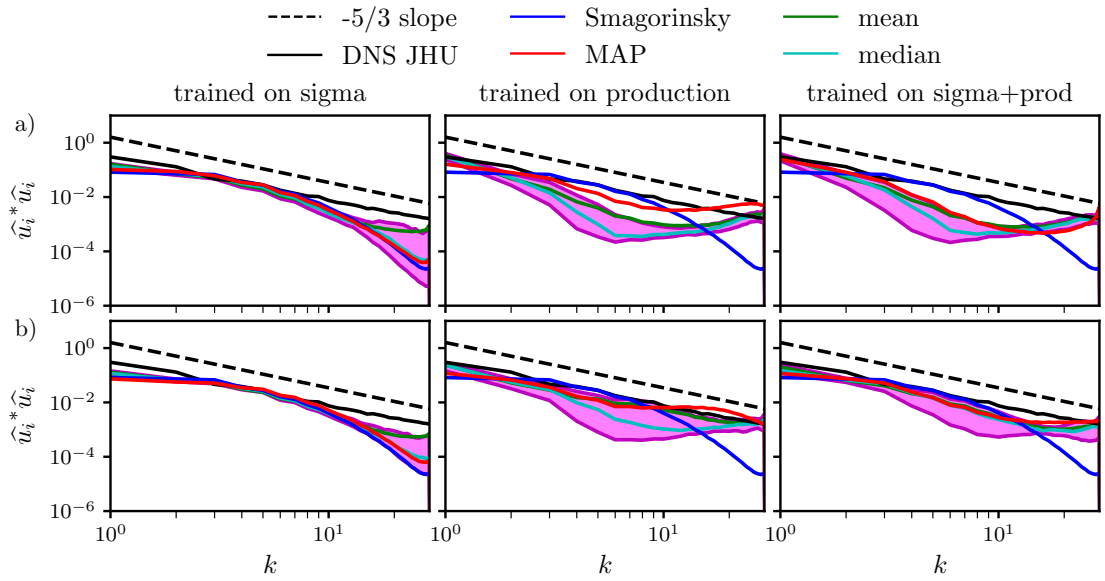

Figure 4.11: Statistical characteristics of spectra distributions of stable forward runs. Shaded area shows 75% confidence interval for each wavenumber k: a) three-parameters model, b) four-parameters model.

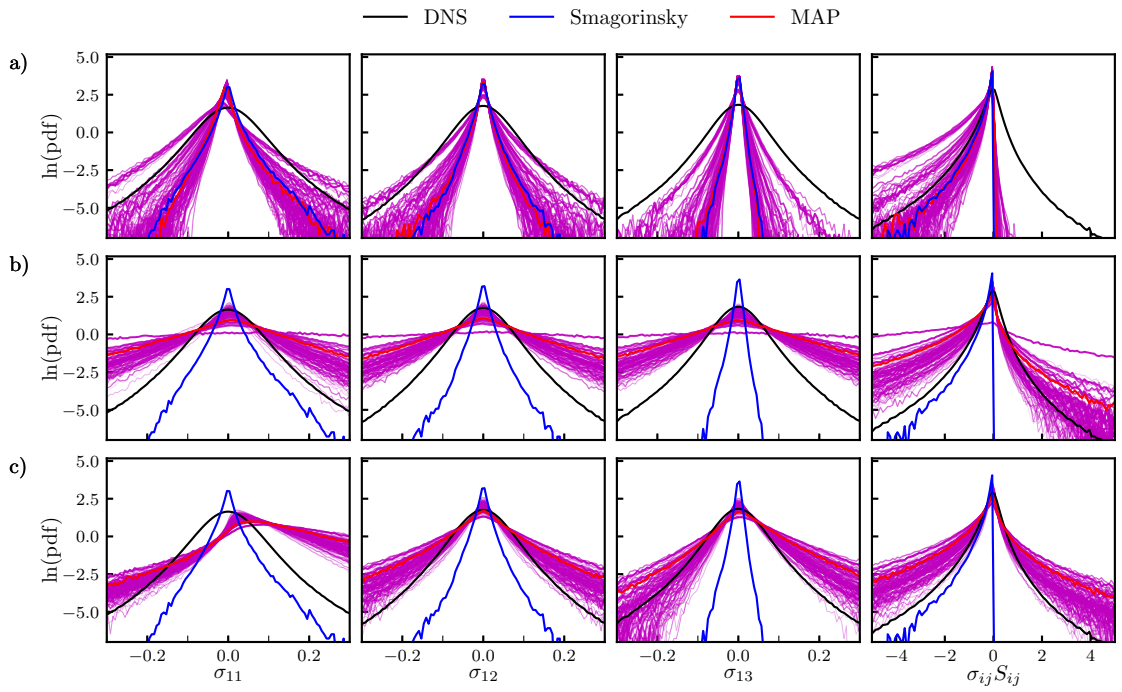

Figure 4.12: Distribution of Reynolds stresses pdf and production pdf for four-parameter model: a)trained on sigma summary statistic, b) trained on production summary statistic and c) trained on combination of sigma and production summary statistics.

4.6 Autonomic Closure Results

In the following, *a priori* tests of the ABC-AC approach are performed using the same HIT DNS data described in Section 4.3. First, we ensure that for a first-order simplification of the closure relation in Eq. (4.5), the approach can recover the coefficient C_S used in the Smagorinsky model. We then obtain coefficients from a three-term second-order truncation of Eq. (4.5) and show that the resulting model can be stably integrated in forward runs.

4.6.1 *A Priori* Testing

Both first-order and the three-term second-order versions of the full model in Eq. (4.5) are tested here, giving the test-scale representations

$$\widehat{\sigma}'_{ij} = c_1 \widehat{\widetilde{S}}_{ij} \quad \text{[1st order]}\,, \tag{4.16}$$

$$\widehat{\sigma}'_{ij} = c_1 \widehat{\widetilde{S}}_{ij} + c_2 \left(\widehat{\widetilde{S}}_{ik} \widehat{\widetilde{R}}_{kj} - \widehat{\widetilde{R}}_{ik} \widehat{\widetilde{S}}_{kj} \right) + c_3 \left(\widehat{\widetilde{S}}_{ik} \widehat{\widetilde{S}}_{kj} - \frac{1}{3} \delta_{ij} \widehat{\widetilde{S}}_{kl} \widehat{\widetilde{S}}_{lk} \right) \quad \text{[2nd order]}\,. \tag{4.17}$$

Analogous to models in Section 4.5, it can be shown that $C_1 = -2(C_S \widehat{\Delta})^2 |\widehat{\widetilde{S}}|$ where C_S is the Smagorinsky coefficient and $\widehat{\widetilde{S}} \equiv \left(2 \widehat{\widetilde{S}}_{ij} \widehat{\widetilde{S}}_{ij} \right)^{1/2}$. In order to facilitate comparisons with prior work, we similarly rewrite Eqs. (4.16) and (4.17) in terms of C_S as

$$\widehat{\sigma}'_{ij} = -2(C_S \widehat{\Delta})^2 |\widehat{\widetilde{S}}| \widehat{\widetilde{S}}_{ij}\,, \tag{4.18}$$

$$\widehat{\sigma}_{ij} = -2(C_S \widehat{\Delta})^2 |\widehat{\widetilde{S}}| \widehat{\widetilde{S}}_{ij} + C_2 \widehat{\Delta}^2 \left(\widehat{\widetilde{S}}_{ik} \widehat{\widetilde{R}}_{kj} - \widehat{\widetilde{R}}_{ik} \widehat{\widetilde{S}}_{kj} \right) + C_3 \widehat{\Delta}^2 \left(\widehat{\widetilde{S}}_{ik} \widehat{\widetilde{S}}_{kj} - \frac{1}{3} \delta_{ij} \widehat{\widetilde{S}}_{kl} \widehat{\widetilde{S}}_{lk} \right)\,, \tag{4.19}$$

where $\widehat{\Delta}$ is introduced into the last two terms in order to render C_2 and C_3 non-dimensional. Note that since $\mathcal{F}_{ij}$ is expressed here using parametric functions, these preliminary tests do not provide a full demonstration of the power of ABC-AC, but are nevertheless important as initial tests of the method.

The statistics used in the ABC analysis are pdfs of the test scale deviatoric stresses $\widehat{\sigma}_{ij}$ (as shown in Figure 4.13), which are denoted $\mathcal{S}_{ij}$ since there is a pdf for each (i, j) component of the stress tensor. It is emphasized that, in the present tests, $\mathcal{S}_{ij}$ represents the pdf of truth $\widehat{\sigma}_{ij}$ and $\mathcal{S}'_{ij}$ represents the pdf of modeled $\widehat{\sigma}'_{ij}$, both of which are computed at the test scale $\widehat{\Delta}$.

Analogous to Eq. (4.14) but using test scale filter size $\widehat{\Delta}$ and strain rate tensor $\widehat{\widetilde{S}}$ instead of LES scale quantities, we obtain the true expected $C_S = 0.22$.

For the first order model, Figure 4.14 shows how the distance $d(\mathcal{S}'_{ij}, \mathcal{S}_{ij})$ depends on C_S for $N = 1000$ samples of C_S from its uniform prior $U(0, 0.4)$, using a tolerance of $\varepsilon = 25$ for the KL distance and $\varepsilon = 150$ for the MSE distance. In both cases, the parameter value resulting in the minimum distance is close to the true value $C_S = 0.22$. More specifically, the values obtained are $C_S \approx 0.216$ for the KL distance and $C_S \approx 0.215$ for the MSE distance. These values of C_S

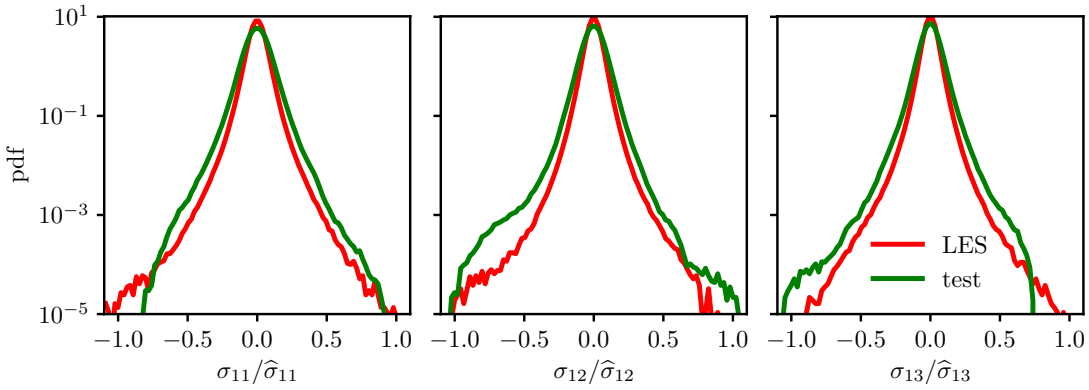

Figure 4.13: Probability density functions of the deviatoric stresses at LES (red lines) and test (green lines) scales, denoted σ_{ij} and $\widehat{\sigma}_{ij}$, respectively.

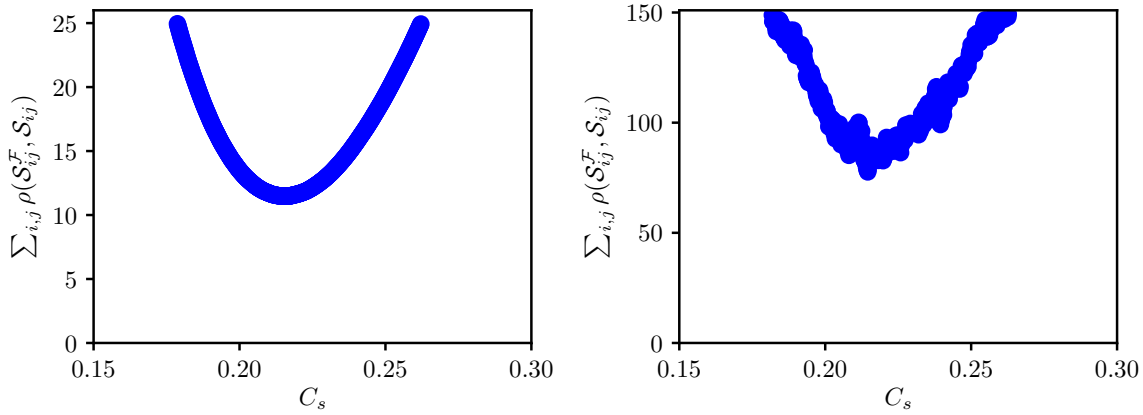

(a) KL distance, $C_S = 0.216$

(b) MSE distance, $C_S = 0.215$

Figure 4.14: Accepted values for the C_S parameter in the first order model and corresponding statistical distances.

determined at the test filter scale can then be applied at the LES (i.e., grid) scale to approximate the unclosed stresses σ_{ij}, namely

$$\sigma_{ij}^{\mathcal{F}} = -2(C_S\widetilde{\Delta})^2|\widetilde{S}|\widetilde{S}_{ij}\,. \tag{4.20}$$

Figure 4.15 shows the resulting pdfs of σ_{ij} and σ'_{ij}, revealing reasonable agreement between the modeled and true stresses at the LES scale.

A similar analysis for the second-order model in Eq. (4.19) gives the posterior pdfs shown in Figure 4.16. In order to facilitate visualization of the three dimensional posterior, marginalized

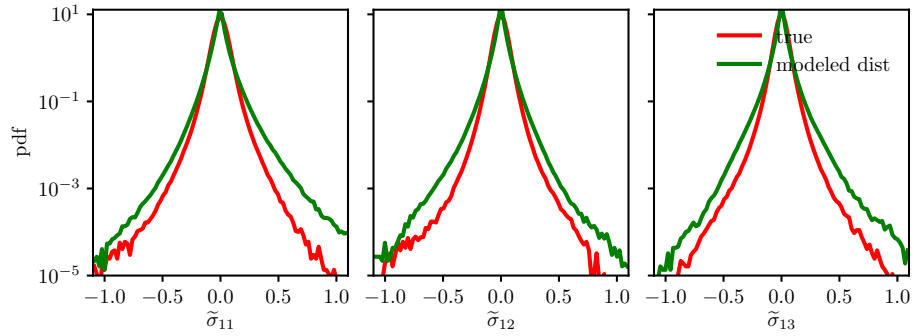

(a) KL distance, $C_S = 0.216$

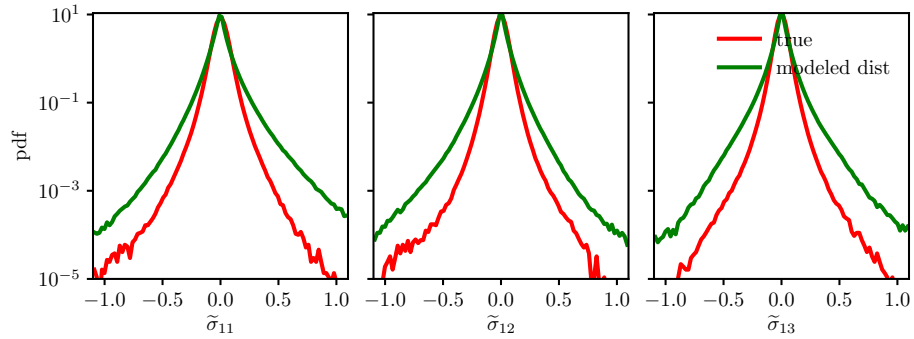

(b) MSE distance, $C_S = 0.215$

Figure 4.15: Probability density functions of stresses $\sigma_{ij}^{\mathcal{F}}$ from the one-parameter first order model in Eq. (4.18) at the LES scale (green lines) and the true LES scale stresses σ_{ij} from the DNS (red lines).

joint pdfs over one and two parameters are shown for each of C_S, C_2 and C_3. Both the mode and mean of the marginal pdf for C_S show that, once again, the ABC approach provides a value of C_S close to 0.2. The marginal pdf for C_2 is bimodal with peaks at $C_2 = \pm 0.1$. Finally, the marginal pdf of C_3 peaks near 0, indicating that this term is of negligible importance compared to the other two terms in the second order closure relation.

Using the values of C_i that give the minimum distance in the statistics, the second order model parameters at the test scale are found to be

$$C_s = 0.18\,, \quad C_2 = -0.088\,, \quad C_3 = -0.0015\,. \tag{4.21}$$

These values can then be applied at the LES scale to give the pdfs of σ'_{ij} at the LES scale shown in Figure 4.17. Once again, the second order model gives close agreement between the modeled and

true stresses.

4.6.2 *A Posteriori* Testing

Using the parameter values identified in the previous section, *a posteriori* testing of the learned model is performed using pseudospectral LES solver, named `spectralLES`, described in Section 4.5.2. Initial *a posteriori* tests have simply focused on whether models learned from the ABC approach can be stably integrated in forward runs, and Figure 4.18 shows that, using the second order model with coefficients given in Eq. (4.21), kinetic energy spectra converge to a stable spectrum at sufficiently long times.

4.7 Conclusions

Approximate Bayesian computation and Markov chain Monte Carlo methods have been used to estimate parameter values, as well as their uncertainties, in subgrid-scale closure models for LES of turbulent flows. The models tested include nonlinear SGS closures with up to four parameters. *A priori* tests results using homogeneous isotropic turbulence have been presented. *A posteriori* results are presented for each discovered model using the `spectraLES`.

We have also provided initial results for an autonomic closure approach using approximate Bayesian computation. Using test-scale filtering, the closure method is able to determine, on the fly, a non-parametric relation for the subgrid-scale stresses at the test scale and then uses this relation at the LES grid scale to achieve closure. Initial *a priori* and *a posteriori* tests on homogeneous isotropic turbulence indicate that the new approach can be used to accurately and stably close the LES equations. Compared to prior implementations of autonomic closure, this approach has low memory requirements and instead relies on the substantial processing power available on GPGPUs. This shift in computational load is achieved using approximate Bayesian computation, a relatively new technique for determining unknown parameters in high dimensional problems.

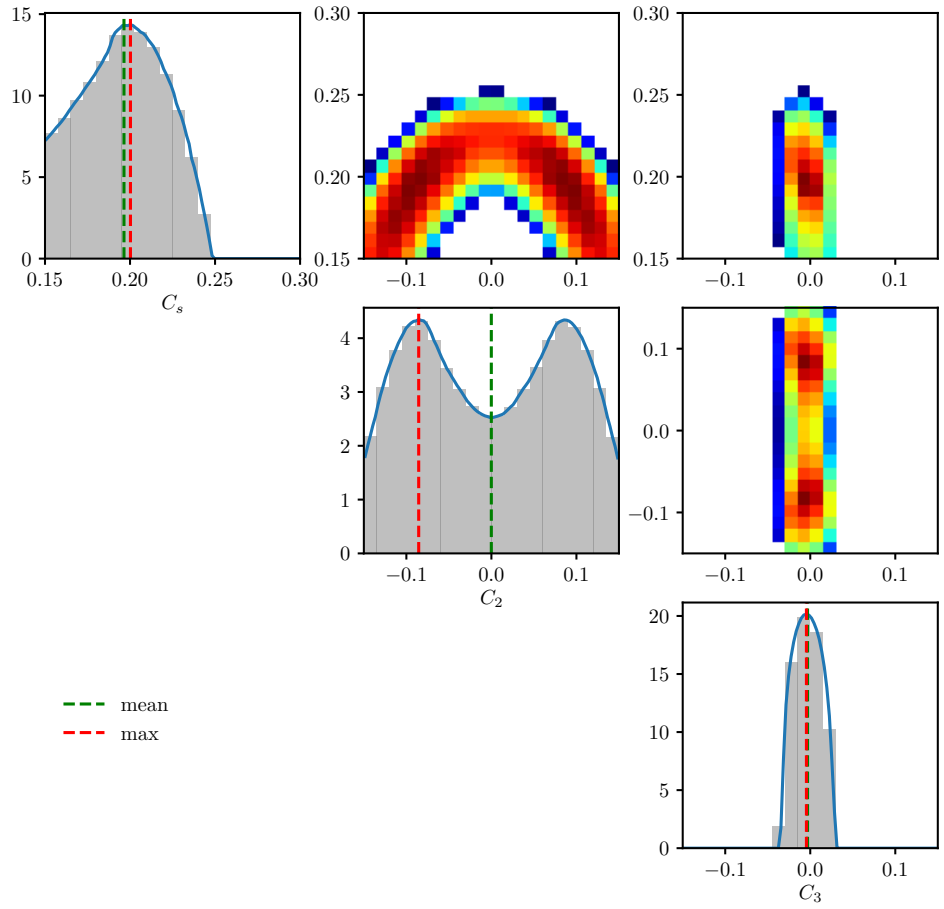

Figure 4.16: Marginal and joint probability density functions of accepted values of C_S, C_2, and C_3 for the second order model in Eq. (4.19) at the test scale. Dashed green lines show the mean of each marginal pdf, and dashed red lines show the location of the MAP.

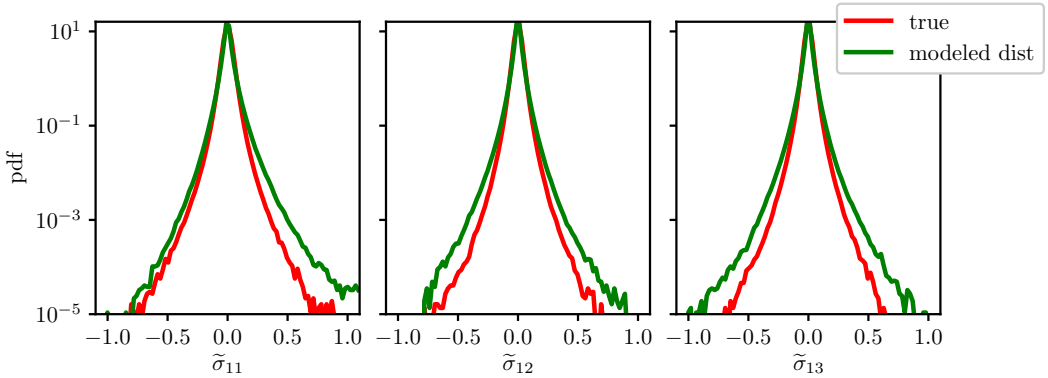

Figure 4.17: Probability density functions of stresses σ'_{ij} from the three-parameter second order model in Eq. (4.19) at the LES scale (green lines) and the true LES scale stresses σ_{ij} from the DNS (red lines).

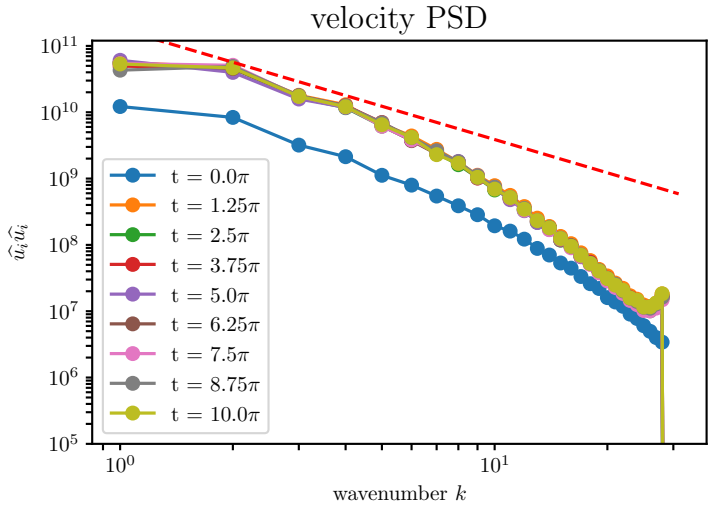

Figure 4.18: Kinetic energy spectra obtained from LES of HIT using `spectraLES` and the second-order model with coefficients from Eq. (4.21).

Chapter 5

Nonequilibrium Turbulence Model Calibration Using ABC-MCMC

5.1 Introduction

The overwhelming majority of Reynolds averaged Navier-Stokes (RANS) simulations continue to be performed using classical equilibrium models, such as the k-ε and k-ω models (see Speziale and So [110] for a review), where the Boussinesq (or gradient transport) hypothesis is used to relate the unclosed Reynolds stresses to the local instantaneous mean strain rate tensor via an isotropic eddy viscosity. However, these models are known to perform poorly in flows with even moderately complex physics, and particularly in flows with rapid spatial or temporal variations in mean flow properties [46, 47, 44, 45]. At the same time, attempts to develop more sophisticated models are typically plagued by the presence of many unknown model parameters, which can be difficult to simultaneously calibrate.

The present chapter outlines the use of the ABC-MCMC method to determine unknown parameters and their uncertainties in a four-parameter RANS closure model that is specifically intended for use in simulations of nonequilibrium flows where the Reynolds stress anisotropy tensor is misaligned with the local instantaneous mean strain rate tensor (thereby precluding the use of an isotropic eddy viscosity and traditional equilibrium closures).

In the following, we briefly describe the nonequilibrium RANS model, review the test cases considered and present the model parameter estimations. Conclusions and directions for future work are provided at the end.

5.2 Description of Nonequilibrium Turbulence Model

Application of an ensemble average to the Navier-Stokes equations yields the RANS equations, which are expressed for an incompressible constant viscosity flow as

$$\frac{\partial \overline{u}_i}{\partial t} + \overline{u}_j \frac{\partial \overline{u}_i}{\partial x_j} = -\frac{1}{\rho}\frac{\partial \overline{p}}{\partial x_i} + \frac{\partial}{\partial x_j}\left(2\nu \overline{S}_{ij}\right) - \frac{\partial}{\partial x_j}\left(\overline{u_i' u_j'}\right) , \tag{5.1}$$

where $\overline{S}_{ij} = (1/2)(\partial \overline{u}_i/\partial x_j + \partial \overline{u}_j/\partial x_i)$ is the mean strain rate tensor and $\overline{u_i' u_j'}$ is the unclosed Reynolds stress tensor. The Reynolds stress can be written in terms of isotropic and anisotropic (or deviatoric) parts as

$$\overline{u_i' u_j'} = \frac{2}{3} k \delta_{ij} + k a_{ij} , \tag{5.2}$$

where k is the turbulence kinetic energy and a_{ij} is the Reynolds stress anisotropy tensor. Because the governing equation for k includes relatively few unclosed terms, the primary challenge in RANS modeling is to represent the tensor a_{ij}, which is unclosed. A number of models have been proposed for this tensor, including various nonlinear eddy viscosity models [37, 118, 34], but by far the most widely used models continue to be equilibrium models where it is assumed that $a_{ij} \propto \overline{S}_{ij}$. Such models include the classical k-ε and k-ω models as well as their many variants (see Speziale and So [110] for a review).

However, it is now widely understood that equilibrium models become inaccurate in complex flows, and, in particular, those flows with rapid spatial and temporal variations in mean flow properties [46]. Such "nonequilibrium" turbulent flows arise in many practical applications, including supersonic and hypersonic vehicles where interactions occur between shock waves and turbulent boundary layers as well as internal combustion engines where pistons rapidly strain the flow. The nonequilibrium turbulence effects introduced in such flows can be significant and require new modeling approaches.

5.2.1 Nonequilibrium Anisotropy Closure

The nonequilibrium turbulence model considered here was identified by Hamlington and Ihme [45] as a nearly ideal model, in terms of both accuracy and computational simplicity, for capturing

the effects of rapid straining in piston-driven and rapidly-compressed flows. This model is expressed as

$$\frac{\partial a_{ij}}{\partial t} + \overline{u}_k \frac{\partial a_{ij}}{\partial x_k} = -\alpha_1 \frac{\varepsilon}{k} a_{ij} + \alpha_2 \overline{S}_{ij} \,, \tag{5.3}$$

where ε is the kinetic energy dissipation rate and the coefficients α_1 and α_2 are given by

$$\alpha_1 = \frac{P}{\varepsilon} - 1 + C_1 \,, \quad \alpha_2 = C_2 - \frac{4}{3} \,, \tag{5.4}$$

where $P \equiv -k a_{ij} \overline{S}_{ij}$ is the kinetic energy production rate. The model parameters C_1 and C_2 in Eq. (5.4) have traditionally been tied to the choice of pressure-strain correlation model [58, 111], but here they will be treated as unknowns determined by the ABC-MCMC procedure.

It should be noted that the model in Eq. (5.3) has a rigorous basis in the exact anisotropy transport equation and accounts for both the return to isotropy of unstrained turbulence [i.e., the first term on the right-hand side of Eq. (5.3)] and the generation of anisotropy in strained turbulence [i.e., the second term on the right-hand side of Eq. (5.3)]. This model is also the basis for the quasi-analytical nonequilibrium anisotropy model outlined in [46, 47].

All of the test cases considered here are homogeneous, which permits subtantial simplifications to the RANS and anisotropy closure equations. In particular, since spatial derivatives of turbulent fluctuating variables are identically zero in homogeneous turbulence, the Reynolds stresses have no effect on the evolution of $\overline{u}_i$ in Eq. (5.1) and the spatial derivative of a_{ij} on the left-hand side of Eq. (5.3) is also identically zero. As a result, for homogeneous flows where $\overline{S}_{ij}$ varies in time only, the evolution of a_{ij} is given by

$$\frac{da_{ij}}{dt} = \left(\frac{k}{\varepsilon} a_{ij} \overline{S}_{ij} + 1 - C_1 \right) \frac{\varepsilon}{k} a_{ij} + \left(C_2 - \frac{4}{3} \right) \overline{S}_{ij} \,, \tag{5.5}$$

where $a_{ij} = a_{ij}(t)$ is a function of time only and Eq. (5.4) has been used to replace the α_i coefficients appearing in Eq. (5.3). Similarly, in homogenenous turbulent flows $k = k(t)$ and $\varepsilon = \varepsilon(t)$ also depend only on time and their dynamics are represented here using the standard equations employed

in classical k-ε models; namely

$$\frac{dk}{dt} = -ka_{ij}\overline{S}_{ij} - \varepsilon\,, \tag{5.6}$$

$$\frac{d\varepsilon}{dt} = -C_{\epsilon 1}\varepsilon a_{ij}\overline{S}_{ij} - C_{\epsilon 2}\frac{\varepsilon^2}{k}\,, \tag{5.7}$$

where $C_{\varepsilon 1}$ and $C_{\varepsilon 2}$ are additional unknown parameters that will be learned using the ABC-MCMC procedure.

The system of nonlinear and coupled ordinary differential equations represented by Eqs. (5.5)–(5.7) constitutes the nonequilibrium turbulence anisotropy closure examined in this study. Quantities of interest resulting from this model, such as turbulence kinetic energy and anisotropy magnitude, are denoted $\mathcal{F}(\mathbf{c})$ and depend on the unknown model parameters $\mathbf{c} = (C_1, C_2, C_{\epsilon 1}, C_{\epsilon 2})$.

5.2.2 Stochastic Modeling

The nonequilibrium anisotropy closure described in the previous section is strictly deterministic given appropriate initial conditions and a prescribed temporally varying mean strain rate tensor $\overline{S}_{ij}(t)$. However, as described by Oliver and Moser [83], treating the coefficients of the turbulence model as random variables accounts only for the uncertainty in those coefficients but does not account for the uncertainty in the model itself.

Following Oliver and Moser [83], because the present nonequilibrium model still does not exactly represent the flow physics, we can consider the result of the model to have some uncertainty due to the modeling. Then the following form represents the stochastic model

$$\mathcal{F}(\mathbf{c}, \theta) = \mathcal{F}(\mathbf{c}) + \epsilon(\theta), \tag{5.8}$$

where $\mathbf{c}$ is, once again, a vector of turbulence model parameters and ϵ is a random vector field depending on the random parameter θ.

5.2.3 Inverse Problem

Using reference data $\mathcal{D}$ from experiments or higher fidelity simulations, we can write the inverse problem

$$\mathcal{F}(\mathbf{c}, \theta) = \mathcal{D}\,, \tag{5.9}$$

where the model parameters $\mathbf{c}$ must be determined through an appropriate inversion technique. Once again, both $\mathcal{F}$ and $\mathcal{D}$ represent quantities of interest such as the turbulence kinetic energy k. Due to the complexity of the model, inversion of Eq. (5.9) is made difficult using optimization approaches. Here we instead use ABC, combined with MCMC methods, to determine $\mathbf{c}$.

5.3 Description of Nonequilibrium Homogeneous Test Cases

The nonequilibrium anisotropy closure described in Section 5.2 is applied here to predict the turbulence response in a range of different nonequilibrium homogeneous turbulence test cases which are grouped into two categories: (i) impulsively strained turbulence, and (ii) periodically-sheared turbulence. Four different straining cases are considered in the first category, and five different shearing frequencies are considered in the second category.

5.3.1 Impulsively-Strained Turbulence

For each of the impulsively-strained cases considered here, the turbulence is assumed to be initially isotropic and unstrained such that $a_{ij} = 0$ and $\overline{S}_{ij} = 0$ for $t < 0$. For $t \geq 0$, the turbulence is then subjected to a constant mean strain rate tensor $\overline{S}_{ij}$ with a characteristic magnitude S. At time $t = 0$, it is assumed that $k = k_0$ and $\varepsilon = \varepsilon_0$, and the initialization of each case is completed by defining Sk_0/ε_0. The four impulsively-strained cases examined here correspond to different forms of $\overline{S}_{ij}$ and comprise the pure shear case from Bardina et al. [3] as well as the plane strain, axisymmetric expansion, and axisymmetric contraction cases from Lee and Reynolds [59], as outlined in the following. It should be noted that each of these cases were also examined by Girimaji [37].

- *Pure shear:* Reference data are available from the large-eddy simulation (LES) by Bardina et al. [3] for $Sk_0/\varepsilon_0 = 3.4$, with $\overline{S}_{ij}$ given for $t \geq 0$ by

$$\overline{S}_{ij} = \begin{bmatrix} 0 & S/2 & 0 \\ S/2 & 0 & 0 \\ 0 & 0 & 0 \end{bmatrix}. \tag{5.10}$$

- *Plane strain:* Reference data are available from the direct numerical simulations (DNS) by Lee and Reynolds [59] for $Sk_0/\varepsilon_0 = 0.5$, with $\overline{S}_{ij}$ given for $t \geq 0$ by

$$\overline{S}_{ij} = \begin{bmatrix} S & 0 & 0 \\ 0 & -S & 0 \\ 0 & 0 & 0 \end{bmatrix}. \tag{5.11}$$

- *Axisymmetric expansion:* Reference data are available from the (DNS) by Lee and Reynolds [59] for $Sk_0/\varepsilon_0 = 5.59$, with $\overline{S}_{ij}$ given for $t \geq 0$ by

$$\overline{S}_{ij} = \begin{bmatrix} S & 0 & 0 \\ 0 & -S/2 & 0 \\ 0 & 0 & -S/2 \end{bmatrix}. \tag{5.12}$$

- *Axisymmetric contraction:* Reference data are available from the DNS by Lee and Reynolds [59] for $Sk_0/\varepsilon_0 = 0.41$, with $\overline{S}_{ij}$ given for $t \geq 0$ by

$$\overline{S}_{ij} = \begin{bmatrix} -S & 0 & 0 \\ 0 & S/2 & 0 \\ 0 & 0 & S/2 \end{bmatrix}. \tag{5.13}$$

5.3.2 Periodically Sheared turbulence

For initially isotropic turbulence subjected to time-periodic shear at $t = 0$, $\overline{S}_{ij}$ is given by

$$\overline{S}_{ij} = \frac{S}{2} \begin{bmatrix} 0 & \sin(\omega t) & 0 \\ \sin(\omega t) & 0 & 0 \\ 0 & 0 & 0 \end{bmatrix}, \tag{5.14}$$

where ω is the shearing frequency. For $Sk_0/\varepsilon_0 = 3.3$ and $\omega/S = 0.125, 0.25, 0.5, 0.75$ and 1.0, DNS results from Yu and Girimaji [127] can be used as reference data.

5.3.3 Decaying Anisotropic Turbulence

We consider arbitrary flow subjected to a constant applied strain $\overline{S}_{ij}$ for all $t < 0$, which is then impulsively removed at $t = 0$. Experimental results for decaying anisotropic turbulence have been obtained by Choi and Lumley [19] for initially plane-strained turbulence.

5.3.4 Straining, Relaxation, and Destraining

A more complex test of the nonequilibrium turbulence response to an imposed mean strain $\overline{S}_{ij}(t)$ is provided by experimental results of Chen et al. [16] for the straining, relaxation, and destraining of initially-isotropic homogeneous turbulence. This test effectively combines the impulsive straining cases in Section 5.3.1 and the decaying case in Section 5.3.3. In the experiment by Chen et al., $\overline{S}_{22}(t) = \overline{S}_{11}(t)$ and all other components of the imposed mean strain are zero.

5.4 Results

In the following, we demonstrate the application of the ABC method to determine parameters $\mathbf{c} = (C_1, C_2, C_{\epsilon 1}, C_{\epsilon 2})$ for the inverse problem in Eq. (5.9). The result of this model is the turbulence kinetic energy k for the test cases described in Section 5.3. The noise $\epsilon(\theta)$ in the model has a Gaussian prior distribution with a mean of 0 and a standard deviation equal to 0.0008. As summary statistics $\mathcal{S}'$, we use a set of values k_i of the kinetic energy k at the points t_i where the reference data are provided. The distance ρ is defined as the maximum error among the considered cases between the modeled kinetic energy and the reference data; namely

$$\rho(\mathcal{S}' - \mathcal{S}) = \max_{\text{cases}} \left(\max |\mathcal{S}' - \mathcal{S}| \right) . \tag{5.15}$$

The following results are obtained using Algorithm 4 outlined in Section 2.3. Since we do not have any prior information about the parameter values, the prior distribution $\pi(\mathbf{c})$ is taken to

be uniform. Therefore, for the calibration step, we used $n = 10^4$ uniformly distributed parameter samples to obtain an approximation of the distance distribution $P_n(\rho|\mathbf{c}, \mathcal{S}')$. We set the desired ratio of accepted parameters $x = 0.05$ to define the threshold d for further simulations and the initial covariance matrix cov_0 for the MCMC proposal $q(\mathbf{c}_0, \text{cov}_0)$.

In the MCMC component of Algorithm 4, we start 24 chains with initial parameters $\mathbf{c}_0$ randomly picked from the accepted parameters in the calibration step. These chains work using the defined threshold d and the adaptive proposal q until each of them accept 10^5 parameters. Thus, in our posterior distribution, we have 2.4×10^6 accepted parameters. To construct the joint pdf, we used a kernel density estimation technique with a Gaussian kernel and a bandwidth defined using Scott's rule [104].

5.4.1 Impulsively-Strained Turbulence

Figure 5.1 shows the posterior distribution for parameters $\mathbf{c}$ given the reference data for the four impulsively-strained turbulence cases. In order to facilitate visualization of the four dimensional posteriors for the four-parameter nonequilibrium closure model, marginal pdfs are shown on the diagonal subplots in Figure 5.1 for each of C_1, C_2, $C_{\epsilon 1}$, and $C_{\epsilon 2}$. Two dimensional marginalized joint pdfs are shown on the off-diagonal subplots of Figure 5.1. The maximum *a posteriori* (MAP) values of the unknown parameters, determined using reference data for the four impulsively-strained cases, are $\mathbf{c} = (C_1, C_2, C_{\epsilon 1}, C_{\epsilon 2}) = (1.4,\ 0.71,\ 1.854,\ 1.9125)$. Confidence intervals (90%) for these parameters are indicated by vertical blue dashed lines on Figure 5.1.

Using these parameter values, Figure 5.2 shows the evolution of the turbulence kinetic energy $k(t)/k_0$ for each of the initially isotropic impulsively-strained homogeneous turbulence cases, as well as for the periodically-sheared turbulence cases. The model performance with these parameters is shown by solid lines and reference values for each case are indicated by points. The results for the impulsively-strained homogeneous turbulence cases (Figure 5.2(a)) are in good agreement with the reference data, while the results for the periodically-sheared turbulence cases (Figure 5.2(b)) do not agree as closely with the reference data. This is expected, however, since, to construct the

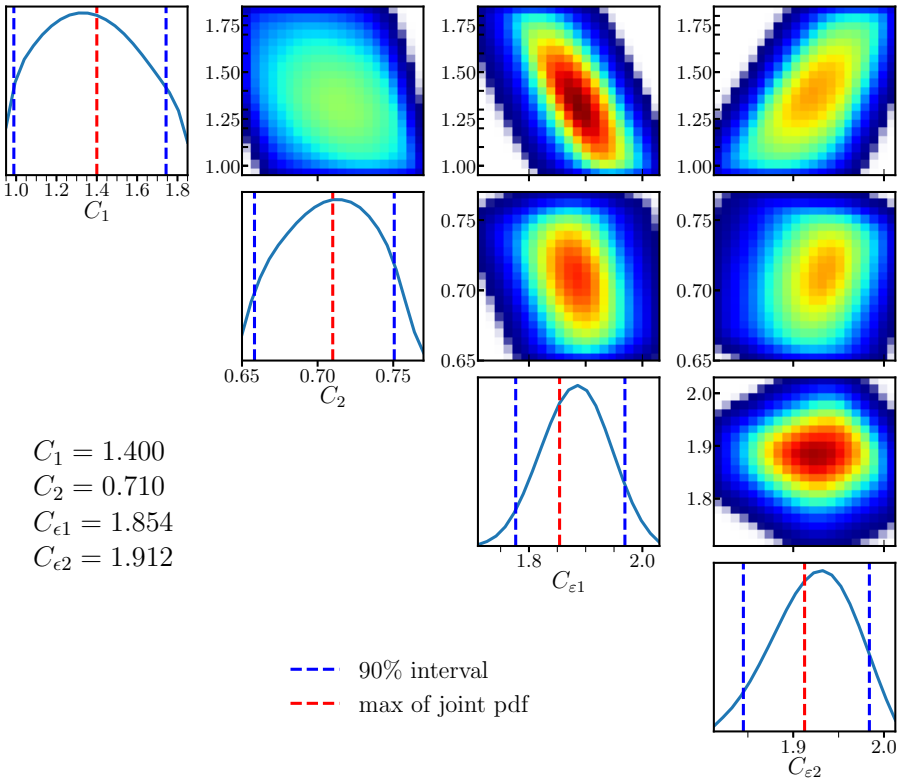

Figure 5.1: Marginal and joint probability density functions of accepted values of C_1, C_2, $C_{\epsilon 1}$ and $C_{\epsilon 2}$ for initially isotropic impulsively-strained homogeneous turbulence cases.

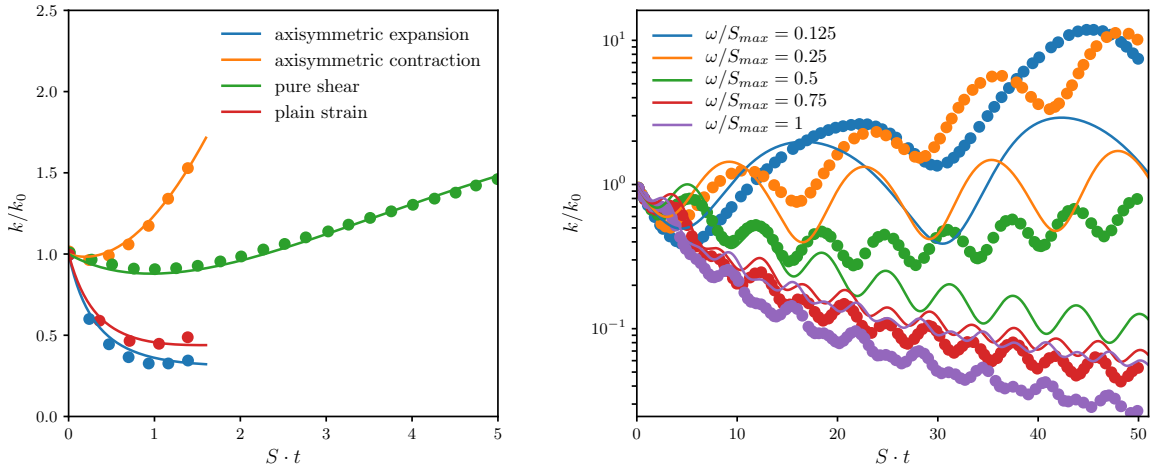

(a) Impulsively strained cases

(b) Periodically sheared cases

Figure 5.2: The evolution of turbulence kinetic energy $k(t)/k_0$ for the nonequilibrium model (solid lines) and reference data (points) for (a) the initially isotropic impulsively-strained homogeneous turbulence cases and (b) the periodically-sheared turbulence cases. Model parameters are determined using reference data from the impulsively-strained cases.

posterior distribution of unknown parameters, only impulsively-strained homogeneous turbulence cases were used.

5.4.2 Periodically-Sheared Turbulence

Similarly, we performed training of model parameters on the periodically-sheared turbulence cases described in Section 5.3 for five different shearing frequencies; namely, $\omega/S = 0.125$, 0.25, 0.5, 0.75 and 1.0. Figure 5.4 shows the resulting posterior pdfs and the corresponding MAP values are $\mathbf{c} = (C_1, C_2, C_{\epsilon 1}, C_{\epsilon 2}) = (2.3,\ 0.75,\ 2.050,\ 2.34)$. Once again, confidence intervals (90%) for these parameters are indicated by vertical blue dashed lines on Figure 5.4.

Figure 5.3(b) compares the model results for the five periodically-sheared cases. Compared to the results in Figure 5.2(b) for model parameters estimated using the impulsively-strained cases, Figure 5.3(b) shows that there is an improvement in the agreement for the low frequency cases. It should be noted that the amplitude of k is significantly different for low and high frequency cases, thus, defining the distance function ρ as the maximum difference between k values makes the algorithm focus on the lower frequency cases more, because of the higher amplitude of error as well. To avoid this issue, one could instead define the distance function as the maximum difference between $\log(k)$ values, which will be explored in the future.

Finally, model results for the four impulsively-strained turbulence cases are shown in Figure 5.3(a). The agreement with reference data is now worse than in Figure 5.2(a), because the model has been trained only on the periodically-sheared turbulence cases.

5.5 Regression

The local-linear regression described in Section 2.4 can be applied to the posterior distribution we get using the ABC-MCMC algorithm. In the following we provide an example of linear regression applied to the calibration of a nonequilibrium anisotropy closure model with three fixed parameters. We plan to extend it to a full four-parameter model application in the future.

5.5.1 1D Linear Regression

We reduce the problem to one parameter $\mathbf{c} = c$ (in the following examples we calibrate parameter C_1 in the nonequilibrium anisotropy closure) and the linear fit is then

$$f = \hat{\alpha} + (\mathcal{S}' - \mathcal{S})^T \hat{\beta}, \tag{5.16}$$

where $\mathcal{S} = (s_1, \ldots, s_q)$ is the vector of truth summary statistics.

If we perform linear regression on each component s_j of the summary statistic vector $\mathcal{S}$ independently, simplifying Eq. (5.16) to

$$f_j = \hat{\alpha}_j + (s'_j - s_j)^T \hat{\beta}_j, \quad j = 1, \ldots, q\,, \tag{5.17}$$

we notice that some s_j are not informative, i.e. the distance $d(s'_{ij}, s_j)$ does not have a clear linear trend of change with c_i, as shown in Fig. 5.5.

To measure how good the linear fit in Eq. (5.17) is, we can calculate the R^2 value (coefficient of determination) of the fit following the standard definition. The coefficient of determination is defined as

$$R^2 \equiv 1 - \frac{SS_{res}}{SS_{tot}}\,, \tag{5.18}$$

where SS_{tot} is the total sum of squares and SS_{res} is the sum of squares of residuals defined as

$$SS_{tot} = \sum_{i=1}^{m} (f_i - \overline{c})^2\,, \qquad SS_{res} = \sum_{i=1}^{m} (c_i - f_i)^2\,, \tag{5.19}$$

where $\overline{c}$ is the mean value of sampled parameters, c_i, and summation is performed over m sampled parameters.

We can see that R^2 can be very small, e.g. s_9 and s_{15} shown in Figure 5.5, and high, e.g. s_{30} and s_{24} shown in Fig. 5.6. Defining an informative statistic as a statistic with $R^2 > 0.85$, we show which components of the summary statistics vector for the impulsively-strained turbulence cases (Section 5.3.1) are informative statistics for the C_1 parameter with other parameters being fixed in the nonequilibrium anisotropy closure. Figure 5.8 shows the posterior distribution of parameter c_1. A wider posterior is observed without regression and a very narrow posterior with regression. This reduces the uncertainty of the parameter estimates.

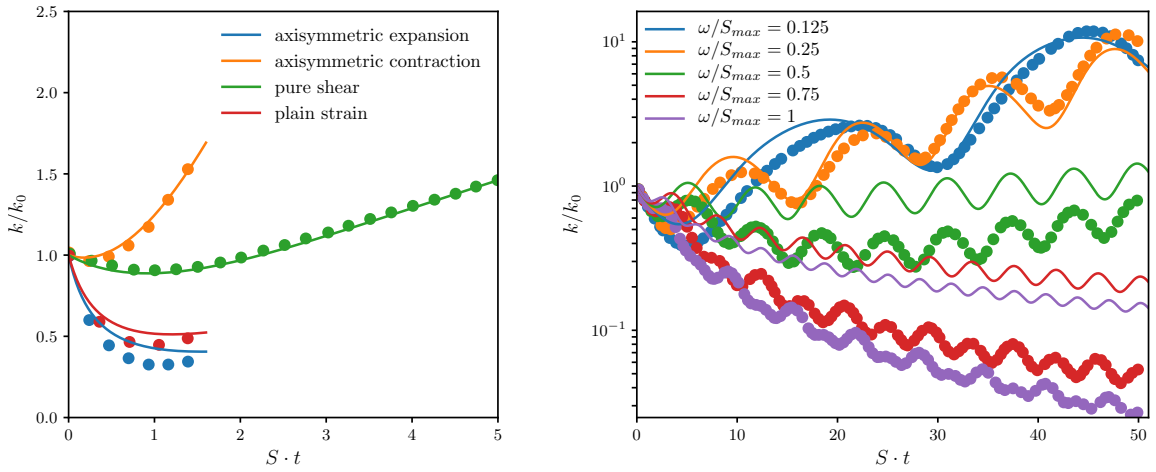

(a) Impulsively-strained cases

(b) Periodically-sheared cases

Figure 5.3: The evolution of turbulence kinetic energy $k(t)/k_0$ for the nonequilibrium model (solid lines) and reference data (points) for (a) the initially isotropic impulsively-strained homogeneous turbulence cases and (b) the periodically-sheared turbulence cases. Model parameters are determined using reference data from the periodically-sheared cases.

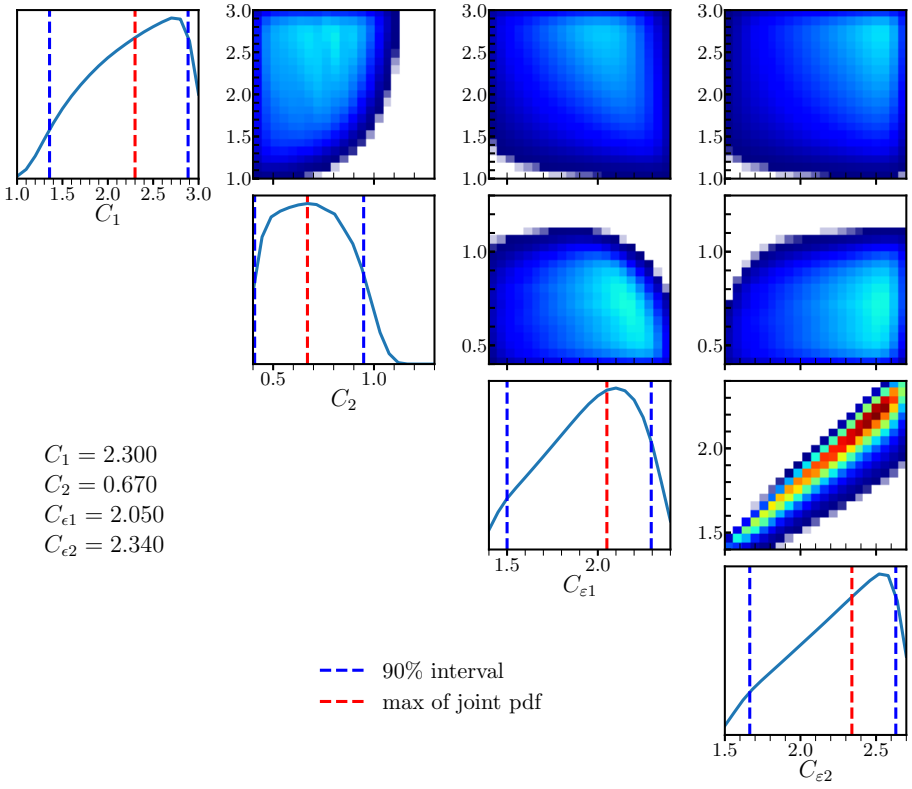

Figure 5.4: Marginal and joint probability density functions of accepted values of C_1, C_2, $C_{\epsilon 1}$ and $C_{\epsilon 2}$ for the periodically-sheared homogeneous turbulence cases.

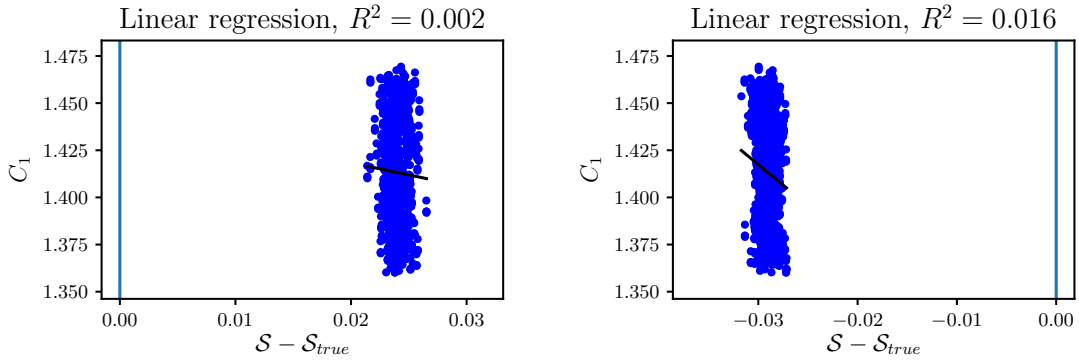

(a) s_9 (b) s_{15}

Figure 5.5: Example of noninformative statistics with the black line showing linear fit from Eq.(5.17).

5.6 Conclusions

In this study, model parameter values and uncertainties have been estimated for a nonequilibrium anisotropy closure model using approximate Bayesian computation (ABC) and a Markov chain Monte Carlo (MCMC) approach. The ABC-MCMC approach was applied to turbulent kinetic energy reference data for four different impulsively-strained cases, and for periodically-sheared turbulence with five different shearing frequencies. The estimated model parameters were found to be similar to, but not exactly the same as, previously reported values and gave good agreement between model results and the reference data. Ultimately, the ABC-MCMC approach demonstrated here is shown to be an effective and efficient method for estimating unknown model parameters as well as their uncertainties, in potentially complex turbulence closure models.

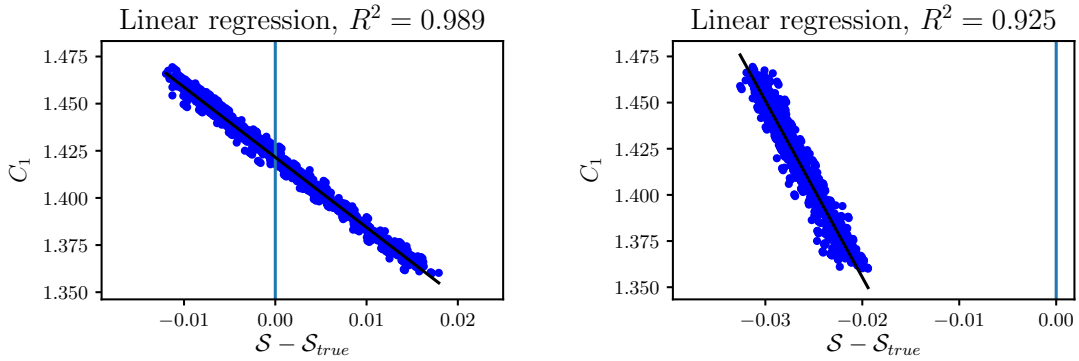

(a) s_{30} (b) s_{24}

Figure 5.6: Example of informative statistics statistics with the black line showing linear fit from Eq.(5.17).

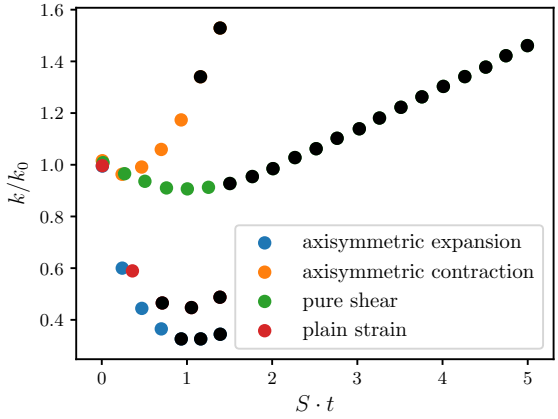

Figure 5.7: Informative statistics (black dots) and noninformative statistics (colored dots) for impulsively-strained turbulence cases (Section 5.3.1) and C_1 parameter (with other parameters being fixed) in nonequilibrium anisotropy closure.

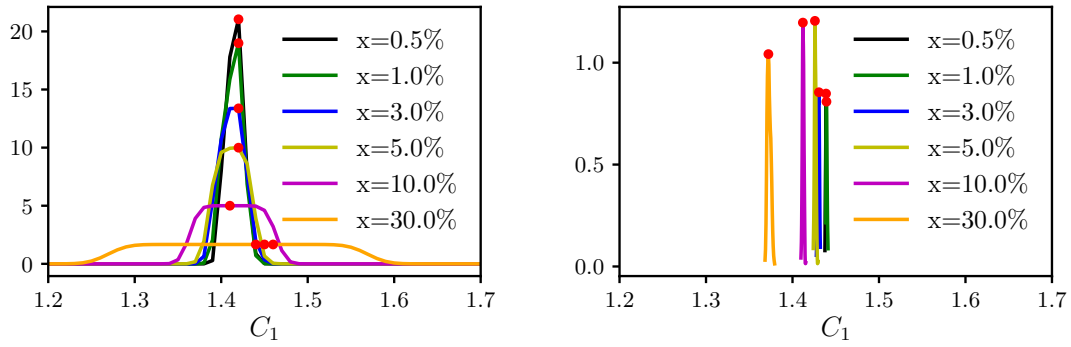

(a) Without regression (b) With regression

Figure 5.8: 1D posterior distributions.

Chapter 6

Menter Shear-Stress Transport Model Calibration Using ABC-MCMC

6.1 Introduction

Despite ongoing advances in the availability of high performance computing resources, the vast majority of industrial and engineering fluid flow problems are still simulated using Reynolds-averaged Navier Stokes (RANS) approaches. Although progress has been made in recent years on the development of computationally efficient large eddy simulation (LES) and hybrid RANS/LES approaches, RANS simulations are likely to remain common in engineering practice for many years to come, primarily because of their substantially lower computational cost compared to LES. Techniques such as optimization and uncertainty quantification are also becoming increasingly important components of the engineering design process, but such techniques often require thousands of simulations (or more), and RANS remains the only viable option for such large numbers of calculations.

The primary difficulty with RANS simulations is the requirement that a physically accurate, computationally stable model be provided for the unclosed Reynolds stresses that appear in the RANS equations. A wide variety of RANS closure models have been suggested over the years but, despite all efforts to create a robust and accurate model, no universal turbulence model exists. Moreover, essentially all RANS models rely on empirical coefficients that must be calibrated for different flows and geometries. Historically, these coefficients were defined by applying a model to a simplified turbulent flow with a known analytical solution, but such flows are often only distantly related to real-world practical applications.

The development of improved methods for inferring model parameters from available exper-

imental or higher fidelity data is an active area of research, with recent focus, in particular on backward inference or data-driven approaches [125]. Probabilistic approaches such as Bayesian methods can also be used to solve the inverse statistical problem that is the core of model parameter calibration, and such approaches are attractive because they provide not only model parameter values but also their uncertainties.

Cheung et al. [17] was the first to apply Bayesian inference method to calibrate Spalart-Allmaras turbulence model using velocity and skin friction experimental data. Oliver and Moser [83] extended this work by adding more models and stochastic extensions. Ray and co-authors [90, 60, 91, 93, 92] used a similar approach to calibrate RANS model parameters in a more complex turbulent flow, namely jet-in-crossflow. Zhang and Fu [128] combined the high-dimensional model representation technique and the Gaussian process machine learning method to construct a surrogate model to make Bayesian inference more affordable. As a demonstration of their method, they calibrated various parameters in the Menter shear stress transport (SST) model using surface drag measurements and velocity profiles from hypersonic turbulent flows over a flat plate as reference data.

In this study, we demonstrate the use of approximate Bayesian computation (ABC) for calibration of parameters in the Menter SST model. The ABC approach is attractive because it avoids the need to explicitly define or estimate a likelihood function, and can be combined with various acceleration techniques, such as Markov chain Monte Carlo (MCMC) methods and adaptive proposals for the Markov chains. The ABC-MCMC algorithm used here is identical to that described in Chapter 2 and used in Chapters 4 and 5. However, compared to Chapter 5, where the simplified cases of homogeneous flows are used to calibrate unknown parameters in nonequilibrium anisotropy RANS model, here we use a more complicated inhomogeneous flow; namely, an axisymmetric transonic bump with experimental results provided by by Bachalo and Johnson [1]. Recently, Schaefer et al. [101] and Zhao et al. [129] performed an uncertainty and sensitivity analysis of this model for different turbulent flows, and we perform a related calibration study prior to initiating Markov chains in order to determine which of the model parameters to

include in the estimation procedure.

In the following, we briefly describe the RANS Menter SST model in Section 6.2 and the axisymmetric transonic bump simulation case in Section 6.3. Then we provide a detailed description of the calibration step and choice of summary statistics for the ABC-MCMC algorithm. Model parameter estimation results are presented in Section 6.4, and conclusions and discussion are provided at the end. Ultimately, this study provides the most comprehensive and realistic demonstration of the ABC-MCMC turbulence model parameter estimation method that is the focus of this dissertation.

6.2 Description of Menter Shear-Stress Transport Two-Equation Model

The classical Menter SST model is a two-equation eddy-viscosity RANS model introduced by Menter [75] in 1994. It is based on the baseline model [75] (BSL model), which combines a Wilcox $k-\omega$ model [124] in the near-wall region and a standard $k-\epsilon$ model in the wake region of the boundary layer. This model blending was introduced to take advantage of a superior behavior of the $k-\omega$ model in the logarithmic part of the boundary layer in equilibrium adverse-pressure-gradient flows and compressible flows, and the freestream independence of the $k-\epsilon$ model in the outer part of the boundary layer. For convenient use, the $k-\epsilon$ model is transformed into the $k-\omega$ formulation, which differs from the original $k-\omega$ model by a cross-diffusion term in the ω equation, and also has different coefficients. Using the same transport equations, the Menter SST model incorporates Bradshaw's hypothesis that the principal turbulent shear-stress is proportional to the turbulent kinetic energy k.

In this study, we follow the nomenclature of NASA Langley Turbulence Modeling Resource (TMR),[1] and the complete formulation and explanation of the model can be found in [75]. The transport equations for k and ω are

$$\frac{\partial(\rho k)}{\partial t}+\frac{\partial(\rho u_j k)}{\partial x_j}=P-\beta^*\rho\omega k+\frac{\partial}{\partial x_j}\left[(\mu+\sigma_k\mu_t)\frac{\partial k}{\partial x_j}\right], \tag{6.1}$$

$$\frac{\partial(\rho\omega)}{\partial t}+\frac{\partial(\rho u_j\omega)}{\partial x_j}=\frac{\gamma}{\nu_t}P-\beta\rho\omega^2+\frac{\partial}{\partial x_j}\left[(\mu+\sigma_\omega\mu_t)\frac{\partial\omega}{\partial x_j}\right]+2(1-F_1)\rho\sigma_{\omega 2}\frac{1}{\omega}\frac{\partial k}{\partial x_j}\frac{\partial\omega}{\partial x_j}, \tag{6.2}$$

[1] https://turbmodels.larc.nasa.gov/sst.html

Table 6.1: Nominal values of Menter SST model coefficients.

Coefficient	σ_{k1}	σ_{k1}	$\sigma_{\omega1}$	$\sigma_{\omega2}$	β_1	β_2	β^*	κ	a_1
Nominal value	0.85	1.0	0.5	0.856	0.075	0.828	0.09	0.41	0.31

where u_i is the mean velocity, ρ is the density, $\nu_t = \mu_t/\rho$ is the turbulent kinematic viscosity and F_1 is the blending function, such that $F_1 = 1$ in the near-wall region, activating the original $k-\omega$ model, and $F_1 = 0$ away from the surface, activating the transformed $k-\epsilon$ model. The F_1 function is defined as

$$\begin{aligned} F_1 = \tanh(\arg_1^4), \qquad \arg_1 &= \min\left[\max\left(\frac{\sqrt{k}}{\beta^*\omega d}, \frac{500\nu}{d^2\omega}\right), \frac{4\rho\sigma_{\omega2}k}{CD_{k\omega}d^2}\right], \\ CD_{k\omega} &= \max\left(2\rho\sigma_{\omega2}\frac{1}{\omega}\frac{\partial k}{\partial x_j}\frac{\partial \omega}{\partial x_j}, 10^{-20}\right), \end{aligned} \tag{6.3}$$

where d is the distance from the wall and $\arg_1$ goes to zero far enough from walls because of the d or d^2 factors in the denominators of all three terms. Thus, the cross-diffusion term with $(1-F_1)$ in Eq. (6.2) disappears near the wall.

The coefficients $\phi = (\gamma, \beta, \sigma_k, \sigma_\omega)$ are different for each part of the blended model, with ϕ_1 denoting values for the $k-\omega$ model and ϕ_2 for the $k-\epsilon$ model. The combined model in Eqs. (6.1) and (6.2) thus uses a single ϕ defined as

$$\phi = F_1\phi_1 + (1-F_1)\phi_2\,. \tag{6.4}$$

Closure coefficients and their nominal values are provided in Table 6.1.

Other closure coefficients are defined using the values in Table 6.1 as

$$\gamma_1 = \frac{\beta_1}{\beta^*} - \sigma_{\omega1}\frac{\kappa^2}{\sqrt{\beta^*}}\,, \qquad \gamma_2 = \frac{\beta_2}{\beta^*} - \sigma_{\omega2}\frac{\kappa^2}{\sqrt{\beta^*}}\,. \tag{6.5}$$

The turbulence kinetic energy production P in Eqs. (6.1) and (6.2) is defined as

$$P = \tau_{ij}\frac{\partial u_i}{\partial x_j}\,, \quad \text{where} \quad \tau_{ij} = \mu_t\left(\frac{\partial u_i}{\partial x_j} + \frac{\partial u_j}{\partial x_i} - \frac{2}{3}\frac{\partial u_k}{\partial x_k}\delta_{ij}\right) - \frac{2}{3}\rho k\delta_{ij}\,. \tag{6.6}$$

In the $k-\epsilon$ and $k-\omega$ two-equation models, the principal shear-stress $\tau := -\rho\overline{u'v'}$ is usually computed as $\tau = \mu_t(\partial u/\partial y)$. However, based on Bradshaw's assumption, the shear stress in the

boundary layer is proportional to the turbulent kinetic energy k as $\tau = \rho a_1 k$, with a_1 being constant. Taking this into account, Menter [75] defined the turbulent eddy viscosity as

$$\mu_t = \frac{\rho a_1 k}{\max(a_1\omega, \Omega F_2)}\,, \tag{6.7}$$

where $\Omega = \sqrt{2R_{ij}R_{ij}}$ with $R_{ij} = 1/2\,(\partial u_i/\partial x_j - \partial u_j/\partial x_i)$ is the absolute vorticity and F_2 is the second blending function

$$F_2 = \tanh(\arg_1^2)\,, \quad \arg_2 = \max\left(\frac{\sqrt{k}}{\beta^*\omega d}, \frac{500\nu}{d^2\omega}\right)\,. \tag{6.8}$$

In an adverse-pressure-gradient boundary layer, production of k is larger than its dissipation ($\Omega > a_1\omega$) and the second term in the parenthesis of Eq. (6.7) becomes dominant over the first term, which is the conventional eddy-viscosity formulation $\mu_t = \rho k/\omega$ in a $k-\omega$ model.

6.3 Flow Solver and Test Problem

To calibrate Menter SST model coefficients, we use the axisymmetric transonic bump case with reference data obtained from the experimental results provided by Bachalo and Johnson [1]. This is a widely used test case for shock-induced separated flow, followed by reattachment. The axisymmetric bump in this experiment is a circular-arc bump with a height of 1.905 cm and a length of 20.32 cm attached to a cylinder that is 15.24 cm in diameter. The flow has a freestream Mach number $M = 0.875$, a temperature of $T = 540°$R and a combination of shock and trailing-edge adverse-pressure-gradient causes flow separation with reattachment downstream of the bump (creating a separation bubble). The Reynolds number $Re = 2.763 \times 10^6$ is calculated based on the freestream velocity U_{inf} and the bump length c. All of the computational case parameters are provided by the TMR website[2] and Figure 6.1(a) shows a schematic of the experiment.

All flow solutions in this chapter were obtained using the modified NASA `OVERFLOW` code version 2.2n[3] . `OVERFLOW` is a compressible 3D flow solver that solves the time-dependent RANS equations using multiple overset structured grids. The code can also operate in two-dimensional or

[2] https://turbmodels.larc.nasa.gov/axibump_val.html
[3] https://overflow.larc.nasa.gov/

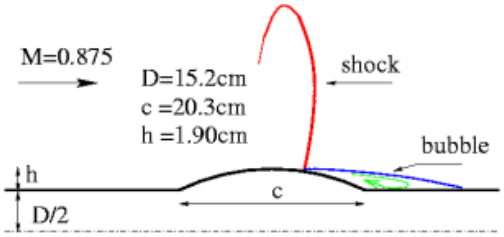

(a) Axisymmetric bump experiment schematic.

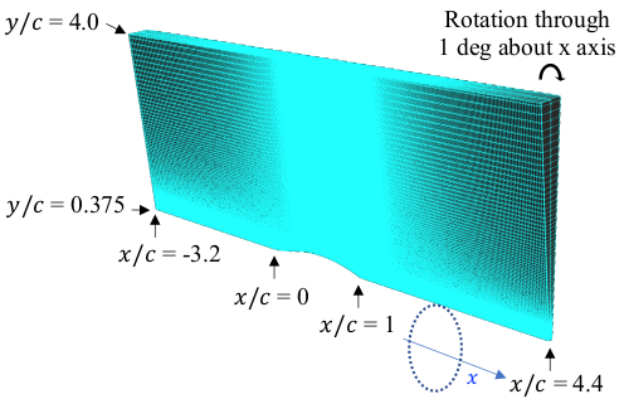

(b) Axisymmetric transonic bump geometry

Figure 6.1: Axisymmetric transonic bump geometry and experiment schematic.

axisymmetric mode. It has been broadly verified and validated [18, 55] and is widely used across the aerospace industry. The modifications allow the code to read turbulence model coefficients from the parameters file in order to perform the ABC-MCMC algorithm.

For axisymmetric problems, `OVERFLOW`can be configured in an axisymmetric mode with a three-plane grid. The center plane lies on the x, z plane and the other two planes lie at $\pm 1^\circ$ rotations from this plane. The geometry and grid configuration are shown in Figure 6.1(b), taken from the TMR website. All computational solutions were obtained using a computational grid with 721×321 cells on the center plane provided by the TMR website. Each simulation ran for 5000 time steps, requiring ~ 1.5 CPU hours using 16 processors.

This axisymmetric transonic bump case has been used previously for Menter SST model validation in `OVERFLOW` [55] and is thus ideally suited for the calibration of the SST model parameters in the present work. Uncertainty quantification for the Menter SST model coefficients [101] has also been performed for this case using the same computational grid as that used here.

Experimental data for these profiles and `OVERFLOW` result for the Menter SST model with nominal coefficients from Table 6.1 are provided in Figs. 6.2 and 6.3.

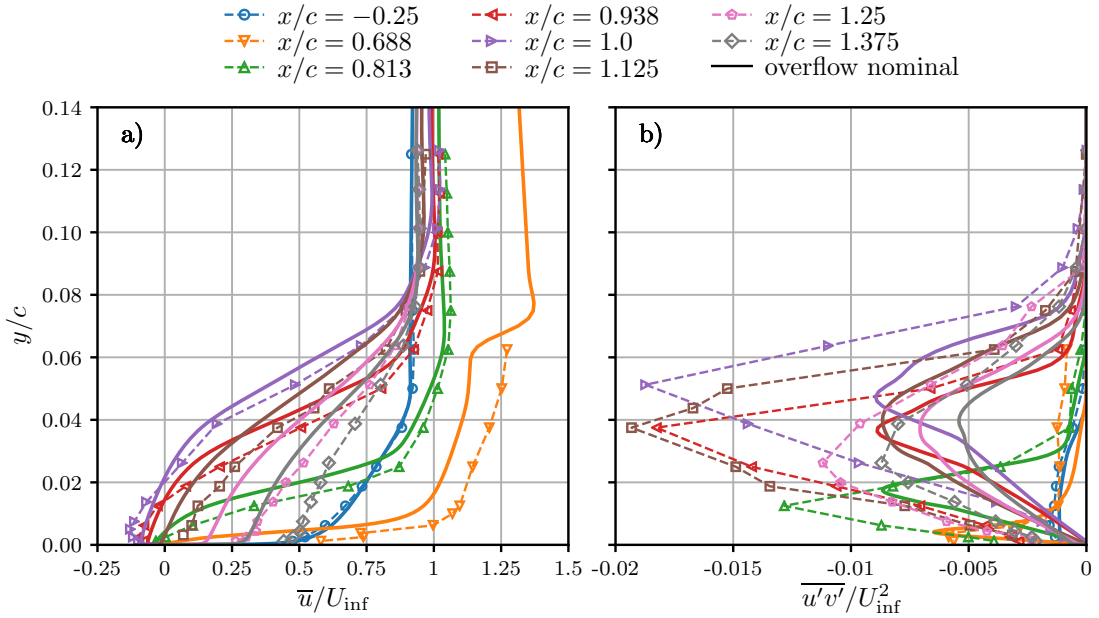

Figure 6.2: Experimental data and numerical result for the Menter SST model with nominal coefficients from Table 6.1 of a) mean velocity and b) turbulent shear stress.

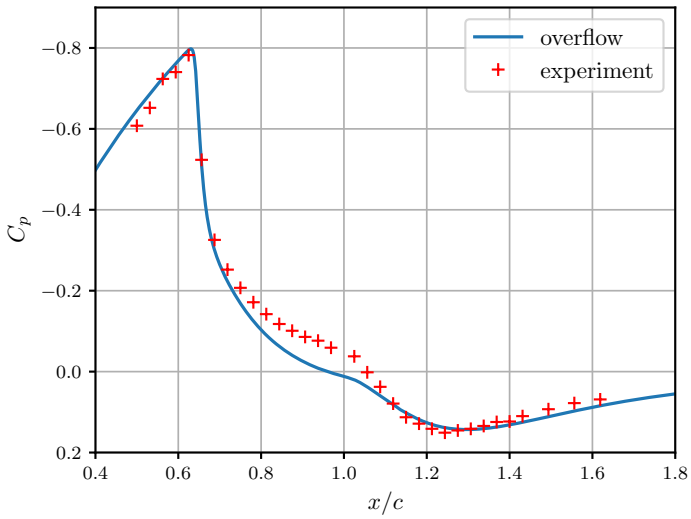

Figure 6.3: Experimental data and numerical result for the Menter SST model with nominal coefficients from Table 6.1 of pressure coefficient C_p.

6.4 Parameter Estimation Results

The ABC-MCMC algorithm with an adaptive proposal used in this study is identical to that described and used in previous chapters of this dissertation. Consequently, we do not re-state the details of the approach. In the following, we provide extensive detail on the calibration step and selection of summary statistics prior to initiating Markov chains; it will be seen that this initial step allows us to reduce the number of unknown parameters calibrated in the model, thereby substantially reducing the computational cost. Final parameter estimates from the ABC-MCMC approach and comparisons with experimental data are provided at the end of this section.

6.4.1 Calibration Step and Choice of Summary Statistics

Schaefer et al. [101] in their uncertainty quantification study of the Menter SST model coefficients demonstrated that five parameters $(\beta^*, \sigma_{\omega 1}, \beta^*/\beta_1, \beta^*/\beta_2, a_1)$ make the most significant contribution to axisymmetric transonic bump simulation results. Based on this analysis, we chose the parameters $\beta^*, \sigma_{\omega 1}, \beta_1, \beta_2, a_1$ for ABC-MCMC calibration. In this calibration step we uniformly sampled $n = 7,776$ parameters samples (uniform grid with 6 samples per dimension).

The advantage of the relatively simple rejection ABC method used in the calibration step is that sampling does not depend on the acceptance criteria. Thus, for each sampled parameter we can store the model output and measure the distance between truth and modeled summary statistics after all simulations have been performed. This allows us to build posterior distributions for various summary statistics and threshold values, and to choose the best statistics and thresholds for the parameter estimation using Markov chains.

For the axisymmetric transonic bump case, we consider experimental data provided by Bachalo and Johnson [1] and shown in Figures 6.2 and 6.3 to be the reference data. Thus, the available reference data are comprised of the pressure coefficient C_p, mean velocity $\overline{u}/U_{\text{inf}}$, turbulent shear stress profiles $(\overline{u'v'})/U_{\text{inf}}^2$, and separation and reattachment points. The experiment provides eight mean velocity and turbulent shear stresses profiles at $x/c = -0.25, 0.688, 0.813, 0.938, 1.0, 1.125, 1.25, 1.375$.

This reference data can be considered as true summary statistics $\mathcal{S}$.

Correspondingly, as modeled summary statistics, $\mathcal{S}'$, we considered pressure coefficient data, mean velocity data, and shear stresses data, interpolated at points where the reference data are provided. Turbulent shear stresses were calculated during post-processing as

$$\overline{u'v'} = -\frac{\mu_t}{\rho}\left(\frac{\partial u}{\partial y} + \frac{\partial v}{\partial x}\right), \tag{6.9}$$

where the turbulent eddy viscosity, μ_t, was taken from SST model calculation.

We define the distance function simply as 2-norm of difference between true summary statistics $\mathcal{S}$ and modeled summary statistics $\mathcal{S}'$, that is

$$d(\mathcal{S}', \mathcal{S}) = \left[\sum_i \left(\mathcal{S}'_i - \mathcal{S}_i\right)^2\right]^{1/2}, \tag{6.10}$$

where i span over data points where the reference data are provided.

Figure 6.4(a)-(c) shows marginal posteriors from the ABC rejection algorithm for $\beta^*, \sigma_{w1}, \beta_1, \beta_2$ and a_1 using the three different summary statistics (i.e., pressure coefficient, mean velocity and turbulent shear stresses profiles). This figure shows that the marginal posteriors for β_2 and a_1 have completely different maximum *a posterior* probability (MAP) values depending on whether C_p or the shear stress are used in the ABC approach. This indicates that the SST model may not be able to simultaneously predict C_p and shear stresses with a high degree of precision using the same parameter values.

To combine available reference data, we normalize it by maximum and number of data points of each reference data. The distance function thus becomes

$$d(\mathcal{S}', \mathcal{S}) = \left[\sum_k \frac{1}{N_k} \sum_i \left(\frac{\mathcal{S}'^k_i - \mathcal{S}^k_i}{\max_i \mathcal{S}^k_i}\right)^2\right]^{1/2}, \tag{6.11}$$

with the separation and reattachment error defined as

$$err_{sep} = \left[(x'_{sep} - x_{sep})^2 + (x'_{reattach} - x_{reattach})^2\right]^{1/2}. \tag{6.12}$$

Figure 6.4(d)-(e) shows marginal posterior distribution after combining the available reference data, in particular: (d) combination of pressure coefficient and mean velocity profiles data, (e)

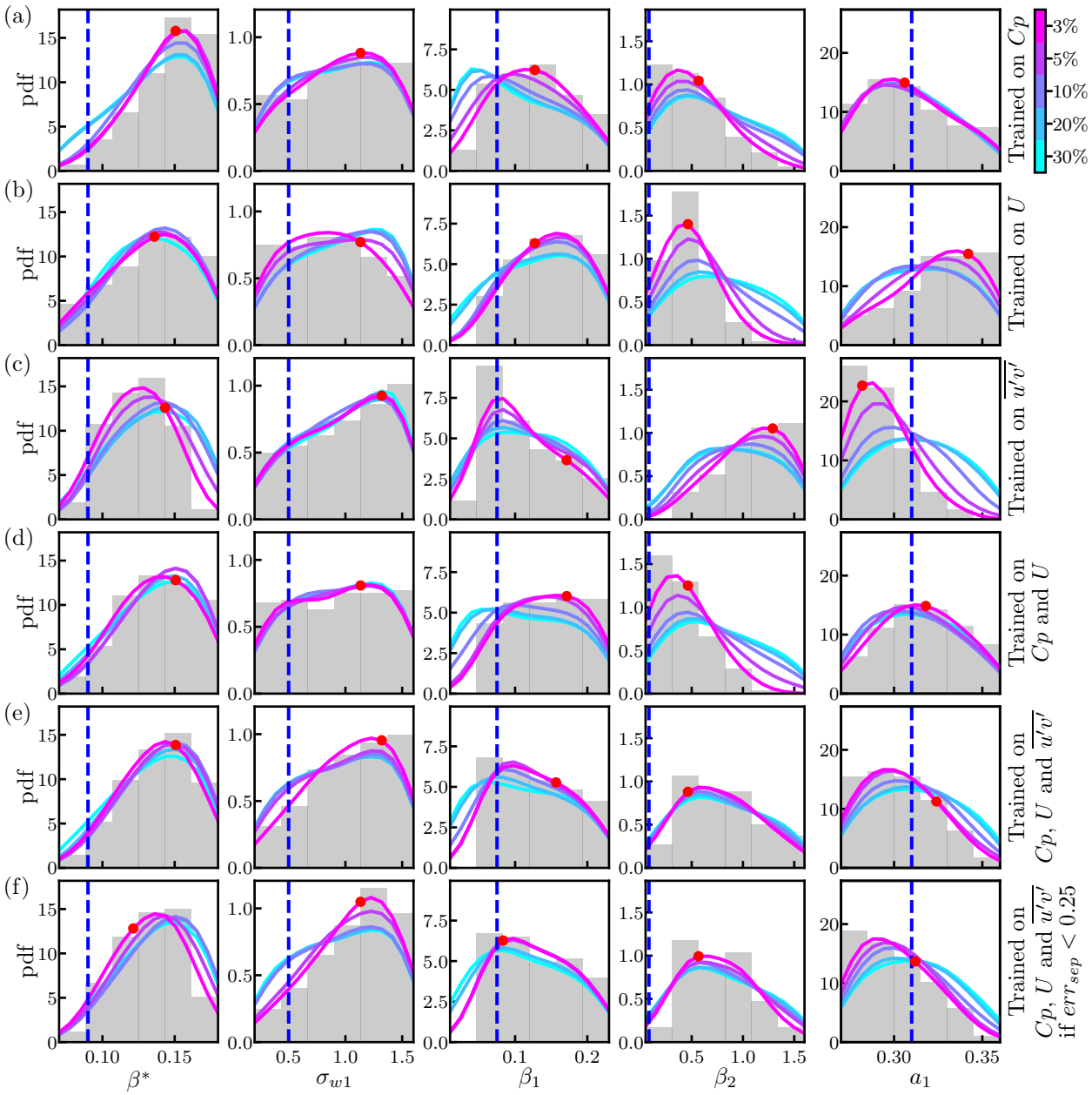

Figure 6.4: Marginal posteriors for calibration step with $\beta^*, \sigma_{\omega 1}, \beta_1, \beta_2, a_1$ parameters and 7776 samples. Each row shows a posterior for different summary statistics: (a) pressure coefficient, (b) mean velocity, (c) turbulent shear stresses profiles, (d) combination of pressure coefficient and mean velocity profiles data, (e) combination of pressure coefficient, mean velocity profiles, and turbulent shear stress profiles data, and (f) combination of pressure coefficient, mean velocity profiles, and turbulent shear stress profiles data with condition on separation and reattachment error to be less than 0.25. Line colors correspond to the percentage of accepted simulations, as determined by the rejection threshold ε. Raw marginals for a 3% acceptance rate (i.e., before Gaussian kernel density estimation) are shown by gray bars. Red dots show the most probable parameter values from the full 5D posteriors for a 3% acceptance rate. Vertical blue dashed lines show the nominal parameter values listed in Table 6.1.

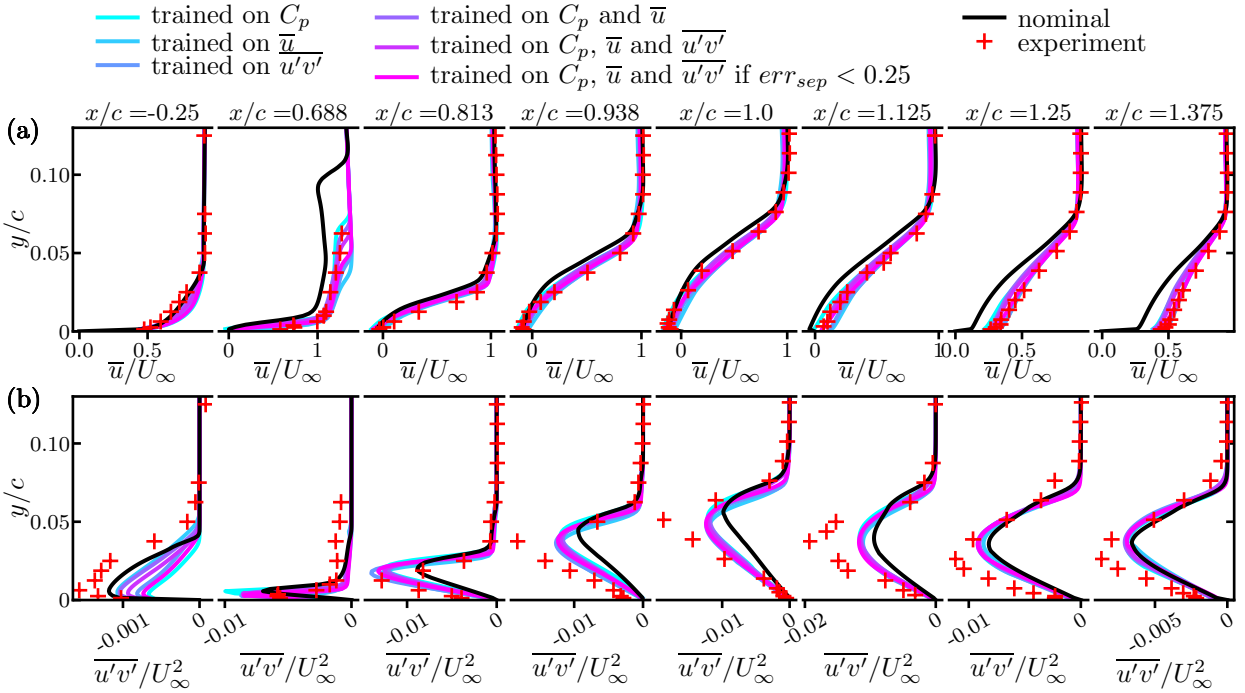

Figure 6.5: Experimental data and numerical result of (a) mean velocity and (b) turbulent shear stress for the Menter SST model with nominal coefficients from Table 6.1 and maximum values of the posterior shown in Figure 6.4.

combination of pressure coefficient, mean velocity profiles, and turbulent shear stress profiles, and (f) the same as (e), but with the condition that the separation and reattachment error be less than 0.25. These figures show that the resulting marginals have maxima that are mixtures of the maxima from the marginals of each of the summary statistics individually.

To compare results for different summary statistics, we estimated MAP values of joint probability distributions with 3% accepted parameters (shown with red dots in Figure 6.4) for all six summary statistics presented in Figure 6.4 and ran forward simulations with these parameters. Figure 6.5 shows the corresponding velocity and turbulent shear stress profiles and Figure 6.6 shows the resulting pressure coefficient profile. The model with MAP values recovers experimental results in velocity and shear stress profiles noticeably better than the model with nominal values from Table 6.1.

Based on this comparison, we pick the combination of pressure coefficient, mean velocity

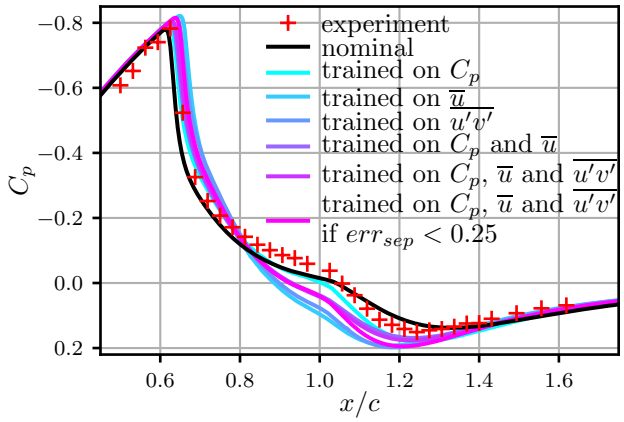

Figure 6.6: Experimental data and numerical result of pressure coefficient C_p for the Menter SST model with nominal coefficients from Table 6.1 and maximum values of the posterior shown in Figure 6.4

profiles, and turbulent shear stress profiles data with condition on separation and reattachment error to be the summary statistics for all following results.

It should be noted that we noticed a strong linear correlation between β^* and β_1 and switched to calibration of parameters $\beta^*, \sigma_{\omega 1}, \beta_1/\beta^*, \beta_2/\beta^*, a_1$ instead. This calibration had $n = 28,804$ samples (i.e., a uniform grid with 6, 13, 6, 7, 8 samples per parameter correspondingly). Figure 6.7 shows the marginal distributions for this calibration. The bigger number of samples in $\sigma_{\omega 1}$ was chosen to demonstrate that the marginal distribution of this parameter is close to uniform. Thus, to reduce the amount of computation, we removed $\sigma_{\omega 1}$ from calibrated parameters and set its value to the nominal value $\sigma_{\omega 1} = 0.5$.

The last calibration step for four parameters $\beta^*, \beta_1/\beta^*, \beta_2/\beta^*, a_1$ had 20,736 samples (i.e., uniform grid with 12 samples per dimension). Figure 6.8 shows marginal distributions for this calibration. Using this posterior distribution we can define necessary characteristics for the MCMC aspect of the ABC-MCMC algorithm. We set the threshold ε such that $P(d(\mathcal{S}', \mathcal{S}) \leq \varepsilon) = 0.03$ (i.e., maximum distance value of 3% accepted parameters), defined the standard deviation of the initial Gaussian kernel for the chains as 0.25 of the standard deviation of the posterior formed by accepting 3% of the tested parameters. The starting parameter values for the chains were randomly sampled from these posteriors.

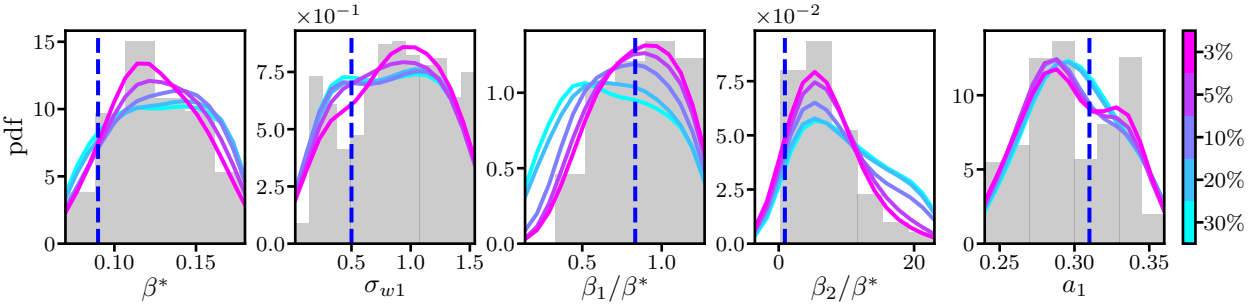

Figure 6.7: Marginal posteriors for calibration step with $\beta^*, \sigma_{\omega 1}, \beta_1/\beta^*, \beta_2/\beta^*, a_1$ parameters and 28804 samples.Line colors correspond to the percentage of accepted simulations, as determined by the rejection threshold ε. Raw marginals for a 3% acceptance rate (i.e., before Gaussian kernel density estimation) are shown by gray bars. Vertical blue dashed lines show the nominal parameter values listed in Table 6.1.

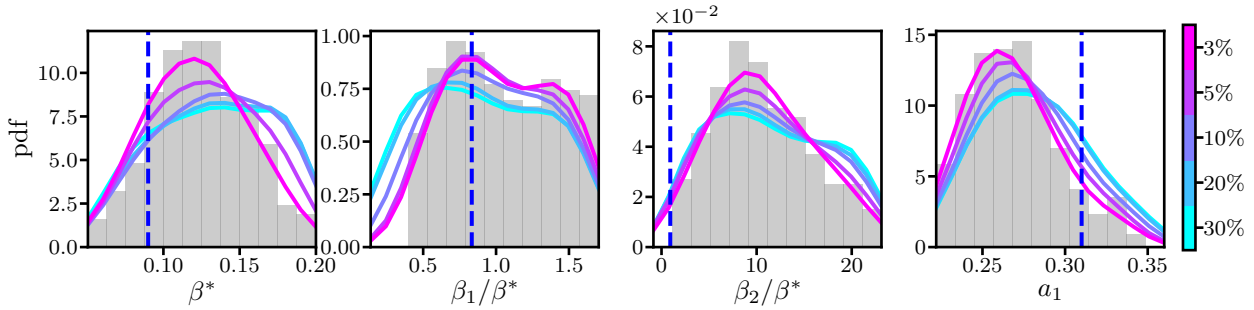

Figure 6.8: Marginal posteriors for calibration step with $\beta^*, \beta_1/\beta^*, \beta_2/\beta^*, a_1$ and 20736 samples. Line colors correspond to the percentage of accepted simulations, as determined by the rejection threshold ε. Raw marginals for a 3% acceptance rate (i.e., before Gaussian kernel density estimation) are shown by gray bars. Vertical blue dashed lines show the nominal parameter values listed in Table 6.1.

6.4.2 Results from ABC-MCMC Parameter Esimation

We ran 200 independent Markov chains, each starting from different parameter values randomly sampled from the accepted parameters (with 3% acceptance rate) in the calibration step. For an initial period of $k = 100$ chain steps, the chain kernel ran without kernel adaptation. The total number of accepted parameters in the chains is 116,327. Figure 6.9 shows marginal (diagonal subplots), 2D marginalized (overdiagonal subplots) and 2D conditional (below diagonal) posterior pdfs. The estimated parameters are MAP values of the joint posterior distribution shown in Figure 6.9, with red dashed lines and their values listed in Table 6.2.

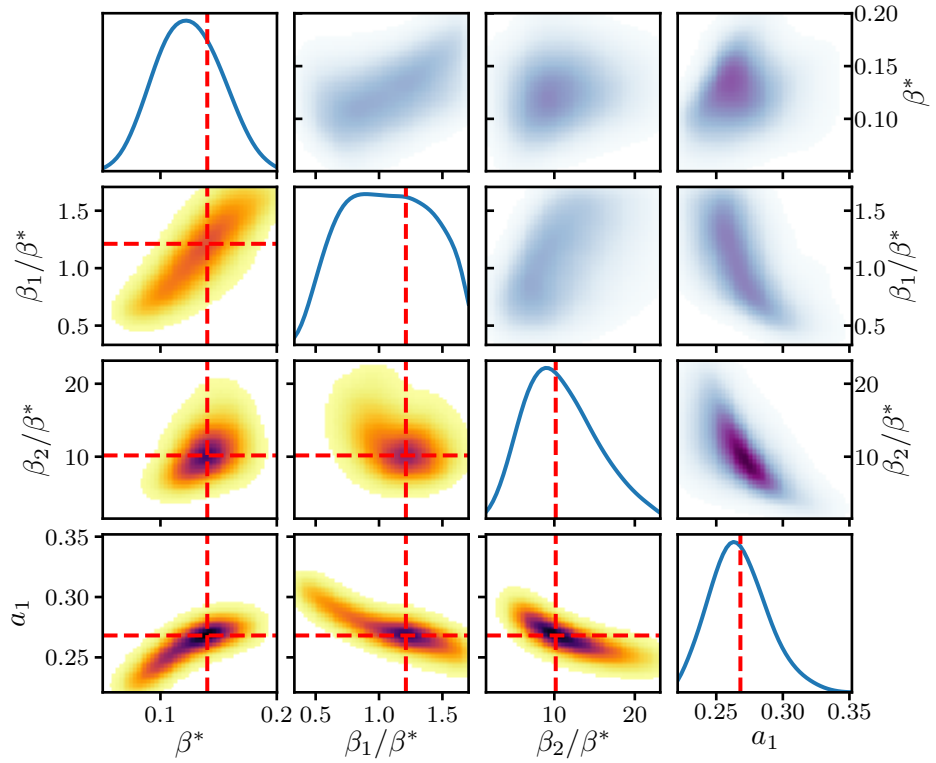

Figure 6.9: Two-dimensional marginalized joint posteriors. Diagonal subplots show one-dimensional marginal pdfs, upper-diagonal subplots show two-dimensional marginalized pdfs and under-diagonal subplots show conditional pdfs taken at MAP values. Red dashed lines represent the MAP values of 4D posterior.

Table 6.2: Estimated parameters for SST model.

Coefficient	β^*	β_1/β^*	β_2/β^*	a_1
Nominal value	0.09	0.833	0.92	0.31
Estimated values	0.14	1.212	10.17	0.268

The comparison of mean velocities and turbulent shear stress profiles of the numerical simulation with estimated parameters and nominal parameters and experimental data is shown in Figure 6.10. Once we obtained the posterior distribution of model parameters we can propagate their uncertainty through the model to estimate uncertainty intervals on the output quantity of interest. To do that we use Monte Carlo Sampling algorithm. Given the probability distribution of model parameters, we draw 199 samples from this distribution and evaluate the model to obtain the modeled quantity of interest. Then we estimate the distribution of the propagated samples. The

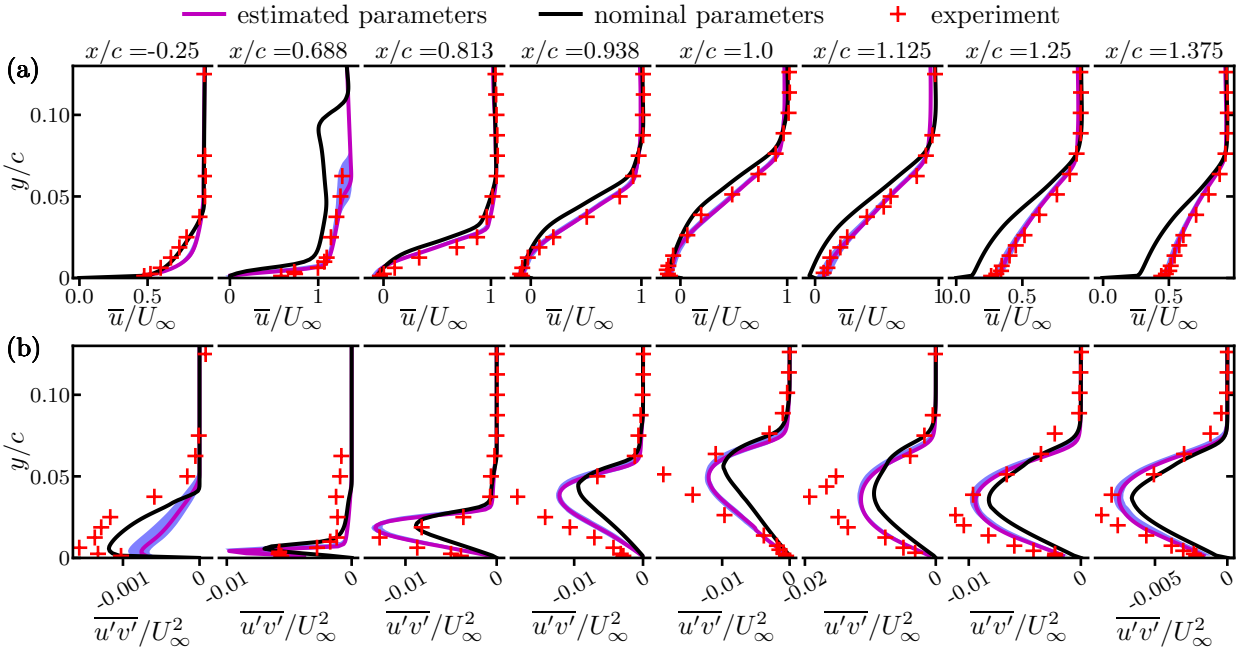

Figure 6.10: Experimental data and numerical result of (a) mean velocity and (b) turbulent shear stress for the Menter SST model with nominal coefficients from Table 6.1 and maximum values of the posterior shown in Figure 6.4. The shaded area indicates the 75% confidence interval

shaded area in Figures 6.10 and 6.11 indicates the 75% confidence interval for each distribution.

Ultimately, the final parameter values from the ABC-MCMC procedure shown in Table 6.2 are substantially different than the nominal values. This correspond to a substantial overall improvement in the ability of the SST model to predict experimental velocity and shear stress profiles, as shown in Figure 6.10, at the expense of slightly reduced agreement with the experimental measurements of C_p. However, the flexibility of the ABC-MCMC method allows a user to easily adjust the weighting of different terms in the combined distance function such that improved agreement of C_p, or improvements in only a certain region of the flow (e.g., prior to flow separation), can be prioritized.

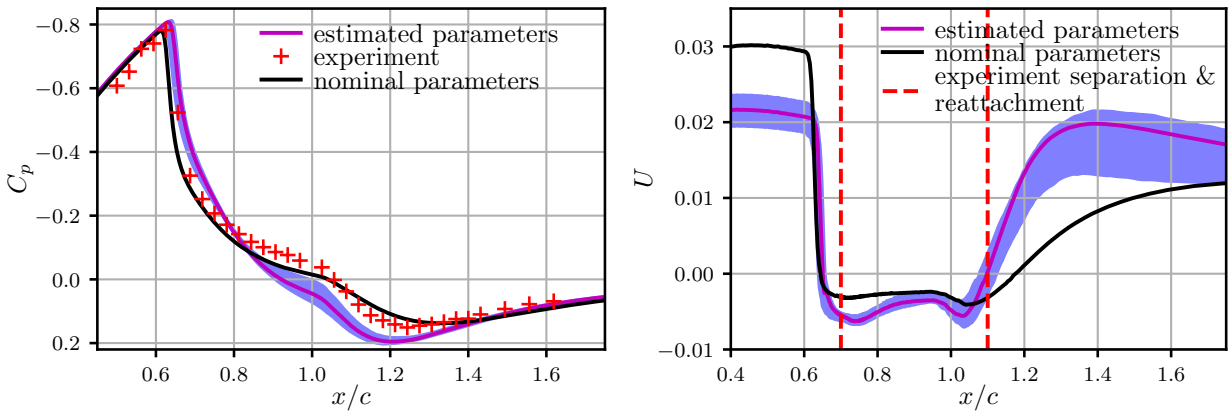

(a) Pressure coefficient C_p

(b) Mean velocity along the surface

Figure 6.11: Experimental data and numerical result of pressure coefficient and mean velocity profile for the Menter SST model with nominal coefficients from Table 6.1 and maximum values of the posterior shown in Figure 6.4. The shaded area indicates the 75% confidence interval

6.5 Conclusions

In the present study, we demonstrate the use of the approximate Bayesian computation with Markov chain Monte Carlo (ABC-MCMC) algorithm for calibration of the RANS Menter SST model parameters. We use a complicated inhomogeneous flow, namely, an axisymmetric transonic bump, with experimental results provided by Bachalo and Johnson [1], as reference data and the RANS of the axisymmetric transonic bump as a model in the ABC-MCMC algorithm.

We provide a detailed description of the calibration step for ABC-MCMC and the choice of summary statistics. The ABC rejection algorithm, used in the calibration step, has a noticeable advantage. It provides us with an opportunity to compare different summary statistics and distance functions. This comparison revealed that the model with the same set of parameters is unable to match all reference data fields. In our calibration step, ABC provides different estimated parameters for different summary statistics constructed from available reference data.

After combining available reference data with equal weights and condition on separation and reattachment points error into summary statistics used in the ABC-MCMC algorithm, the estimated model parameters gave good agreement between model results and the reference data.

Once we obtained the posterior distribution of model parameters, we propagate their uncertainty through the model to estimate uncertainty intervals on the output quantity of interest.

Ultimately, the ABC-MCMC approach demonstrated here is shown to be an effective and efficient method for estimating unknown model parameters, as well as their uncertainties, in potentially complex turbulence closure models.

Chapter 7

Conclusions and Future Research

This dissertation demonstrates the estimation of turbulence model parameters using approximate Bayesian computation (ABC). Many recent studies of model parameter estimation and uncertainty quantification focus on statistical approaches. For example, Bayesian inference can be used to provide posterior distributions of unknown parameters, but knowledge of the likelihood function is required, which can be expensive to compute. By contrast, ABC uses a series of approximations to estimate the posterior without knowing or estimating the likelihood function. Applying ABC to turbulence model parameter estimation reduces the computational burden of Bayesian inference and provides a flexible tool for model calibration.

In this dissertation, we described the ABC methodology in detail, including the baseline algorithm, a Markov chain Monte Carlo (MCMC) technique, calibration step, adaptive proposal, and a linear regression correction. To demonstrate how ABC can be applied to turbulence model calibration, we estimated model parameters for three different turbulence models. In the following, we provide additional more specific conclusions resulting from the research described in this dissertation, and also provide several directions for future research.

7.1 Conclusions

As a result of the research described herein, we can state the following conclusions:

(1) The ABC-MCMC approach is shown to be an effective and efficient method for estimating unknown model parameters, as well as their uncertainties.

(2) ABC-MCMC can be applied to potentially complex turbulence closure models, such as models with partial differential equations.

(3) The MCMC procedure and adaptive proposal accelerate the ABC process and reduce the requirement for computational resources during the model parameter estimation.

(4) The summary statistics are a crucial component of ABC. These statistics must be sufficiently sensitive to changes in model parameters and must represent the dependence of the underlying reference data on these parameters.

(5) The acceptance-rejection ABC algorithm, despite its computational expensiveness, has a noticeable advantage. Since parameter samples in this algorithm are independent of each other, we can store the output from the simulations with each sampled parameter and experiment with different choices of the summary, distance function metric, and tolerance, to see how this affects our results. Thus, the calibration step in ABC-MCMC algorithm can provide not only hyper-parameters for the chains, but also design the best summary statistics and distance function.

(6) All of the estimation studies of turbulence model parameters in this dissertation demonstrate that models are often unable to simultaneously match all reference data fields, and ABC provides different estimated parameters for different summary statistics constructed from available reference data. As such, ABC provides an additional understanding of the model behavior and its ability to reconstruct the real turbulence flow.

(7) Once we obtained the posterior distribution of model parameters we can propagate their uncertainty through the model to estimate uncertainty intervals on the output quantity of interest. To do that, we use Monte Carlo Sampling algorithm. Given the probability distribution of model parameters, we draw samples from this distribution and evaluate the model to obtain the modeled quantity of interest and estimate the distribution of the propagated samples.

7.2 Future Research

The research described in this dissertation suggests a number of important directions for future research, including:

(1) The efficiency of the ABC-MCMC algorithm can be further improved by incorporating an adaptive threshold ε into the MCMC procedure, as recently proposed by Vihola and Franks [115].

(2) The local linear regression can be applied to multi-parameter models to improve accuracy while reducing the dependence on the choice of ε.

(3) The performance of the ABC algorithm relies on a user's ability to summarize high-dimensional system responses into a few informative, low-dimensional summary statistics. To reduce this subjective component in the ABC algorithm, one can explore automatic ways of choosing informative statistics. For example, the recent study by Åkesson et al. [131] proposes a convolutional neural network architecture for automatically learning informative summary statistics of temporal responses.

(4) The ABC approach is highly parallelizable and does not require communication between processes. The main computational effort is thus spent on evaluating the model with sampled parameters. Consequently, if the model can fit into the memory of a general purpose graphical processing unit (GPGPU), the baseline ABC and ABC-MCMC algorithms can be substantially accelerated.

Bibliography

[1] W. D. Bachalo and D. A. Johnson. Transonic, turbulent boundary-layer separation generated on an axisymmetric flow model. AIAA journal, 24(3):437–443, 1986.

[2] J. Bardina, J. Ferziger, and W. C. Reynolds. Improved subgrid scale models for Large Eddy Simulation. AIAA paper, No. 80-1357, 1980.

[3] J. Bardina, J. H. Ferziger, and W. C. Reynolds. Improved turbulence models based on Large Eddy Simulation of homogeneous, incompressible turbulent flows. Technical Report TF-19, Thermosciences Division Department of Mechanical Engineering Stanford University, 1983.

[4] Mark A Beaumont. Approximate Bayesian Computation in evolution and ecology. Annual review of ecology, evolution, and systematics, 41:379–406, 2010.

[5] Mark A. Beaumont. Approximate Bayesian Computation. Annual review of statistics and its application, 6:379–403, 2019.

[6] Mark A. Beaumont, Wenyang Zhang, and David J. Balding. Approximate Bayesian Computation in population genetics. Genetics, 162(4):2025–2035, 2002.

[7] Mark A. Beaumont, Jean-Marie Cornuet, Jean-Michel Marin, and Christian P. Robert. Adaptive Approximate Bayesian Computation. Biometrika, 96(4):983–990, 2009.

[8] Michael G. B. Blum and Olivier François. Non-linear regression models for Approximate Bayesian Computation. Statistics and Computing, 20(1):63–73, 2010.

[9] M. A. Bolshov, Y. A. Kuritsyn, and Y. V. Romanovskii. Tunable diode laser spectroscopy as a technique for combustion diagnostics. Spectrochimica Acta Part B: Atomic Spectroscopy, 106:45–66, 2015.

[10] J. M. Bonnie and G. Sanford. Computer program for calculation of complex chemical equilibrium compositions and applications. User's Manual and Program Discription, 1996.

[11] François Bouttier and Graeme Kelly. Observing-system experiments in the ecmwf 4d-var data assimilation system. Quarterly Journal of the Royal Meteorological Society, 127(574): 1469–1488, 2001.

[12] S. Boyd and L. Chua. Fading memory and the problem of approximating nonlinear operators with Volterra series. IEEE Trans. Circuit Syst., 32:1150, 1985.

[13] T. Cai, T. Tan, G. Wang, W. Chen, and X. Gao. Gas temperature measurements using wavelength modulation spectroscopy at 1.39 μm. Optica Applicata, 39(1), 2009.

[14] Ewan Cameron and A. N. Pettitt. Approximate Bayesian Computation for astronomical model analysis: a case study in galaxy demographics and morphological transformation at high redshift. Monthly Notices of the Royal Astronomical Society, 425(1):44–65, 2012.

[15] T. Chai and R. R. Draxler. Root mean square error (rmse) or mean absolute error (mae)?–arguments against avoiding rmse in the literature. Geoscientific Model Development, 7(3): 1247–1250, 2014.

[16] Jun Chen, Charles Meneveau, and Joseph Katz. Scale interactions of turbulence subjected to a straining-relaxation-destraining cycle. Journal of Fluid Mechanics, 562:123–150, 2006.

[17] Sai Hung Cheung, Todd A. Oliver, Ernesto E. Prudencio, Serge Prudhomme, and Robert D. Moser. Bayesian uncertainty analysis with applications to turbulence modeling. Reliability Engineering & System Safety, 96(9):1137–1149, 2011.

[18] Marissa L. Childs, Thomas H. Pulliam, and Dennis C. Jespersen. Overflow turbulence model resource verification results. Technical Report NAS-2014-03, NASA Ames Research Center, 2014.

[19] K.-S. Choi and J. L. Lumley. Return to isotropy of homogeneous turbulence revisited. In Turbulence and Chaotic Phenomena in Fluids, pages 267–272, 1984.

[20] J. D. Christopher, N. T. Wimer, C. Lapointe, T. R. S. Hayden, I. Grooms, G. B. Rieker, and P. E. Hamlington. Parameter estimation for complex thermal-fluid flows using approximate bayesian computation. Physical Review Fluids, 3:104602, 2018.

[21] Jason D. Christopher, Caelan Lapointe, Nicholas T. Wimer, Torrey R. S. Hayden, Ian Grooms, Gregory B. Rieker, and Peter E. Hamlington. Parameter estimation for a turbulent buoyant jet with rotating cylinder using Approximate Bayesian Computation. In 23rd AIAA Computational Fluid Dynamics Conference, page 3629, 2017.

[22] Jason D. Christopher, Caelan Lapointe, Nicholas T. Wimer, Torrey R. S. Hayden, Ian Grooms, Gregory B. Rieker, and Peter E. Hamlington. Parameter estimation for a turbulent buoyant jet using Approximate Bayesian Computation. In 55th AIAA Aerospace Sciences Meeting, page 0531, 2017.

[23] Jason D. Christopher, Cealan Lapointe Nicholas T. Wimer, Torrey R. S. Hayden, Ian Grooms, Gregory B. Rieker, and Peter E. Hamlington. Parameter estimation for complex thermal-fluid flows using Approximate Bayesian Computation. Physical Review Fluids, 3:104602, 2018.

[24] P. G. Constantine, Q. Wang, A. Doostan, and G. Iaccarino. A surrogate accelerated Bayesian inverse analysis of the HyShot II flight data. AIAA Paper, AIAA-2011-2037, 2011.

[25] S. A. Cottilard. Catalytic combustion. Nova Science Publ., 2011.

[26] Katalin Csilléry, Michael G. B. Blum, Oscar E. Gaggiotti, and Olivier François. Approximate Bayesian Computation (ABC) in practice. Trends in ecology & evolution, 25(7):410–418, 2010.

[27] J. W. Daily. Laser induced fluorescence spectroscopy in flames. Progress in Energy and Combustion Science, 23(2):133–199, 1997.

[28] Olga A. Doronina, Jason D. Christopher, Colin A. Z. Towery, Peter E. Hamlington, and Werner J. A. Dahm. Autonomic closure for turbulent flows using Approximate Bayesian Computation. In 2018 AIAA Aerospace Sciences Meeting, page 0594, 2018.

[29] Olga A. Doronina, Colin A. Z. Towery, Jason D. Christopher, Ian Grooms, and Peter E. Hamlington. Turbulence model development using Markov chain Monte Carlo Approximate Bayesian Computation. In AIAA Scitech 2019 Forum, page 1883, 2019.

[30] V. Ebert, T. Fernholz, C. Giesemann, H. Pitz, H. Teichert, J. Wolfrum, and H. Jaritz. Simultaneous diode-laser-based in situ detection of multiple species and temperature in a gas-fired power plant. Proceedings of the Combustion Institute, 28(1):423–430, 2000.

[31] D. C. Estumano, F. C. Hamilton, M. J. Colaço, A. J. K. Leiroz, H. R. B. Orlande, R. N. Carvalho, and G. S. Dulikravich. Bayesian estimate of mass fraction of burned fuel in internal combustion engines using pressure measurements. Engineering Optimization IV, pages 997–1003, 2015.

[32] Nelson J. R. Fagundes, Nicolas Ray, Mark Beaumont, Samuel Neuenschwander, Francisco M. Salzano, Sandro L. Bonatto, and Laurent Excoffier. Statistical evaluation of alternative models of human evolution. Proceedings of the National Academy of Sciences, 104(45): 17614–17619, 2007.

[33] J.H. Frank and S.A. Kaiser. High-resolution imaging of dissipative structures in a turbulent jet flame with laser rayleigh scattering. Experiments in Fluids, 44:221–233, 2008.

[34] T. B. Gatski and T. Jongen. Nonlinear eddy viscosity and algebraic stress models for solving complex turbulent flows. Progress in Aerospace Science, 36:655–682, 2000.

[35] M. Germano, U. Piomelli, P. Moin, and W. H. Cabot. A dynamic subgrid-scale eddy viscosity model. Phys. Fluids A, 3:1760–1765, 1991.

[36] Massimo Germano, Ugo Piomelli, Parviz Moin, and William H. Cabot. A dynamic subgrid-scale eddy viscosity model. Physics of Fluids A: Fluid Dynamics, 3(7):1760–1765, 1991.

[37] Sharath S. Girimaji. Fully explicit and self-consistent algebraic Reynolds stress model. Theoretical and Computational Fluid Dynamics, 8(6):387–402, 1996.

[38] C. S. Goldenstein and R. K. Hanson. Diode-laser measurements of linestrength and temperature-dependent lineshape parameters for h2o transitions near 1.4 μm using voigt, rautian, galatry, and speed-dependent voigt profiles. Journal of Quantitative Spectroscopy and Radiative Transfer, 152:127–139, 2015.

[39] C. S. Goldenstein, C. L. Strand, I. A. Schultz, K. Sun, J. B. Jeffries, and R. K. Hanson. Fitting of calibration-free scanned-wavelength-modulation spectroscopy spectra for determination of gas properties and absorption lineshapes. Applied Optics, 53(3):356–367, 2014.

[40] Christopher S. Goldenstein and Garrett C. Mathews. Simulation technique enabling calibration-free frequency-modulation spectroscopy measurements of gas conditions and lineshapes with modulation frequencies spanning khz to ghz. Applied Optics, 59(5):1491–1500, 2020.

[41] Christopher S. Goldenstein, R. Mitchell Spearrin, Jay B. Jeffries, and Ronald K. Hanson. Infrared laser-absorption sensing for combustion gases. Progress in Energy and Combustion Science, 60:132–176, 2017.

[42] C. Greenshields. OpenFOAM | The OpenFOAM Foundation, March 2016. URL http://openfoam.org/.

[43] Heikki Haario, Eero Saksman, and Johanna Tamminen. An adaptive Metropolis algorithm. Bernoulli, 7(2):223–242, 2001.

[44] P. E. Hamlington and W. J. A. Dahm. Nonlocal form of the rapid pressure-strain correlation in turbulent flows. Physical Review E, 80:046311, 2009.

[45] P. E. Hamlington and M. Ihme. Modeling of Non-Equilibrium Homogeneous Turbulence in Rapidly Compressed Flows. Flow, Turbulence and Combustion, 93(1):93–124, 2014.

[46] Peter E. Hamlington and Werner J. A. Dahm. Reynolds stress closure for nonequilibrium effects in turbulent flows. Physics of Fluids, 20(11):115101, November 2008.

[47] Peter E. Hamlington and Werner J. A. Dahm. Frequency response of periodically sheared homogeneous turbulence. Physics of Fluids, 21(5):055107, May 2009.

[48] R. K. Hanson and P. K. Falcone. Temperature measurement technique for high-temperature gases using a tunable diode laser. Applied Optics, 17(16):2477–2480, 1978.

[49] T. R. S. Hayden and G. B. Rieker. Large amplitude wavelength modulation spectroscopy for sensitive measurements of broad absorbers. Optics Express, 24(24):27910–27921, 2016.

[50] T. R. S. Hayden, N. Malarich, D. J. Petrykowski, S. P. Nigam, J. D. Christopher, C. Lapointe, N. T. Wimer, P.E. Hamlington, and G. B. Rieker. Oh radical measurements in combustion environments using wavelength modulation spectroscopy and dual-frequency comb spectroscopy near 1491 nm. Applied Physics B, 125, 2019.

[51] Torrey R. S. Hayden, Nicholas T. Wimer, Caelan Lapointe, Jason D. Christopher, Siddharth P. Nigam, Aniruddha Upadhye, Mark Strobel, Peter E. Hamlington, and Gregory B. Rieker. Characterization of the buoyant jet above a catalytic combustor using wavelength modulation spectroscopy. Combustion Science and Technology, 192(6):997–1014, 2020.

[52] T.R.S. Hayden, D.J. Petrykowski, A. Sanchez, S.P. Nigam, C. Lapointe, J.D. Christopher, N.T. Wimer, A. Upadhye, M. Strobel, P.E. Hamlington, and G.B. Rieker. Characterization of oh, h_2o, and temperature profiles in industrial flame treatment systems interacting with polymer films. Proceedings of the Combustion Institute, 37(2):1571–1578, 2019.

[53] Q. Huang, F. Wang, H. Zhang, J. Yan, M. Ni, and K. Cen. In-situ co measurement of gas and oil combustion flame using near infrared tunable diode laser with direct and modulated absorption signals. Optics Communications, 306:99–105, 2013.

[54] W. Jahn, G. Rein, and J. L. Torero. Forecasting fire dynamics using inverse computational fluid dynamics and tangent linearisation. Advances in Engineering Software, 47(1):114–126, 2012.

[55] Dennis C. Jespersen, Thomas H. Pulliam, and Marissa L. Childs. Overflow turbulence modeling resource validation results. Technical Report NAS-2016-01, NASA Ames Research Center, 2016.

[56] J.-C. Jouhaud, P. Sagaut, B. Enaux, and J. Laurenceau. Sensitivity analysis and multiobjective optimization for LES numerical parameters. Journal of Fluids Engineering, 130(2): 021401, 2008.

[57] R. N. King, P. E. Hamlington, and W. J. A. Dahm. Autonomic closure for turbulence simulations. Physical Review E, 93: 031301(R), 2016.

[58] B. E. Launder, G. J. Reece, and W. Rodi. Progress in the development of a Reynolds-stress turbulence closure. Journal of Fluid Mechanics, 68(3):537–566, 1975.

[59] Moon Lee and W. S. Reynolds. Numerical experiments on the structure of homogeneous turbulence. Technical Report TF-19, Thermosciences Division Department of Mechanical Engineering Stanford University, 1985.

[60] Sophia Lefantzi, Jaideep Ray, Srinivasan Arunajatesan, and Lawrence Dechant. Estimation of $k-\varepsilon$ parameters using surrogate models and jet-in-crossflow data. Technical report, Technical report, Sandia National Laboratories, Livermore, CA, USA, 2015.

[61] Yi Li, Eric Perlman, Minping Wan, Yunke Yang, Charles Meneveau, Randal Burns, Shiyi Chen, Alexander Szalay, and Gregory Eyink. A public turbulence database cluster and applications to study Lagrangian evolution of velocity increments in turbulence. Journal of Turbulence, 9:N31, 2008.

[62] D. K. Lilly. A proposed modification of the Germano subgrid-scale closure method. Phys. Fluids A, 4(3):633, 1992.

[63] Jarno Lintusaari, Michael U. Gutmann, Ritabrata Dutta, Samuel Kaski, and Jukka Corander. Fundamentals and recent developments in Approximate Bayesian Computation. Systematic biology, 66(1):e66–e82, 2017.

[64] Fabio Luciani, Scott A Sisson, Honglin Jiang, Andrew R Francis, and Mark M Tanaka. The epidemiological fitness cost of drug resistance in Mycobacterium tuberculosis. Proceedings of the National Academy of Sciences, 106(34):14711–14715, 2009.

[65] Lin Ma, Yue Wu, Wenjiang Xu, Stephen D. Hammack, Tonghun Lee, and Campbell D. Carter. Comparison of 2d and 3d flame topography measured by planar laser-induced fluorescence and tomographic chemiluminescence. Applied Optics, 55(20):5310–5315, 2016.

[66] H. Madsen. Parameter estimation in distributed hydrological catchment modelling using automatic calibration with multiple objectives. Advances in Water Resources, 26(2):205–216, 2003.

[67] J. M. Marin, P. Pudlo, C. P. Robert, and R. J. Ryder. Approximate Bayesian computational methods. Statistics and Computing, 22(6):1167–1180, 2012.

[68] Jean-Michel Marin, Pierre Pudlo, Christian P. Robert, and Robin J. Ryder. Approximate Bayesian Computational methods. Statistics and Computing, pages 1–14, 2012.

[69] P. Marjoram, J. Molitor, V. Plagnol, and S. Tavaré. Markov chain Monte Carlo without likelihoods. Proceedings of the National Academy of Sciences, 100(26):15324–15328, 2003.

[70] Paul Marjoram and Simon Tavaré. Modern computational approaches for analysing molecular genetic variation data. Nature Reviews Genetics, 7(10):759, 2006.

[71] Paul Marjoram, John Molitor, Vincent Plagnol, and Simon Tavaré. Markov chain Monte Carlo without likelihoods. Proceedings of the National Academy of Sciences, 100(26):15324–15328, 2003.

[72] C. S. Mcenally, L. D. Pfefferle, A. M. Schaffer, M. B. Long, R. K. Mohammed, M. D. Smooke, and M. B. Colkei. Characterization of a coflowing methane/air non-premixed flame with computer modeling, rayleigh-raman imaging, and on-line mass spectrometry. Proceedings of the Combustion Institute, 28(2):2063–2070, 2000.

[73] T.A. McManus and J.A. Sutton. Simultaneous 2d filtered rayleigh scattering thermometry and stereoscopic particle image velocimetry measurements in turbulent non-premixed flames. Experiments in Fluids, 61:134, 2020.

[74] C. Meneveau and J. Katz. Scale-invariance and turbulence models for Large-Eddy Simulation. Annual Review of Fluid Mechanics, 32:1–32, 2000.

[75] Florian R Menter. Two-equation eddy-viscosity turbulence models for engineering applications. AIAA journal, 32(8):1598–1605, 1994.

[76] Johan Meyers, Pierre Sagaut, and Bernard J Geurts. Optimal model parameters for multi-objective Large-Eddy Simulations. Physics of Fluids, 18(9):095103, 2006.

[77] Mikael Mortensen and Hans Petter Langtangen. High performance python for direct numerical simulations of turbulent flows. Computer Physics Communications, 203:53–65, 2016.

[78] S. Mosbach, A. Braumann, P. L. W. Man, C. A. Kastner, G. P. E. Brownbridge, and M. Kraft. Iterative improvement of Bayesian parameter estimates for an engine model by means of experimental design. Combustion and Flame, 159(3):1303–1313, 2012.

[79] W. L. Oberkampf and C. J. Roy. Verification and validation in scientific computing. Cambridge University Press, 2010.

[80] W. L. Oberkampf and T. Trucano. Validation methodology in computational fluid dynamics. In Fluids 2000 Conference and Exhibit, page 2549, 2000.

[81] W. L. Oberkampf and T. G. Trucano. Verification and validation in computational fluid dynamics. Progress in Aerospace Sciences, 38(3):209–272, 2002.

[82] W. L. Oberkampf, T. G. Trucano, and C. Hirsch. Verification, validation, and predictive capability in computational engineering and physics. Applied Mechanics Reviews, 57(5): 345–384, 2004.

[83] Todd A. Oliver and Robert D. Moser. Bayesian uncertainty quantification applied to RANS turbulence models. In Journal of Physics: Conference Series, volume 318, page 042032. IOP Publishing, 2011.

[84] Eric J. Parish and Karthik Duraisamy. A paradigm for data-driven predictive modeling using field inversion and machine learning. Journal of Computational Physics, 305:758–774, 2016.

[85] E. Pemha and E. Ngo Nyobe. Genetic algorithm approach and experimental confirmation of a laser-based diagnostic technique for the local thermal turbulence in a hot wind tunnel jet. Progress In Electromagnetics Research, 28:325–350, 2011.

[86] Louis C. Philippe and Ronald K. Hanson. Laser diode wavelength-modulation spectroscopy for simultaneous measurement of temperature, pressure, and velocity in shock-heated oxygen flows. Applied Optics, 32(30):6090–6103, 1993.

[87] Umberto Picchini. Inference for SDE models via Approximate Bayesian Computation. Journal of Computational and Graphical Statistics, 23(4):1080–1100, 2014.

[88] S. B. Pope. A more general effective-viscosity hypothesis. Journal of Fluid Mechanics, 72 (02):331–340, 1975.

[89] Z. Qu, R. Ghorbani, D. Valiev, and F. M. Schmidt. Calibration-free scanned wavelength modulation spectroscopy–application to h 2 o and temperature sensing in flames. Optics Express, 23(12):16492–16499, 2015.

[90] Jaideep Ray, Sophia Lefantzi, Srinivasan Arunajatesan, and Lawrence Dechant. Bayesian calibration of a $k - \epsilon$ turbulence model for predictive jet-in-crossflow simulations. In 44th AIAA Fluid Dynamics Conference, page 2085, 2014.

[91] Jaideep Ray, Sophia Lefantzi, Srinivasan Arunajatesan, and Lawrence Dechant. Bayesian Parameter Estimation of a $k - \varepsilon$ Model for Accurate Jet-in-Crossflow Simulations. AIAA Journal, pages 2432–2448, 2016.

[92] Jaideep Ray, Lawrence Dechant, Sophia Lefantzi, Julia Ling, and Srinivasan Arunajatesan. Robust bayesian calibration of a $k - \varepsilon$ model for compressible jet-in-crossflow simulations. AIAA Journal, 56(12):4893–4909, 2018.

[93] Jaideep Ray, Sophia Lefantzi, Srinivasan Arunajatesan, and Lawrence Dechant. Learning an Eddy Viscosity Model Using Shrinkage and Bayesian Calibration: A Jet-in-Crossflow Case Study. ASCE-ASME J Risk and Uncertainty in Engineering Systems. Part B: Mechanical Engineering, 4(1):011001, March 2018. doi: 10.1115/1.4037557.

[94] G. B. Rieker, J. B. Jeffries, and R. K. Hanson. Calibration-free wavelength-modulation spectroscopy for measurements of gas temperature and concentration in harsh environments. Applied Optics, 48(29):5546–5560, 2009.

[95] J. Rohmer, M. Rousseau, A. Lemoine, R. Pedreros, J. Lambert, and A. Benki. Source characterisation by mixing long-running tsunami wave numerical simulations and historical observations within a metamodel-aided ABC setting. Stochastic Environmental Research and Risk Assessment, pages 1–18.

[96] L. S. Rothman, I. E. Gordon, Y. Babikov, A. Barbe, D. C. Benner, P. F. Bernath, M. Birk, L. Bizzocchi, V. Boudon, and L. R. Brown. The hitran2012 molecular spectroscopic database. Journal of Quantitative Spectroscopy and Radiative Transfer, 130:4–50, 2013.

[97] Donald B. Rubin. Bayesianly justifiable and relevant frequency calculations for the applied statistician. The Annals of Statistics, 12(4):1151–1172, 1984.

[98] Cosmin Safta, Myra Blaylock, Jeremy Templeton, Stefan Domino, Khachik Sargsyan, and Habib Najm. Uncertainty quantification in LES of channel flow. International Journal for Numerical Methods in Fluids, 83(4):376–401, 2017.

[99] A. G. Salinger, R. P. Pawlowski, J. N. Shadid, and B. G. van Bloemen Waanders. Computational analysis and optimization of a chemical vapor deposition reactor with large-scale computing. Industrial & Engineering Chemistry Research, 43(16):4612–4623, 2004.

[100] F. Sarghini, G. De Felice, and S. Santini. Neural networks based subgrid scale modeling in Large Eddy Simulations. Computers & fluids, 32(1):97–108, 2003.

[101] John Schaefer, Serhat Hosder, Thomas West, Christopher Rumsey, Jan-Renee Carlson, and William Kleb. Uncertainty Quantification of Turbulence Model Closure Coefficients for Transonic Wall-Bounded Flows. AIAA Journal, 55(1):195–213, January 2017. ISSN 0001-1452, 1533-385X.

[102] Christof Schulz and Volker Sick. Tracer-lif diagnostics: quantitative measurement of fuel concentration, temperature and fuel/air ratio in practical combustion systems. Progress in Energy and Combustion Science, 31(1):75–121, 2005.

[103] D. W. Scott. On optimal and data-based histograms. Biometrika, 66(3):605–610, 1979.

[104] David W Scott. Multivariate density estimation: theory, practice, and visualization. John Wiley & Sons, 2015.

[105] B. W. Silverman. Density estimator for statistics and data analysis. Statistics and Applied Probability, 1986.

[106] Scott A. Sisson, Yanan Fan, and Mark Beaumont. Handbook of Approximate Bayesian Computation. Chapman and Hall/CRC, 2018.

[107] J. Smagorinsky. General circulation experiments with the primitive equations I. The basic experiment. Monthly Weather Review, 91(3):99–164, 1963.

[108] Jorge Sousa, Clara García-Sánchez, and Catherine Gorlé. Improving urban flow predictions through data assimilation. Building and Environment, 132:282–290, 2018.

[109] R. M. Spearrin, C. S. Goldenstein, J. B. Jeffries, and R. K. Hanson. Quantum cascade laser absorption sensor for carbon monoxide in high-pressure gases using wavelength modulation spectroscopy. Applied Optics, 53(9):1938–1946, 2014.

[110] C. G. Speziale and R. M. C. So. The Handbook of Fluid Dynamics, chapter 14.Turbulence Modeling and Simulation, pages 14.1–14.111. Springer, 1998.

[111] C. G. Speziale, S. Sarkar, and T. B. Gatski. Modeling the pressure strain correlation of turbulence: an invariant dynamical systems approach. Journal of Fluid Mechanics, 227: 245–272, 1991.

[112] K. Sun, X. Chao, R. Sur, C. S. Goldenstein, J. B. Jeffries, and R. K. Hanson. Analysis of calibration-free wavelength-scanned wavelength modulation spectroscopy for practical gas sensing using tunable diode lasers. Measurement Science and Technology, 24(12):125203, 2013.

[113] M. Sunnåker, A. G. Busetto, E. Numminen, J. Corander, M. Foll, and C. Dessimoz. Approximate Bayesian Computation. PLoS Computational Biology, 9(1):e1002803, 2013.

[114] Mikael Sunnåker, Alberto Giovanni Busetto, Elina Numminen, Jukka Corander, Matthieu Foll, and Christophe Dessimoz. Approximate Bayesian Computation. PLoS Computational Biology, 9(1):e1002803, January 2013.

[115] Matti Vihola and Jordan Franks. On the use of approximate Bayesian computation Markov chain Monte Carlo with inflated tolerance and post-correction. Biometrika, page asz078, February 2020.

[116] I. Vrbik, R. Deardon, Z. Feng, A. Gardner, and J. Braun. Using individual-level models for infectious disease spread to model spatio-temporal combustion dynamics. Bayesian Analysis, 7(3):615–638, 2012.

[117] S. Wagner, B. T. Fisher, J. W. Fleming, and V. Ebert. Tdlas-based in situ measurement of absolute acetylene concentrations in laminar 2d diffusion flames. Proceedings of the Combustion Institute, 32(1):839–846, 2009.

[118] S. Wallin and A. V. Johansson. An explicit algebraic Reynolds stress model for incompressible and compressible turbulent flows. Journal of Fluid Mechanics, 403:89–132, 2000.

[119] S. Wang and X. Xu. Parameter estimation of internal thermal mass of building dynamic models using genetic algorithm. Energy Conversion and Management, 47(13-14):1927–1941, 2006.

[120] Y. Wang, P. Chatterjee, and J. L. de Ris. Large eddy simulation of fire plumes. Proceedings of the Combustion Institute, 33(2):2473–2480, 2011.

[121] Anna Wawrzynczak and Piotr Kopka. Approximate Bayesian Computation for estimating parameters of data-consistent Forbush decrease model. Entropy, 20(8):622, 2018.

[122] Daniel Wegmann, Christoph Leuenberger, and Laurent Excoffier. Efficient Approximate Bayesian Computation coupled with Markov chain Monte Carlo without likelihood. Genetics, 182(4):1207–1218, 2009.

[123] H. G. Weller, G. Tabor, H. Jasak, and C. Fureby. A tensorial approach to computational continuum mechanics using object-oriented techniques. Computers in Physics, 12(6):620–631, 1998.

[124] David C Wilcox. Reassessment of the scale-determining equation for advanced turbulence models. AIAA journal, 26(11):1299–1310, 1988.

[125] Heng Xiao and Paola Cinnella. Quantification of model uncertainty in RANS simulations: A review. Progress in Aerospace Sciences, 108:1–31, July 2019.

[126] Munehiko Yamaguchi, Takeshi Iriguchi, Tetsuo Nakazawa, and Chun-Chieh Wu. An observing system experiment for typhoon conson (2004) using a singular vector method and dotstar data. Monthly Weather Review, 137(9):2801–2816, 2009.

[127] Dazhi Yu and Sharath S. Girimaji. Direct numerical simulations of homogeneous turbulence subject to periodic shear. Journal of Fluid Mechanics, 566:117, November 2006.

[128] Jincheng Zhang and Song Fu. An efficient approach for quantifying parameter uncertainty in the SST turbulence model. Computers & Fluids, 181:173–187, 2019.

[129] Yatian Zhao, Chao Yan, Xiaoyong Wang, Hongkang Liu, and Wei Zhang. Uncertainty and sensitivity analysis of SST turbulence model on hypersonic flow heat transfer. International Journal of Heat and Mass Transfer, 136:808–820, June 2019. ISSN 00179310.

[130] Ye Zheng and Stephane Aris-Brosou. Approximate Bayesian Computation algorithms for estimating network model parameters. bioRxiv, page 106450, 2017.

[131] Mattias Åkesson, Prashant Singh, Fredrik Wrede, and Andreas Hellander. Convolutional Neural Networks as Summary Statistics for Approximate Bayesian Computation. arXiv:2001.11760 [cs, stat], January 2020.

Appendix A

Catalytic Burner

A.1 Physical experiments setup

The catalytic burner examined here has been studied previously [51, 50] and is a scaled-down version of catalytic burners commonly used for industrial heating of food products and polymer films. The catalytic burner is 0.25 m long by 0.075 m wide and combusts a mixture of methane and desiccated air. An iron-chromium alloy catalyst mesh is welded to an open-box metal frame. The catalyst is used to achieve more complete combustion at lower temperatures, thereby reducing the presence of reactive products of incomplete combustion and pollutants [25] in the burner exit gases. To premix the oxidizer and fuel, the reactants pass through a bed of glass spheres within a cylindrical flame arrestor mounted beneath the combustor. A schematic of the present burner experiment is shown in Fig. A.1(a), and a photograph of the burner in operation, with accompanying laser optics, is shown in Fig. A.1(b).

Experimental measurements were made using wavelength modulation spectroscopy (WMS), which provides line-of-sight, absorption-weighted average temperature and chemical species concentrations. As shown in Fig. A.1, the WMS measurements were made along the longest dimension of the burner (termed the 'length' herein and denoted by the z-axis) at the midpoint of the burner width (i.e., the center of the x-dimension of the burner). Vertical profiles (i.e., as a function of height above the burner along the y-axis) of line-of-sight, absorption-weighted average temperature were measured for three different burner operating powers; these profiles provide reference data for the ABC parameter estimation described in Section 3.4.

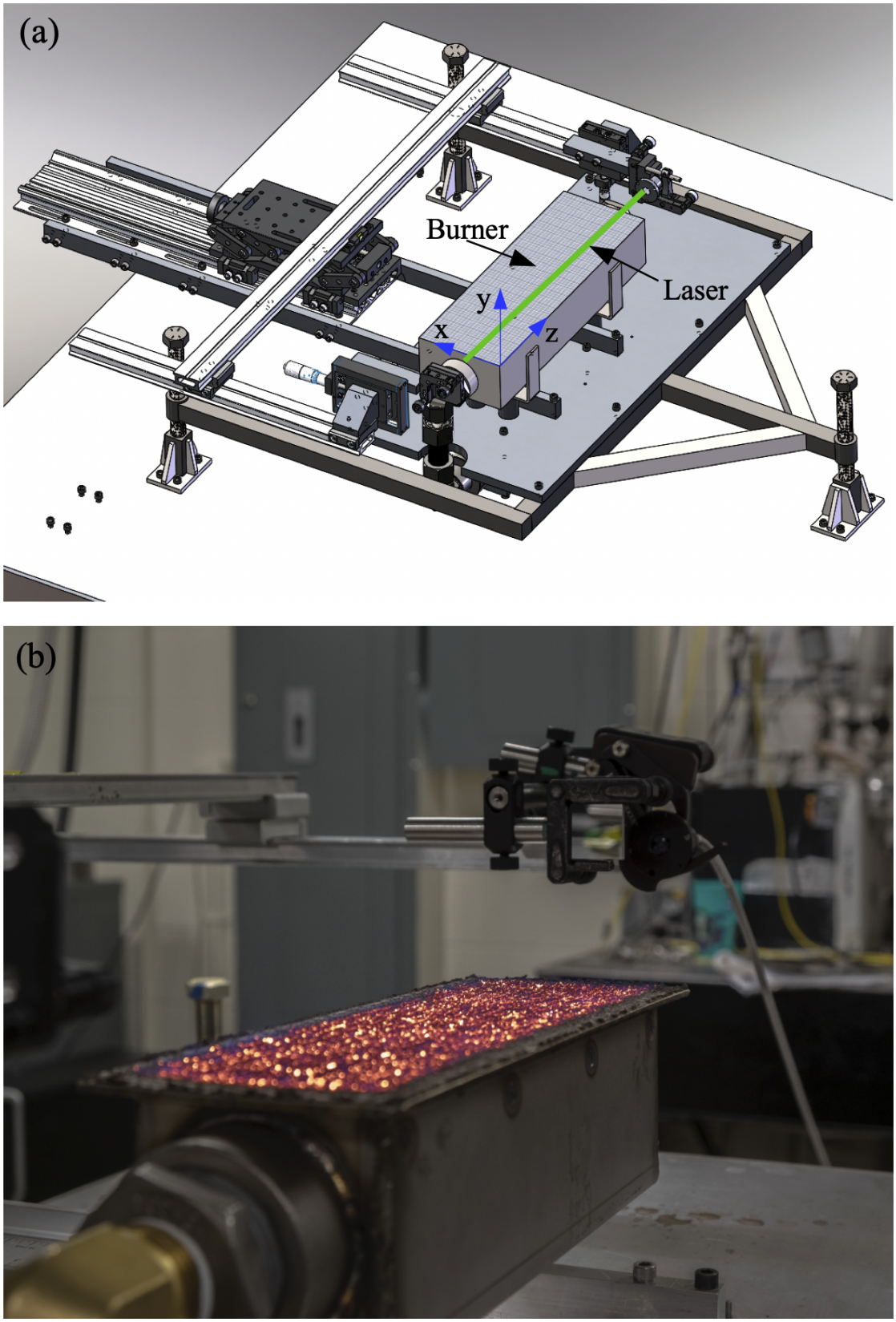

Figure A.1: Schematic of the experimental setup for laser absorption spectroscopy above the catalytic burner (a), and an image of the burner in operation, including laser optics (b).

A.1.1 Laser absorption spectroscopy (LAS)

Tunable diode laser absorption spectroscopy (TDLAS) was used to perform **in situ** temperature measurements in the flow above the catalytic burner. This method provides a non-intrusive, quantitative, absolute, time-resolved, robust, and portable sensor [41] to measure temperature at different locations in the flow. Other laser-based techniques such as Raman or Rayleigh scattering and laser induced fluorescence can also provide quantitative spatial and temporal information [27, 72, 102, 33, 65, 73]. However, such measurements often require large optical setups that are not ideal for industrial applications. The use of TDLAS herein is thus motivated by the practical feasibility of this approach for characterization and control of real-world industrial systems.

From a quantitative perspective, Beer's law can be used to model the transmitted intensity of the laser through the absorbing gases and is given as

$$I_{\mathrm{t}}(t) = I_0(t)\exp[-\alpha(\lambda)]\,, \tag{A-1}$$

where $I_{\mathrm{t}}(t)$ is the intensity of the transmitted modulated light after it passes through the absorbing gases, $I_0(t)$ is the incident (i.e., un-attenuated) intensity, $\lambda(t)$ is the wavelength of the laser as a function of time, and $\alpha(\lambda)$ is the absorbance of the probed molecular species as a function of wavelength. As discussed below, the absorbance depends on the gas temperature, species concentration, pressure, and pathlength, and thus by measuring the incident and transmitted laser intensities, the gas properties can be determined.

In this study, we use WMS, a specialized form of TDLAS, to obtain **in situ** temperature measurements. This method has been used previously to measure temperature and species mole fractions in a variety of combustion environments, from shock tubes to atmospheric flames [86, 30, 13, 117, 53, 109, 89, 9, 49, 40]. Compared to traditional TDLAS, where the wavelength of a diode laser is tuned across one or two quantum transitions of the target species, WMS uses additional high frequency signals and signal isolation to reduce noise for real-world systems.

To conduct WMS, a fast modulation is applied to the injection current of a tunable diode laser, which results in rapid wavelength and intensity variations of the laser light. A lock-in amplifier

isolates the series of harmonics in the signal measured at the detector, which occur due to the fast intensity modulation and the effects of absorption. The second harmonic is especially useful because it is distinctly sensitive to absorption. In particular, normalizing the second harmonic signal (denoted $2f$) by the first harmonic (denoted $1f$) creates a ratio (i.e., $2f/1f$) that is sensitive to absorption, but insensitive to intensity fluctuations. This ratio makes the sensor robust in harsh environments and enables calibration-free absolute measurements [94].

Although the specific shape of an absorption transition is also dependent on the other non-absorbing gases present in the system (e.g., CO_2, CO, etc., in combustion systems), the integrated absorbance is independent of the collision partner, and is therefore a more useful quantity to measure. The integrated absorbance is extracted from the measured $2f/1f$ ratio using an approach similar to that described in Refs. [49, 112, 39]. Using the measured WMS $2f/1f$ signal as a baseline, the simulated $2f/1f$ signal is adjusted until the two signals are in close agreement. In particular, the Voigt line-shape profile parameters (i.e., line-center, integrated area, Doppler width, and Lorentz width) are adjusted in a nonlinear fitting code until the profiles match. The spectral database HITRAN 2012 and the validated line parameters from Goldenstein **et al.** [38] are used to create initial estimates for the Voigt parameters.

Temperature is calculated using the integrated absorbances that emerge from the fitted Voigt profiles for two different measured H_2O transitions. This technique, called two-line thermometry [48], calculates temperature using the ratio of integrated absorbances from WMS fits to the two H_2O transitions. Integrated absorbance, A, is computed over the laser pathlength as

$$A_i(p,T) = p\int_0^L S_i(T,x)\chi_{\text{abs}}(x)dx\,, \tag{A-2}$$

where p is the total pressure (assumed constant for the entire pathlength), $S_i(T,x)$ is the line strength of the ith probed transition at temperature T and location x, $\chi_{\text{abs}}(x)$ is the species mole fraction of the absorbing gas, and L is the total pathlength of the laser beam.

The ratio of the integrated absorbances A_1 and A_2 of two H_2O absorption features yields a

quantity, R, that depends only on the temperature, namely

$$R = A_1/A_2 = f(T)\,. \tag{A-3}$$

The ratio of the two H_2O absorption transitions is directly related to temperature, despite the fact that each individual integrated absorbance is independently related to species mole fraction. Based on a ratio of the signal absorbed at the two different wavelengths (and hence for two different quantum transitions), a temperature can be calculated [51]. The resulting temperature is, effectively, an absorption-weighted average temperature over the laser pathlength (or 'line of sight').

A.1.2 Experimental setup

The present WMS measurements use two NEL Inc. distributed feedback diode lasers centered on H_2O absorption transitions at 1391.7 nm and 1468.9 nm. These absorption transitions have two primary advantages that make them ideal for temperature measurements in this system. First, they have a large difference in the lower state energy (1045 cm^{-1} and 3319 cm^{-1}, respectively); this optimizes the temperature sensitivity at elevated temperatures. Second, Goldenstein and Hanson [38] have previously validated these line strength parameters, thus providing ideal conditions for fitting the Voigt profiles.

The lasers are combined and simultaneously passed across the long dimension of the burner (i.e., the lasers initially travel above the burner for 0.25 m parallel to the z-axis). To increase the signal-to-noise ratio, the combined laser is reflected twice, causing the laser to pass over the burner three times, creating an effective path length of 0.75 m. The sensor was previously validated in a controlled system for known conditions [51]; temperature measurements were found to be accurate within 3% up to approximately 1300 K. Above this temperature, uncertainties were extrapolated using the nonlinear relationship between absorption and temperature from Eq. (A-3). A fume hood was located several feet above the burner to evacuate exhaust gases, producing a negligible impact on the high-temperature flow close to the burner surface. Calibration data, along with additional setup information and data processing techniques, can be found in Hayden **et al.** [51].

To obtain vertical profiles of temperature, a 'y'-shaped optical stage was mounted on a scissor jack, enabling vertical translation of the laser beam along the y-axis (see Fig. A.1). Measurements were taken at heights of 0.5 mm to 10.5 mm above the burner in 2 mm increments, then 10.5 mm to 150.5 mm above the burner in 10 mm increments. All measurements were performed along the length (i.e., z-axis) of the burner centered across the burner width (i.e., 37.5 mm from the edge in the x direction; see Fig. A.1). This resulted in temperature measurements at 20 vertical positions. The tighter measurement spacing close to the burner provides additional information in the region most likely to contain sustained combustion after the gases pass through the catalytic mesh. Data are averaged for 10 mins at each height to remove any slow transients in burner conditions or room air fluctuations.

A.2 Numerical experiments setup

A.2.1 Large eddy simulations (LES)

To accurately represent the flow physics above the catalytic burner while maintaining sufficient computational affordability so that up to $\mathcal{O}(10^3)$ distinct choices of $\mathbf{c}$ could be sampled, 3D LES was used for the computational model. The fireFOAM solver [120] in OpenFOAM version 4 [42, 123] was used to perform the LES.

The computational configuration consisted of a non-reacting heated, buoyant jet with a rectangular exit matching the size of the catalytic burner described in Section A.1. The low-pass filtered compressible Navier-Stokes equations were solved with second-order accuracy in space and time, in conjunction with mass, enthalpy, and species conservation equations. The LES equations were closed using a dynamic one-equation eddy SGS model. Coupling between the pressure and velocity was accomplished using the PIMPLE algorithm, which combines the Pressure-Implicit with Spliting of Operators (PISO) and Semi-Implicit Method for Pressure Linked Equations (SIMPLE) algorithms. Heat transfer mechanisms represented in the LES include conduction, transport of temperature by advection of chemical species, and radiative losses (approximated using the discrete

ordinate method).

The LES equations were solved on a 3D grid with approximately 2.4×10^6 hexahedral control volumes stretched vertically to enhance the resolution near the burner, resulting in a finest vertical resolution of approximately 0.8 mm. The grid was uniform in horizontal directions. The computational domain is shown in Fig. A.2(a). The domain dimensions (0.35 m long by 0.175 m wide by 1.2 m tall) were chosen to allow the bottom-driven jet to exit the domain primarily vertically at the top boundary. The burner inflow was centered at the bottom of the domain and was 0.25 m long and 0.075 m wide, corresponding to the dimensions of the catalytic burner shown in Fig. A.1.

Time stepping was adaptive and controlled by a maximum Courant-Friedrichs-Lewy (CFL) of 0.4. After a sufficiently long period to allow the flow field to fully develop, mean statistics for temperature were computed over a duration of 1 s. Samples obtained using this time period were found to be within approximately 1% of samples obtained over a 20 s averaging period, while allowing many more simulations to be performed for different parameters $\mathbf{c}$. Example temperature and speed fields from one such simulation are shown in Figs. A.2(b) and (c), respectively.

To account for the possibility of continued combustion within the domain, heat release was modeled above the combustor by adding a source term to the enthalpy equation in fireFOAM. Heat was added using a half-Gaussian distribution with the peak occurring at the burner surface, then trailing off in intensity as height increases above the burner (i.e., in the y-direction), as shown in Fig. A.2(a). Heat was applied uniformly in the 0.075 m by 0.25 m region directly above the burner; at x and z-locations beyond the edge of the burner, the heat addition was set to zero.

Inlet conditions were fixed at close to the temperatures measured at the combustor surface (i.e., close to T_0 in Table 3.1). The exact values of T_0 from Table 3.1 were not used in the simulations because the experimental measurements provide absorption weighted temperatures, rather than the unweighted temperatures required in the simulations, and because the lowest experimental measurement was still 0.5 mm above the burner surface. We thus increased the temperature boundary condition slightly compared to T_0 in each simulation; we found that surface temperatures of 1515 K, 1610 K, and 1685 K were sufficient to provide reasonable agreement between the experimental and

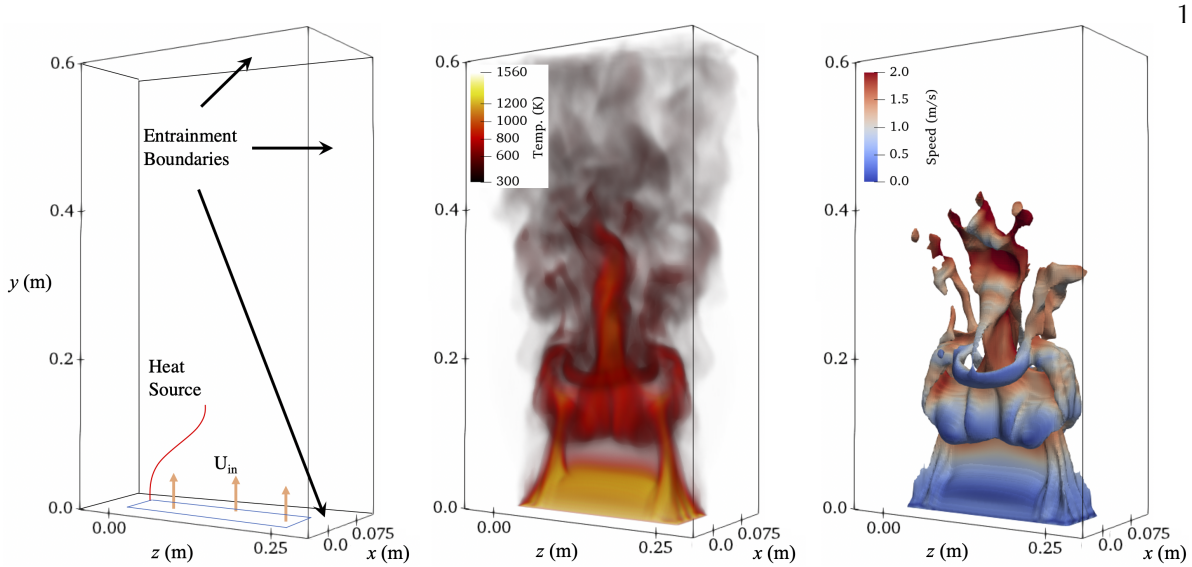

Figure A.2: Schematic showing the setup of the 3D LES domain (left), temperature field (i.e., volume rendering of a 500 K isosurface and additional volume rendering at higher locations) of a single snapshot in time from a simulation with inlet mean temperature of 1515 K and inlet speed of 0.38 m/s with no additional heat added above the burner surface (middle), and speed field on the same temperature isosurface (right).

simulation results at the first measurement height of 0.5 mm. The composition of the exit gases was determined by specifying equilibrium products of complete combustion. Mass fractions of N_2, O_2, H_2O and CO_2 were fixed accordingly, as specified by the NASA software Chemical Equilibrium Analysis (CEA) [10]. The equivalence ratio, ϕ, was set in the simulations to match the values in Table 3.1 for each of the three experimental cases.

It should be noted that, although the presence of continued combustion in the burner exit gases is not consistent with equilibrium conditions at the burner surface, the true composition of the exit gases is unknown. However, the assumption of chemical equilibrium is acceptable in the present study because combustion is not directly modeled in the LES, and the exact composition of the species at the inlet thus has limited impact on the conclusions of the analysis. Additionally, the calculation of absorption-weighted equivalent summary statistics using the LES data, as described in the next section, does not depend on the absolute quantity of H_2O present in the domain, but instead depends on the distribution of H_2O, which is assumed to enter the domain uniformly in space and time.

A.2.2 LAS-equivalent model summary statistics

To effectively compare the experimental and LES results, as is required for ABC, we constructed summary statistics from the LES that were equivalent to the line-of-sight absorption-weighted average LAS measurements. Although a spatial average over the LES computational cells through which the laser passes would be the simplest option for computing these statistics, this approach neglects the nonlinear relationship between temperature and absorption, as well as the effect of spatial variations in the H_2O mole fraction.

Consequently, we calculated the integrated absorbance that would occur for each of the two lasers passing through the LES domain. To accomplish this conversion, linestrengths (i.e., the amount of laser absorption) were determined for the range of temperatures observed in the LES using the reference temperature linestrengths in Ref. [38], with the partition function from [96]. Based on 3D fields of temperature and H_2O mole fraction from the LES, line strengths were integrated for each laser using spatially resolved temperatures along the laser paths, with each line strength weighted by the normalized H_2O mole fraction. We then used the ratio of integrated line strengths for each laser to determine a line-of-sight absorption-weighted average temperature, as given by Eq. (A-3), at a given height.

Temperatures were recorded from the LES at the center of the burner in the x-direction, 3.75 cm from the burner edge, parallel to the z-axis at each of the LAS measurement heights. At each output time, the temperature and H_2O mole fraction at each height were used to calculate a line of sight absorption weighted average temperature. These time series were averaged to obtain LAS-equivalent temperatures; the resulting vertical profiles of average temperature comprise the modeled summary statistics $\hat{\mathcal{S}}$ that are compared with the LAS summary statistics shown in Fig. 3.1.

The LES data were also adjusted to account for uncertainties inherent in the measurements. For each sampled parameter $\mathbf{c}$, a uniform random number between $\pm 3\%$ was selected independently 1,000 times, and this amount of uncertainty was added to the entire profile of temperature (assuming that any bias observed in the experiment was correlated at all heights). The resulting modeled

summary statistics $\mathcal{S}'$, each with added uncertainty, were then compared with the reference values $\mathcal{S}$ for each of the 1,000 randomly selected uncertainties, for each value of $\mathbf{c}$. It should be noted, however, that the variation in $\mathcal{S}'$ was generally larger due to variations in $\mathbf{c}$, as opposed to variations in the applied uncertainty.